UNIMOLECULAR PHOTODISSOCIATION STUDIES IN MOLECULAR BEAMS AND FLOW TUBES

by

Wyatt G. Merrill

A dissertation submitted in partial fulfillment of

the requirements for the degree of

Doctor of Philosophy

(Chemistry)

at the

University of Wisconsin–Madison

2017

Date of final oral examination: 08/28/2017

The dissertation is approved by the following members of the Final Oral Committee:

F. Fleming Crim, Emeritus Professor, Chemistry

Gilbert Nathanson, Professor, Chemistry

Etienne Garand, Assistant Professor, Chemistry

John Wright, Professor, Chemistry

Amanda Case, Assistant Professor, Chemistry, Augsburg College

Unimolecular photodissociation studies in molecular beams and flow tubes

Wyatt G. Merrill

Under the supervision of Professor F. Fleming Crim

at the University of Wisconsin–Madison

The present work details gas-phase photodissociation studies of unimolecular reactions in two distinct apparatus: (1) a high-vacuum molecular beam chamber capable of velocity map imaging and (2) a newly constructed high-pressure flow tube. In both cases, we initiate photodissociation and probe the ensuing products with pulsed ns-lasers.

Experiments carried out in the molecular beam apparatus investigate energy disposal and relative quantum yields following Ã-band photodissociation of $CHBrCl_2$ at 215, 225, 235, 245, 255, and 265 nm. The Ã-band of $CHBrCl_2$ consists of $\sigma^* \leftarrow n$ transitions to a number of repulsive electronic states, and subsequent C−Br bond cleavage occurs rapidly. Excess energy partitions between internal degrees of freedom in the $CHCl_2$ photofragment, spin-orbit excitation in the Br fragment, and kinetic energy. We probe the Br photofragments in a state-selective manner using resonance enhanced multiphoton ionization (REMPI) and time of flight (TOF) mass spectrometry, thereby discerning the ground-state Br and spin-orbit excited Br* product channels. We measure the relative yields of Br and Br* at each photolysis wavelength by integrating their respective TOF signals. The velocity map imaging (VMI) technique resolves the kinetic energy of the recoiling photofragments, yielding a measurement of the $CHCl_2$ fragment internal energy from energy conservation. We employ classical impulsive modeling to predict the partitioning of $CHCl_2$ internal energy between

vibrational and rotational degrees of freedom.

The $^3Q_{0^+}(\mathrm{A}')$ and $^1Q_1(\mathrm{A}')$ diabats in $CHBrCl_2$ mix to form an avoided crossing that plays an important role in the photodissociation dynamics and product yields. This crossing region, taken with the numerous accessible electronic states in the $\tilde{\mathrm{A}}$-band, necessitates a relatively complex description of the photodissociation process. To this end, we rely on the anisotropy present in the VMI data as well as studies on similar halomethanes to complement the energy disposal and yield measurements. We find that the partial absorption cross section of $^3Q_{0^+}(\mathrm{A}')$ is present throughout the $\tilde{\mathrm{A}}$-band, although competition from other electronic states is evident. At longer photolysis wavelengths, propensity for adiabatic passage through the avoided crossing region dictates the relative quantum yield for Br and Br*. At shorter wavelengths, electronic states not subject to the crossing region influence the relative yields as well. Because the center of mass for the $CHCl_2$ fragment does not lie along the C−Br bond axis, dissociation generates a high degree of rotational excitation in the $CHCl_2$ fragment, and this is reflected in our VMI data. However, we find that classical impulsive models overestimate this rotational excitation, suggesting that the angular dependence of the potential and the evolution of the $CHCl_2$ geometry, which promotes vibrational excitation, are important aspects of the dissociation dynamics.

We subsequently designed a high-pressure flow tube apparatus to carry out kinetics measurements using the same laser system as the molecular beam apparatus. The flow tube contains an upstream region where pulsed-laser photolysis initiates unimolecular photodissociation and a downstream region where laser-induced fluorescence (LIF) detects the rise of products generated by unimolecular decomposition. We characterize the fluid transport and detection properties of the apparatus. In particular, we measure flow rates and radial velocity

profiles to assess flow development and transport times between the photolysis and detection regions. We characterize LIF capabilities in our apparatus by detecting OH following nitric acid photodissociation in the flow. The flow tube is designed to investigate unimolecular decomposition relevant to atmospheric chemistry, and we show that the timescales it is equipped to measure are amenable to studies of peroxy radical intermediates generated during the oxidation of volatile organic compounds in the troposphere. The decomposition of these peroxy radicals yields OH products, and we demonstrate our ability to measure these products over a range of pressures and flow rates.

Table of Contents

List of Figures

List of Tables

Acknowledgments

I have heard enough stories on the school yard to know how fortunate I am to have an advisor like Fleming. It is regrettable that promising graduate students of all walks will commonly cite their advisor as a reason for abandoning research, and so let this be a record to the contrary—Fleming renewed my passion for research at a watershed moment in my graduate career. He demonstrates incisiveness, curiosity, and humility in the most inspiring manner imaginable. My gratitude for his patience and teaching as I matured as an experimentalist cannot be overstated. As his final graduate student, I wish to make it known that I have been imbued with exclusive and sacred torch-passing teachings, but it must be said that Fleming's wisdom has reached countably-infinite others as well.

As an undergraduate, I fell into a similarly fortuitous research setting with my physics professor, Sudha Swaminathan. Sudha cared about me as a burgeoning researcher more than I understood at the time, but I know now what a tremendous privilege it was to receive her guidance and wisdom. Her previous advisory role has become one of friendship, and I am so glad we maintain correspondence and find time to see one another when we are able.

Cornelia Heid was my first mentor in the dark arts of the laser lab, and I am forever in her debt for the patience and expertise that required. The various post cards I hung above my desk from her post-grad globetrotting (literally trotting much of the time, no doubt) were daily reminders that we need not abandon our sense of adventure for an expertise in quantum chemistry developed in labs with no windows. I am so grateful for Cornelia's teachings and friendship.

The design and fabrication of the flow tube apparatus would not have left the proverbial

runway were it not for the tenacity and foresight of Amanda Case. Her thoughtful research and conception of the flow tube during the time I was finishing my molecular beam experiments was of far greater consequence to my graduate career than I realized at the time. If I refer to myself in the first person singular at any point during the discussion of the flow tube experiments, the reader should take this to mean "Amanda and I" and mentally amend the appropriate verb conjugation. Moreover, Amanda has been a friend and a mentor for the bulk of my time in Madison, and I know I am not alone in appreciating her role in that capacity.

In a similar sense, I am indebted to Steve Myers and the entire UW-Madison machine shop. Steve is not only a world-class machinist, he is also as curious and drawn to problem-solving as any scientist I have met, and discussions with him about the flow tube fabrication and the endless modifications thereafter were invaluable. I have little doubt that if he decided to pursue the same degree that I have he would finish in half the time.

I also acknowledge the remaining members of my thesis committee—Gil Nathanson, Etienne Garand, and John Wright. I taught for Gil for two semesters as a TA and was as inspired as any of his undergraduate onlookers by the exuberant love of chemistry he wore on his sleeve. Taking his class on surface chemistry was a no-brainer (in the sense that it was an easy decision, not in the sense that it took no brains), and I consider him a chief inspiration in the art of asking questions. Etienne and his research group treated me like one of their own while Fleming did his community service as an NSF director. Their comradery is much appreciated. John joined my thesis committee late in the game, but I knew he was a great choice ever since I won a gift card in the departmental poster session that he judged.

There is a long list of friends I wish to acknowledge that I considered including in an

appendix, but the guidelines issued by the UW Graduate School suggest that would not be apropos. Tyler and Camden share the dubious achievement of most likely to keep in touch with the friend who abandoned them to do science halfway across the country, and I hope they know how much that means to me. I was fortunate to live with two people in graduate school who were far more than merely roommates, Adrian and Stephanie. Life in Madison would have been very different (read as: much worse) without their companionship. Danny, Brett, Brandon, Travis, Jessi, Daniel, Katie, Tom, Andrew, Kevin, *et al.*, I cherish the memories of our time together in Madison. Let's make more elsewhere! I could write an entire acknowledgments section about each of you.

My family is a fount of love and support. It goes without saying that I could never have found my way here without their guidance. There are many un-talked-about character traits that grant success in science, and I reckon upbringing is responsible for most (the rest are stochastic). Words fail. Thank you, from the bottom of my heart, for all your help and caring. You never doubted me, and it means the world.

Finally, I must thank Next Door Brewing Company. My patronage there led to tenure in the form of a cramped studio above the establishment during my final months in Madison, and many long nights writing this dissertation were much improved by their craft beers and free wifi connection.

"It warn't so. I tried it."

—*Huckleberry Finn*

For my parents and their parents

Chapter 1

Introduction

1.1 Photodissociation theory and experiment

Photodissociation is a chemical reaction in which absorption of one or more photons leads to bond rupture in a molecule. Innumerable experimental and theoretical methods beyond the purview of this chapter have interrogated photodissociation with great success. Indeed, studies of light-matter interaction, bond breaking, and energy transfer are superlatively fundamental to physical chemistry. Moreover, fundamental studies give rise to a host of novel applied methods that use photodissociation as a tool to investigate atmospheric chemistry, combustion, surface chemistry, and many other related fields. Here, the scope of background information will be limited to gas-phase, experimental techniques utilizing pulsed-ns laser systems and the requisite introductory quantum theory underpinning these techniques. Much of this chapter uses Reinhard Schinke's *Photodissociation Dynamics: Spectroscopy and Fragmentation of Small Polyatomic Molecules* as a valuable reference.[1]

1.1.1 Time-dependent *ab initio* treatment of photodissociation

To introduce the mechanics governing photodissociation in polyatomic molecules, it is pedagogically convenient to consider the photodissociation of a generic triatomic molecule ABC. Figure 1.1 depicts the ensuing discussion schematically. We use Jacobi coordinates to describe nuclear motion in ABC, in which r is the internuclear separation between B and C and R is the distance from A to the BC center-of-mass (s). Prior to absorbing a pho-

Figure 1.1: Schematic of wavepacket evolution throughout the photodissociation of a generic triatomic molecule ABC mediated by a fully repulsive excited electronic state. Note that the upper horizontal axis depicting the decay of the autocorrelation function $S(t)$ does not correspond with a particular energy.

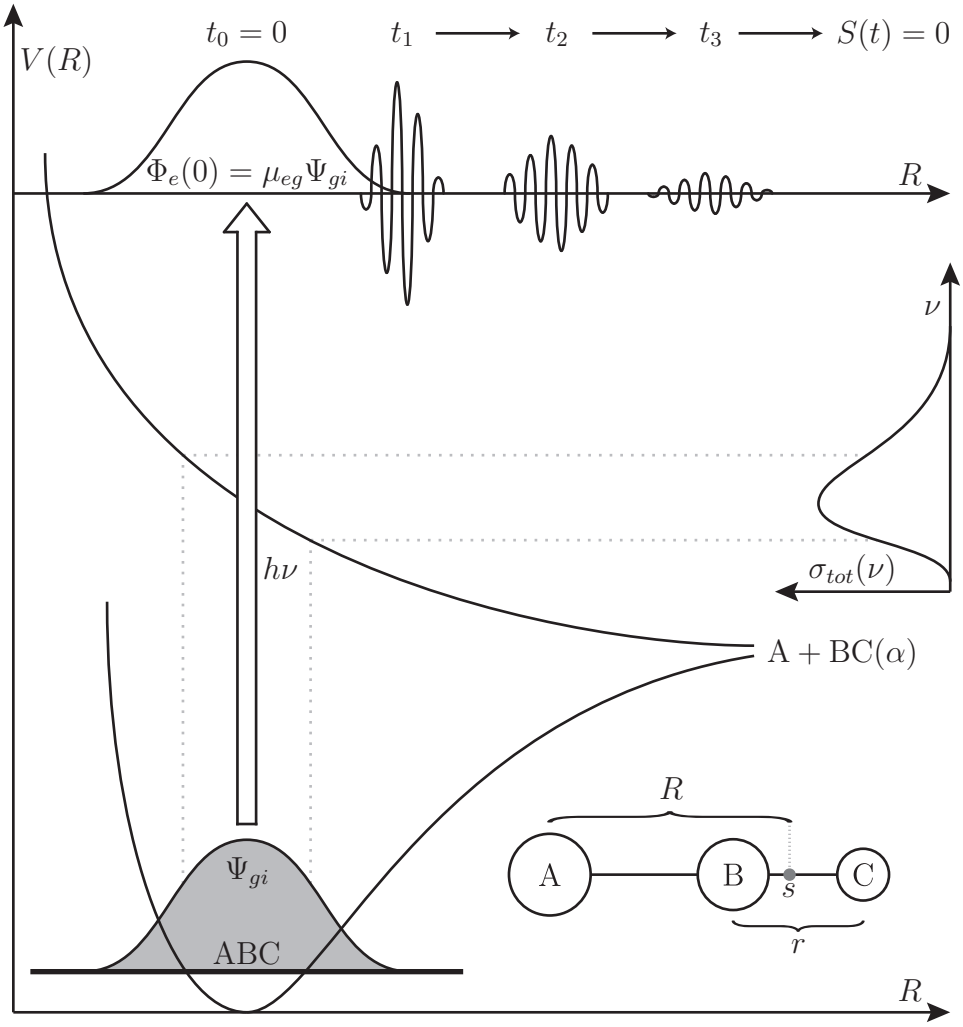
$V(R)$
$t_0 = 0$
t_1
t_2
t_3
$S(t) = 0$
$\Phi_e(0) = \mu_{eg}\Psi_{gi}$
R
ν
$h\nu$
$\sigma_{tot}(\nu)$
$\mathrm{A} + \mathrm{BC}(\alpha)$
R
Ψ_{gi}
A
B
C
s
r
ABC
R

ton of frequency ν, ABC is in the ground (g) electronic state $|\Psi_{gi}\rangle$ with a particular set of vibrational-rotational quantum numbers (i). Absorption promotes ABC to a purely repulsive excited (e) electronic state with slope $\partial V/\partial R$ where the nuclei move in time (t), eventually leading to photofragments A + BC in quantum state α. The time-dependent Schrödinger equation (TDSE)

$$i\hbar\frac{\partial}{\partial t}\Phi_e(t) = \hat{H}_e\Phi_e(t) \tag{1.1}$$

governs this evolution, where $\hat{H}_e$ is the Hamiltonian for the excited electronic state and $\Phi_e(t)$ is the time-dependent wavepacket evolving in that state. If we take $t = 0$ to be the absorption event and assume instantaneous promotion to the excited electronic state,

$$\Phi_e(0) = \mu_{eg}\Psi_{gi} \tag{1.2}$$

where μ_{eg} is the transition dipole moment. At a given time t during the dissociation, the solution to the TDSE

$$\Phi_e(t) = \mathrm{e}^{-i\hat{H}_e t/\hbar}\Phi_e(0) \tag{1.3}$$

is therefore just the time-evolution operator $\mathrm{e}^{-i\hat{H}_e t/\hbar}$ applied to the product of the stationary state for the ABC parent and the dipole transition moment.

Details of the dynamics outlined above are contained in the total photodissociation cross section $\sigma_{tot}(\nu)$ and the partial photodissociation cross sections $\sigma(\nu, \alpha)$ for ABC, which a pulsed-ns laser setup can measure experimentally. The total photodissociation cross section is concerned only with the probability of absorbing a photon of a particular frequency leading to bond rupture, whereas a partial photodissocation cross section represents the probability of absorbing a photon of frequency ν leading to fragments in quantum state α. Naturally,

the sum of the partial photodissociation cross sections

$$\sigma_{tot}(\nu) = \sum_{\alpha} \sigma(\nu, \alpha) \tag{1.4}$$

is the total photodissociation cross section.

The Fourier transform of an appropriate function will relate the frequency-resolved cross section measurements to the time-resolved wavepacket evolution of ABC. That function is the autocorrelation function $S(t)$, which is defined as the overlap integral

$$S(t) \equiv \langle \Phi_e(0) | \Phi_e(t) \rangle \tag{1.5}$$

of the evolving wavepacket and the initial wavepacket. Broadly speaking, autocorrelation reveals similarities between observables as a function of the time lag between them. As it pertains to wavepacket evolution in the ABC excited state, $S(t)$ reveals the residence time of the wavepacket in the Franck-Condon region, and thus, how rapidly dissociation occurs. In excited electronic states with barriers to dissociation, the wavepacket can return to the origin geometry, giving rise to oscillations in $S(t)$ that manifest as structural features in the absorption spectrum. The spectrum for ABC, on the other hand, will be unstructured due to the purely repulsive excited state surface. The breadth of the absorption for ABC will depend on the steepness of the excited state potential in two dimensions: $\partial V/\partial R$ and $\partial V/\partial r$. Steeper surfaces in the Franck-Condon region lead to broader absorption and faster dissociation. Section 1.1.2 will address the dimensionality of the electronic excited state for larger polyatomic molecules, but this principle is easily generalized.

As promised, the Fourier transform of $S(t)$

$$\sigma_{tot}(\nu) \propto \int_{-\infty}^{+\infty} S(t) \mathrm{e}^{iEt/\hbar} dt \tag{1.6}$$

returns the total photodissociation cross section, where E is the sum of the initial ground state energy of ABC and the absorbed photon energy $h\nu$. Projecting $\Phi_e(t \to \infty)$ onto the stationary eigenstates of the separated photofragments yields the partial photodissociation cross sections. Experimentally, state-resolved product detection following photodissociation with a narrow bandwidth laser can discern $\sigma(\nu, \alpha)$. Section 1.1.5 will discuss the methods of state-specific detection that we use to achieve this.

1.1.2 Degrees of freedom and potential energy surfaces

The evolution of the wavepacket in Figure 1.1 takes place along a single coordinate R, which simplifies not only the artistic wherewithal needed to depict the process but also the intramolecular and intermolecular forces acting on the separating photofragments. Such a simplification is only strictly true for diatomic molecules, where the electronic potential depends solely on the internuclear distance of the two atoms. For non-linear polyatomics, $V(R)$ in Figure 1.1 is a one-dimensional cut from a potential energy surface (PES) dictated fully by $3N - 6$ coordinates, where N is the number of nuclei in the parent molecule. This dimensionality is the number of vibrational degrees of freedom present in the molecule. In photodissociation, the energy remaining after bond rupture may be taken up by these degrees of freedom, or by other degrees of freedom such as translation, rotation, or electronic excitation. It is the topology of the full-dimensional PES that governs this energy partitioning.

In principle, one maps out a PES by varying the $3N - 6$ nuclear coordinates and solving the corresponding electronic Schrödinger equation within the Born-Oppenheimer approxi-

mation,[2] which separates the electronic and nuclear degrees of freedom on the basis of their (typically) distinct timescales. In practice, this can be challenging computationally. Each electronic state in a molecule corresponds with a single PES, and each PES requires ∼10 points per degree of freedom. This results in a computational bottleneck that scales exponentially with the number of nuclei. Furthermore, the PES of excited electronic states, which are accessed during UV photodissociation, are more difficult to calculate than their ground-state counterparts.[3] Couplings between degrees of freedom can also complicate the electronic Hamiltonian. For instance, electronic states of many-electron atoms are known to have strong coupling between the electron spin and the magnetic field generated by electron orbital motion (the so-called spin-orbit interaction).

1.1.3 Transitions between potential energy surfaces

The difficulty of computing a full-dimensional PES to study photodissociation is compounded by the many trajectories the separating photofragments can explore. Often, these trajectories include so-called nonadiabatic transitions from one PES to another. A transition of this sort is facilitated by coupling of electronic and nuclear motions, which constitutes a break-down of the Born-Oppenheimer approximation (a computational inconvenience if there ever was one).

Two basic approaches exist to treat these electronic transitions: adiabatic and diabatic representations. Again using the generic ABC photodissociation described in section 1.1.1, Figure 1.2 demonstrates the difference between the two representations schematically in a crossing region between excited-state potentials V_1 and V_2. For a given photofragment

Figure 1.2: Schematic of diabatic potential curves V_1 and V_2 crossing at internuclear distance R_C. Following absorption of a photon of frequency ν, ABC wavepacket evolution begins on the V_1 potential. The V_1 diabat leads to excited state produces $\mathrm{A}^* + \mathrm{BC}$, while the V_2 diabat leads to ground state products $\mathrm{A} + \mathrm{BC}$. Inset: adiabatic representation (dashed lines) of V_1 and V_2. $Q_{12}(R)$ represents the nonadiabatic coupling elements, which facilitate transfer between the adiabatic potentials during wavepacket evolution.

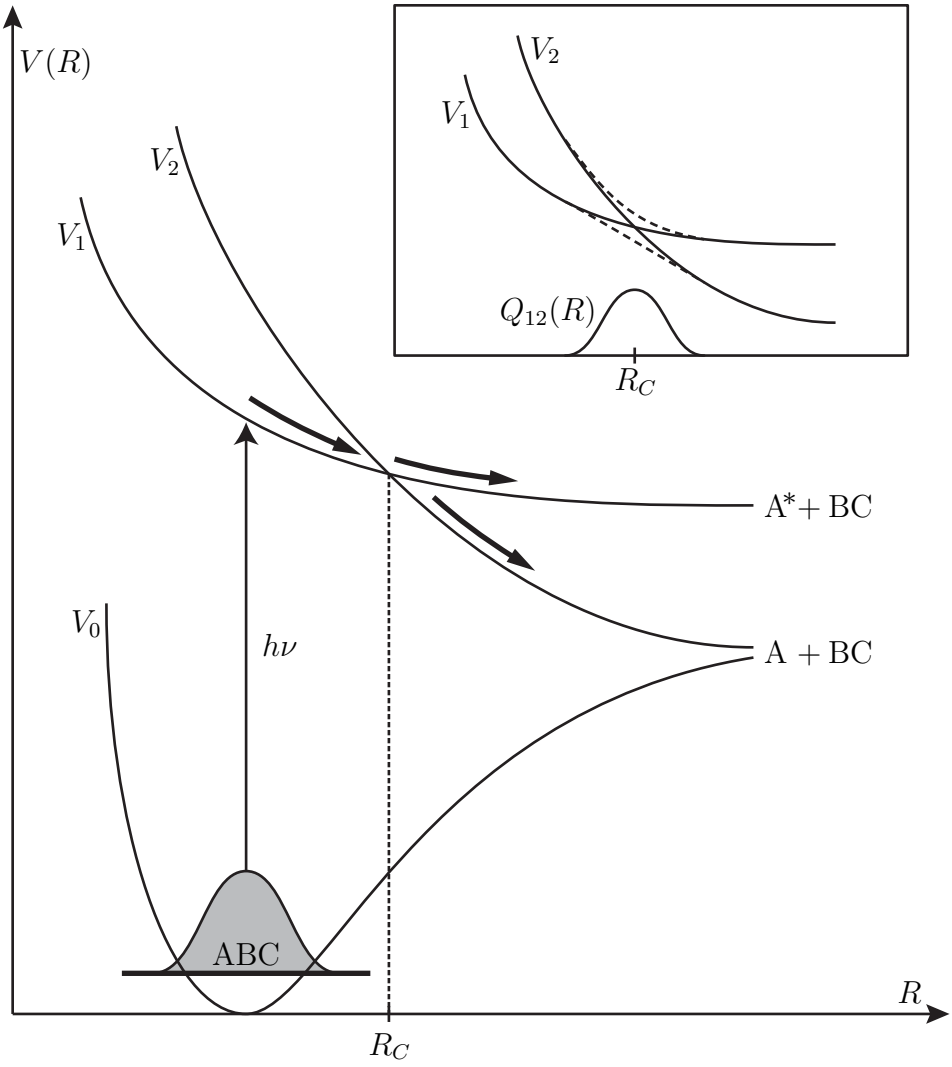
$V(R)$
V_2
V_1
V_0
$h\nu$
ABC
A*+ BC
A + BC
R_C
R
V_2
V_1
$Q_{12}(R)$
R_C

velocity, coupling between V_1 and V_2 in this region dictates the relative yield of excited- and ground-state products, and we will see that the origin of that coupling depends on which representation (adiabatic or diabatic) is used. Experimentally, one can resolve the branching between ground- and excited-state products in a straightforward way with proper detection methods (more on this in Section 1.1.5). Computationally, determining this branching is a formidable challenge. Let's see why.

1.1.3.1 Adiabatic representation

The total molecular Hamiltonian $\hat{H}_{mol}(\mathbf{q}; R, r)$ for ABC, which must include all nuclear and electronic degrees of freedom, is given by

$$\hat{H}_{mol}(\mathbf{q}; R, r) = \hat{H}_e(\mathbf{q}; R, r) + \hat{T}_n(R, r) \tag{1.7}$$

where $\mathbf{q}$ is a vector containing all the electronic coordinates that depends parametrically on R and r, $\hat{H}_e(\mathbf{q}; R, r)$ is the electronic Hamiltonian, and $\hat{T}_n(R, r)$ is the kinetic energy of the nuclei. Adiabatic representation expands the total wavefunction of the molecule $F(\mathbf{q}; R, r)$ in terms of the nuclear wavefunction $\Psi^n(R, r)$ and the electronic functions $\Theta^e(\mathbf{q}; R, r)$ that solve the Schrödinger equation for a particular set of nuclear coordinates r and R. That is,

$$F(\mathbf{q}; R, r) = \sum_k \Psi_k^n(R, r)\Theta_k^e(\mathbf{q}; R, r) \tag{1.8}$$

and

$$\hat{H}_e\Theta_k^e(\mathbf{q}; R, r) = V_k(R, r)\Theta_k^e(\mathbf{q}; R, r) \tag{1.9}$$

where $V_k(R, r)$ is the PES for the k^{th} electronic state such that $k = 0$ is the ground electronic state (the first root of Equation 1.9), $k = 1$ is the first excited electronic state (the second root

of Equation 1.9), and so on. Using $F(\mathbf{q}; R, r)$ for the wavefunction in the time-independent Schrödinger equation gives

$$\left[\hat{H}_{mol}(\mathbf{q}; R, r) - E\right] F(\mathbf{q}; R, r) = 0 \tag{1.10}$$

or by susbtitution,

$$\left[\hat{H}_e(\mathbf{q}; R, r) + \hat{T}_n(R, r) - E\right] \sum_{k'} \Psi^n_{k'}(R, r)\Theta^e_{k'}(\mathbf{q}; R, r) = 0 \tag{1.11}$$

where E is the total energy of ABC. Due to orthogonality, the overlap integral of two electronic wavefunctions is

$$\langle \Theta^e_k | \Theta^e_{k'} \rangle = \begin{cases} 1, & \text{if } k = k' \\ \\ 0, & \text{if } k \neq k'. \end{cases} \tag{1.12}$$

Therefore, we proceed by multiplying by $\langle \Theta^e_k|$ on the left and integrating each term over $\mathbf{q}$ so that two of the summations over k'

$$\begin{aligned} \langle \Theta^e_k | E \sum_{k'} \Psi^n_{k'}(R, r)\Theta^e_{k'} \rangle &= E \sum_{k'} \Psi^n_{k'}(R, r) \langle \Theta^e_k | \Theta^e_{k'} \rangle \\ &= E\Psi^n_k(R, r) \end{aligned} \tag{1.13}$$

and

$$\begin{aligned} \langle \Theta^e_k | \hat{H}_e | \sum_{k'} \Psi^n_{k'}(R, r)\Theta^e_{k'} \rangle &= \sum_{k'} \Psi^n_{k'}(R, r) \left\langle \Theta^e_k | \hat{H}_e | \Theta^e_{k'} \right\rangle \\ &= V_k(R, r)\Psi^n_k(R, r) \end{aligned} \tag{1.14}$$

are easily simplified. The third summation

$$\langle \Theta^e_k | \hat{T}_n | \sum_{k'} \Psi^n_{k'}(R, r)\Theta^e_{k'} \rangle = \sum_{k'} \langle \Theta^e_k | \hat{T}_n | \Psi^n_{k'}(R, r)\Theta^e_{k'} \rangle \tag{1.15}$$

is less cooperative. Equation 1.11 is now

$$\sum_{k'} \langle \Theta^e_k | \hat{T}_n | \Psi^n_{k'}(R, r)\Theta^e_{k'} \rangle + \left[V_k(R, r) - E\right] \Psi^n_k(R, r) = 0 \tag{1.16}$$

and it is clear that in the adiabatic representation, the electronic state k is coupled to the electronic state k' through the off-diagonal matrix elements of the nuclear kinetic energy operator. For ABC, the nuclear kinetic energy operator is given by

$$\hat{T}_n = -\frac{\hbar^2}{2m_A}\frac{\partial^2}{\partial R^2} - \frac{\hbar^2}{2\mu_{BC}}\frac{\partial^2}{\partial r^2} \tag{1.17}$$

where m_A is the mass of A and μ_{BC} is the reduced mass of BC. With this expression, one can rewrite Equation 1.16 as

$$\left[V_k(R,r) - E - \frac{\hbar^2}{2m_A}\frac{\partial^2}{\partial R^2} - \frac{\hbar^2}{2\mu_{BC}}\frac{\partial^2}{\partial r^2}\right]\Psi_k^n(R,r) + \sum_{k'}\left[Q_{kk'}^{(R)}\frac{\partial}{\partial R} + Q_{kk'}^{(r)}\frac{\partial}{\partial r} + U_{kk'}^{(R)} + U_{kk'}^{(r)}\right]\Psi_{k'}^n(R,r) = 0 \tag{1.18}$$

where

$$\begin{aligned} Q_{kk'}^{(R)} &= -\frac{\hbar^2}{m_A}\left\langle \Theta_k^e \middle| \frac{\partial}{\partial R} \middle| \Theta_{k'}^e \right\rangle \\ Q_{kk'}^{(r)} &= -\frac{\hbar^2}{\mu_{BC}}\left\langle \Theta_k^e \middle| \frac{\partial}{\partial r} \middle| \Theta_{k'}^e \right\rangle \\ U_{kk'}^{(R)} &= -\frac{\hbar^2}{2m_A}\left\langle \Theta_k^e \middle| \frac{\partial}{\partial R} \middle| \Theta_{k'}^e \right\rangle \\ U_{kk'}^{(r)} &= -\frac{\hbar^2}{2\mu_{BC}}\left\langle \Theta_k^e \middle| \frac{\partial}{\partial r} \middle| \Theta_{k'}^e \right\rangle \end{aligned} \tag{1.19}$$

are the nonadiabatic coupling elements (generalized as $Q_{12}(R)$ in Figure 1.2). The nonadiabatic coupling elements reflect the dependence of the electronic wavefunctions on the nuclear coordinates. Within the Born-Oppenheimer approximation, we assume these couplings are negligible and Equation 1.18 reduces to

$$\left[V_k(R,r) - E - \frac{\hbar^2}{2m_A}\frac{\partial^2}{\partial R^2} - \frac{\hbar^2}{2\mu_{BC}}\frac{\partial^2}{\partial r^2}\right]\Psi_k^n(R,r) = 0. \tag{1.20}$$

However, the nonadiabatic coupling elements become non-negligible in an avoided crossing region like the one shown in Figure 1.2, and their treatment may have considerable bearing

on product yields and energy partitioning. This is problematic, as they require first- and second-order derivatives of the electronic wavefunctions with respect to r and R (or, more generally, *all* nuclear degrees of freedom), and the electronic wavefunctions themselves are typically many-body functions dependent on a number of electronic coordinates. Indeed, a calculation of the nonadiabatic coupling elements is far more demanding computationally than that of a single PES.

1.1.3.2 Diabatic representation and the imperative of experiment

In diabatic representation, one constructs the electronic wavefunctions in such a way that the nonadiabatic coupling elements (Equation 1.19) are minimized.[4] This yields potentials for which the electronic basis changes smoothly throughout the crossing region, which is convenient for numerical applications but ensures that Θ_k^e is no longer an eigenstate of $\hat{H}_e$. Thus, the off-diagonal elements of $\hat{H}_e$ present a difficulty similar to those of $\hat{T}_n$ in adiabatic representation. That is, coupling between adiabatic states is facilitated by off-diagonal elements of $\hat{T}_n$ (kinetic coupling), while coupling between diabatic states is facilitated by off-diagonal elements of $\hat{H}_e$ (potential coupling).

Although the computational difficulties associated with constructing accurate full-dimensional potential energy surfaces and treating dissociation on and between these surfaces can in principle be met with sufficient computing power, in many cases such an approach is unfeasible. Moreover, in cases where improved computing capabilites do permit new computational studies, or novel approximations and insights are to be tested, it is experimental data that validate the success of these approaches. Experiment and theory are complimentary means of evaluating and revising our understanding of physical chemistry, and photodissoci-

ation studies provide a prototypical example of that. Nonetheless, the scale and complexity of the systems that can be investigated with quantum-mechanical accuracy is far greater for experimentalists. The remainder of the chapter will cover some relevant experimental methods for studying photodissociation and consider how photodissociation can be a component of broader experimental studies.

1.1.4 Pulsed laser systems

Few inventions have advanced experimental physical chemistry as significantly as the laser, particularly insofar as spectroscopy and photochemistry are concerned. Lasers offer unprecedented resolution in the time and spectral domains, as well as tremendous sensitivity down to single-molecule regimes. Pulsed lasers provide short, intense pulses of light with an extremely well defined wavelength, which is ideal for initiating particular quantum transitions with precise timing. We rely on pulsed-ns lasers to initiate photodissociation and to probe the resulting products in all of our experiments. In particular, we employ Nd:YAG lasers to pump tunable dye lasers. We use a number of optics in conjunction with these lasers to achieve harmonic generation, polarization, focusing, etc.

1.1.5 State-resolved product detection

Following photodissociation, quantum-state specific probing of the photofragments affords the measurement of $\sigma(\nu, \alpha)$, the partitioning of excess energy, and the branching between ground- and excited-state products. Techniques that achieve state-specific detection must be extremely sensitive and specific to a particular chemical species. This is especially true

in experiments with low pressures or high concentrations of background species. The two most common methods for achieving this are resonance-enhanced multiphoton ionization (REMPI)[5] and laser-induced fluorescence (LIF).[6] Both techniques rely on well-characterized spectroscopy of the excited electronic states of whatever species is being probed. Figure 1.3 depicts REMPI and LIF probing schematically.

1.1.5.1 Resonance-enhanced multiphoton ionization

Ionization meets the requirement for sensitive detection in a fairly routine manner. Electric fields generated by ion optics can guide ionized species towards a particle multiplier, a method widely used in mass spectrometric techniques. The energy required for ionization of most species necessitates multiphoton absorption in the visible and UV regions. When an intermediate excited electronic state is accessed during multiphoton absorption, ionization efficiency is dramatically enhanced. This is the essential feature of REMPI detection. With a narrow bandwidth laser, only species in a particular quantum state will access the intermediate state, ultimately leading to ionization and state-specific detection. An $(m+n)$ designation for REMPI schemes is typical, where m is the number of photons required to reach the resonant intermediate state and n is the number of photons required to exceed the ionization threshold from that state.

1.1.5.2 Laser-induced fluorescence

As the name suggests, LIF uses fluorescent emission from an excited electronic state as a signature of a particular chemical species. The electronic excitation to reach this state is generated by a laser and is quantum-state specific, so collecting the resulting fluorescence

Figure 1.3: Schematic of REMPI (left) and LIF (right) detection schemes. The REMPI detection pictured is a $2 + 1$ detection process, in which two photons are absorbed to reach a resonant excited electronic state and a third photon is absorbed in that state to achieve ionization. The LIF scheme involves absorption of a photon leading to an excited electronic state and subsequent emission of a photon of the same energy.

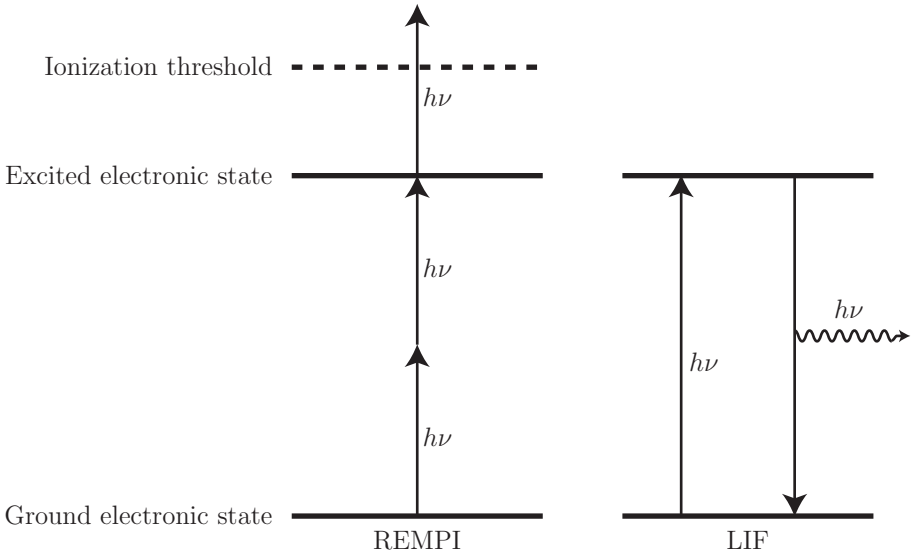
Ionization threshold
hν
Excited electronic state
hν
hν
Ground electronic state
REMPI
hν
hν
LIF

(typically with a photomultiplier tube) achieves state-specific detection. Since the excited molecule will fluoresce in all directions spatially, the detector can be positioned perpendicular to the laser path to minimize scattered light. The LIF signal will also occur on a longer timescale than the scattered light, so the signal can be gated with proper electronics to improve sensitivity.

1.2 Photodissociation as a tool for studying chemical kinetics

Unimolecular decomposition may proceed rapidly (as with photodissociation on a fully repulsive PES), or it may be slowed by isomerization processes and stabilized intermediates. A laser pulse can provide a well-defined starting time for these kinetics, and monitoring the decay of reactants or rise of products with a second laser pulse yields information about the rate of decomposition. Typically, the rate of photodissociation is faster than 1 ns, and therefore not amenable measurement with a pulsed-ns laser setup. However, the photodissociation event can initiate secondary reactions of interest, which may be much slower. The precise timing and specificity of bond cleavage makes photodissociation an ideal tool for studying such reactions.

The change of concentration of a reactant A in time due to unimolecular decomposition

$$\frac{d[\mathrm{A}]}{dt} = -k[\mathrm{A}] \tag{1.21}$$

is proportional to the rate constant k. Integration from $t = 0$ with an initial concentration

$[\mathrm{A}]_0$ of A gives

$$\ln\left(\frac{[\mathrm{A}]}{[\mathrm{A}]_0}\right) = -kt \tag{1.22}$$

or

$$[\mathrm{A}] = [\mathrm{A}]_0 e^{-kt} \tag{1.23}$$

where [A] is the concentration of A at time t. Measurement of [A] and [A]$'$ at times t and t' removes the need for knowledge of the initial concentration, since their ratio

$$\begin{aligned} \frac{[\mathrm{A}]}{[\mathrm{A}]'} &= \frac{[\mathrm{A}]_0 e^{-kt}}{[\mathrm{A}]_0 e^{-kt'}} \\ &= e^{k(t'-t)} \end{aligned} \tag{1.24}$$

gives k directly. Experimentally, this requires developing an environment in which the probe laser can reliably differentiate concentrations of a decaying reactant or a growing product at (at least) two points in time. The unimolecular decomposition cannot be complete, nor can it be too slow to discern the concentration of [A] at distinct times following photodissociation. The number of photons absorbed by the parent molecule must also be consistent between experiments measuring [A] and [A]$'$. We address these requirements by constructing and characterizing a flow tube apparatus, which will be described in detail in Chapter 4.

1.3 Structural layout

The remainder of this thesis will cover specific apparatus and experiments that rely on or are motivated by the background covered in this chapter. Chapters 2 and 3 detail studies of $CHBrCl_2$ photodissociation in a molecular beam. Chapter 4 covers the design, construction, and characterization of a flow tube apparatus that utilizes photodissociation to initiate uni-

molecular reactions and LIF to probe the resulting products. Chapter 5 concludes the thesis by suggesting future experiments, specifically those of atmospheric relevance.

References

[1] R. Schinke. *Photodissociation Dynamics: Spectroscopy and Fragmentation of Small Polyatomic Molecules*. Cambridge University Press, Cambridge, 1993.

[2] M. Born and R. Oppenheimer. Zur quantentheorie der molekeln. *Annalen der Physik*, 389(20):457–484, 1927.

[3] P. J. Bruna and S. D. Peyerimhoff. *Excited-State Potentials*, pages 1–97. John Wiley & Sons, Inc., 2007.

[4] H. Köuppel, W. Domcke, and L. S. Cederbaum. *Multimode Molecular Dynamics Beyond the Born-Oppenheimer Approximation*, pages 59–246. John Wiley & Sons, Inc., 2007.

[5] M. N. R. Ashfold and J. D. Howe. Multiphoton spectroscopy of molecular species. *Annu. Rev. Phys. Chem.*, 45(1):57–82, 1994.

[6] R. N. Zare. My life with LIF: A personal account of developing laser-induced fluorescence. *Annu. Rev. Anal. Chem.*, 5(1):1–14, 2012. PMID: 22149473.

Chapter 2

Molecular Beam Apparatus

2.1 Overview

This chapter covers the experimental apparatus we use to study the dynamics and yields for $CHBrCl_2$ photodissociation in the $\tilde{A}$-band. Figure 2.1 depicts a cross section of the apparatus. The $CHBrCl_2$ parent is carried in a molecular beam to a laser-interaction region. There, an ultraviolet (UV) laser pulse initiates photodissociation and a second UV laser pulse ionizes the resulting photofragments. Electrodes guide the ions into a field-free time-of-flight mass spectrometer (TOF-MS). The detector at the end of the flight tube is capable of spatially resolving the impinging ions, which allows us to employ the velocity-map imaging technique (VMI).[1,2] The ensuing chapter will cover each of these components and the auxiliary aspects of the apparatus in detail.

The vacuum chamber was originally designed by Stephen Penn,[3] Carl Hayden, and Karen Carlson Muyskens.[4] Gail Thorson[5] made modifications to the TOF/MS, and Michael Hause[6] incorporated VMI capabilities. Thereafter, Heidi Yoon[7] upgraded the vacuum on the main chamber to a turbomolecular pump.

2.2 Vacuum system

The vacuum chamber consists of the three regions indicated in Figure 2.1: the source chamber, the main chamber, and the flight tube. Separate pumps evacuate each region to achieve differential pumping throughout the chamber. In the source chamber where the molecular

Figure 2.1: Diagram of the molecular beam apparatus vacuum chamber reproduced with permission from Amanda Case's thesis.[8] R, E, and G, are the repeller, extractor, and ground electrodes, respectively. The dot between the R and E electrodes is the laser-interaction region.

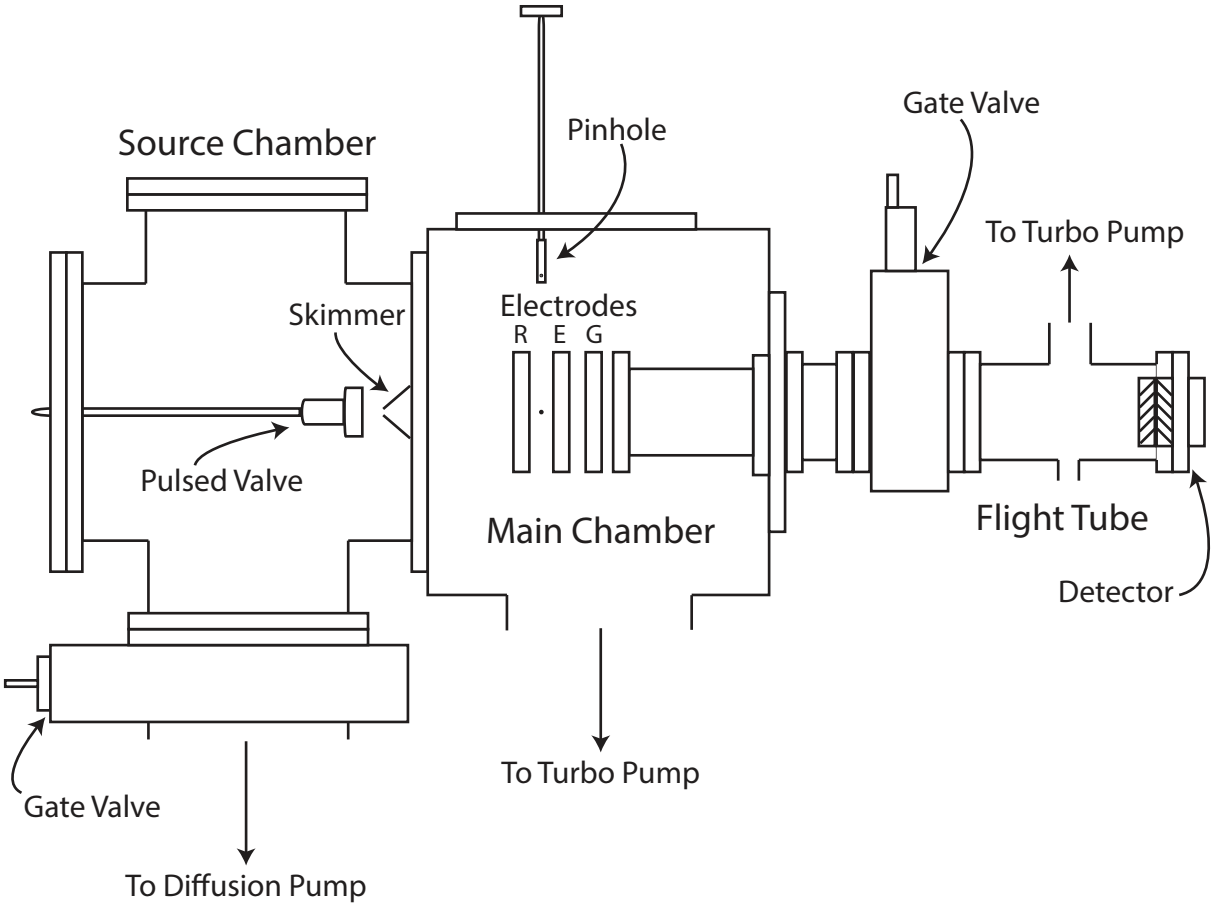
Source Chamber
Pinhole
Gate Valve
To Turbo Pump
Skimmer
Electrodes
R E G
Pulsed Valve
Main Chamber
Flight Tube
Detector
Gate Valve
To Turbo Pump
To Diffusion Pump

beam is formed, a 6-inch diameter diffusion pump (Varian, VHS-6) backed by a mechanical pump (Varian, SD-700) evacuates the region. The diffusion pump is connected to the source chamber through a liquid nitrogen trap to minimize oil contamination and a gate valve (Arico, 5010) that can seal the pump from the chamber. The main chamber, where the electrodes and the laser-interaction region are situated, is evacuated by a turbomolecular pump (Oerlikon Leybold, TurboVAC 600C) backed by a mechanical pump (Oerlikon Leybold, TRIVAC D25B). A second gate valve can seal off the flight tube. A second turbomolecular pump (Varian, TV-81M) backed by another mechanical pump (Varian, SD300) evacuates the flight tube. If power to the pumps is lost, interlocked solenoid valves shut automatically between the mechanical pumps and the turbomolecular pumps to prevent oil contamination.

Thermocouple gauges (Teledyne Hastings) measure foreline pressure, which is kept below 50 mTorr by the mechanical pumps. In the chamber, a capacitance manometer gauge (MKS Instruments, Bartaron) measures pressures above 10 mTorr, while Bayard-Apert type ion gauges (Kurt J. Lesker, G075TK) monitor the pressure below 10^{-4} Torr. A gauge controller (Granville-Phillips, Series 270) reads the pressure in each region of the apparatus. Table 2.1 summarizes typical operating pressures with the molecular beam on and off. These pressures are sufficient to generate stable expansion into the source chamber and a mean free path in the main chamber long enough to prevent molecule-molecule interactions.

Table 2.1: Typical pressures (in Torr) for the vacuum chamber with molecular beam on and off.

Molecular beam	Source chamber	Main chamber	TOF tube
off	$2 \cdot 10^{-7}$	$2 \cdot 10^{-7}$	$8 \cdot 10^{-8}$
on	$6 \cdot 10^{-6}$	$6 \cdot 10^{-7}$	$6 \cdot 10^{-7}$

2.3 Molecular beam formation

A gas manifold moves sample of the parent molecules into the vacuum chamber by way of supersonic expansion through a pulsed valve. The expansion passes through a skimmer en route to the laser-interaction region, forming the molecular beam. The following sections detail this process.

2.3.1 Gas manifold

A mechanical pump (Varian, SD-200) evacuates a gas manifold (stainless steel tubing, 0.25-inch OD) prior to sample preparation. Liquid samples are housed in a glass bubbler (Ace Glass), which is in line with the manifold and the pulsed valve. A freeze-pump-thaw cycle degases liquid samples before use. Gas samples are prepared in a mixing cylinder, typically with helium and a lecture bottle of the sample. A helium gas cylinder or the mixing cylinder pressurizes the manifold to ∼1200 Torr. In either case, helium is the carrier gas in the molecular beam. An ultratorr feedthrough takes the gas mixture from the manifold into the vacuum chamber to the pulsed valve.

2.3.2 Pulsed valve

The pulsed valve (General Valve, Series 9) generates a supersonic expansion of the sample through a 0.5-mm orifice in the source chamber, which efficiently cools the parent molecules rovibrationally. The valve consists of a Teflon armature and poppet and seals with a Kalrez o-ring. The pulsed valve is opened by a solenoid whose voltage is controlled by a home-built

driver operating at 20 Hz. A skimmer (Beam Dynamics, 1-mm diameter) passes the coldest region of the expansion from the source chamber to the main chamber. The skimmer is 11 cm from the laser-interaction region. The length between the pulsed valve and the skimmer is adjustable but is typically $\sim$3 cm.

2.4 Laser setup

We use two laser legs in our experiments, one for initiating photodissociation (the photolysis leg) and one for probing photofragments (the REMPI leg). Figure 2.2 depicts the two legs schematically. In both legs, the second harmonic of an Nd:YAG laser (Quanta-Ray, Lab 170 on the photolysis leg; Spectra Physics, DCR or Continuum, NY-81 on the REMPI leg) running at 20 Hz pumps a tunable dye laser (Continuum, ND6000). The output of the dye laser passes through two autotrackers (Inrad Optics, AT-II and AT-III), which generate second and third harmonics of the dye light with β-barium borate (BBO) crystals and maintain harmonic generation during wavelength scans.A $\lambda/2$ waveplate between the autotrackers ensures the correct polarization for third-harmonic generation. A harmonic separator (Inrad Optics) isolates the third harmonic from the second harmonic and the dye fundamental. A second $\lambda/2$ waveplate sets the polarization of the light to be perpendicular to the molecular beam and parallel to detector, which is necessary for the VMI analysis we perform. Ultimately, the setup generates UV light between 300 and 400 nm with less than 0.5 mJ/pulse on both legs. The two beams are sent into opposite sides of the vacuum chamber through UV-grade CaF_2 windows with teflon baffles on the interior side to minimize laser scatter. Lenses (300-mm and 500-mm focal lengths for the photolysis and REMPI leg,

Figure 2.2: Schematic of the laser setup used for the molecular beam apparatus. On both legs, the second harmonic of the Nd:YAG laser pumps a tunable dye laser. BBO crystals (labeled HG) generate the second and third harmonics of the dye laser output, which are separated by a harmonic separator before passing into the source chamber.

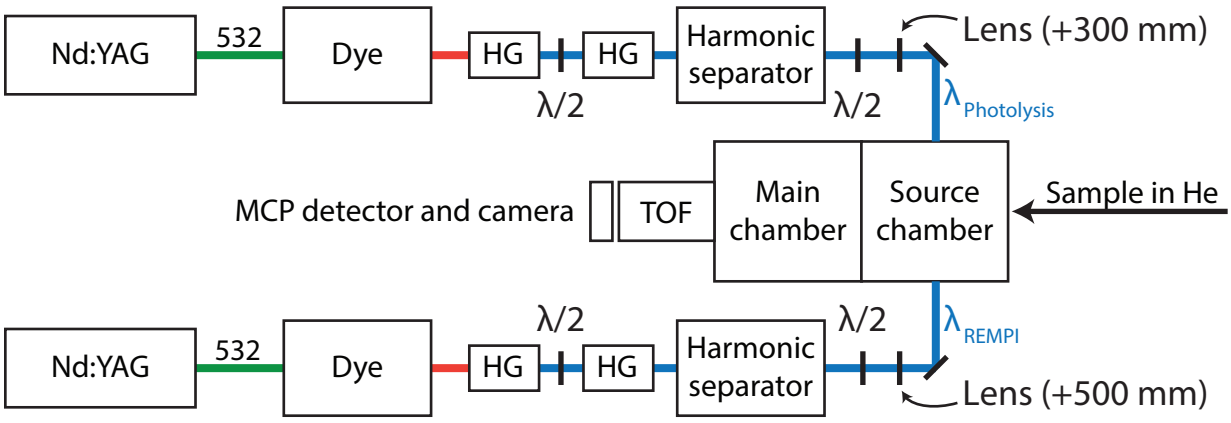
Nd:YAG
532
Dye
HG
HG
λ/2
Harmonic separator
λ/2
Lens (+300 mm)
λ Photolysis
MCP detector and camera
TOF
Main chamber
Source chamber
Sample in He
Nd:YAG
532
Dye
λ/2
HG
HG
Harmonic separator
λ/2
λ REMPI
Lens (+500 mm)

respectively) focus the light into the laser-interaction region. We use a retractable pinhole in the laser-interaction region to achieve optimal spatial overlap between the two beams.

A wavemeter (Coherent, WaveMaster) with 0.001 nm resolution and 0.005 nm accuracy calibrates the dye laser wavelength. The wavelength of the dye laser is changed by adjusting the angle of the end mirror in the oscillator cavity, which is achieved with a stepper motor. The motor is controlled by LabView code written by Cornelia Heid.[9] The code also reads in the wavemeter output through a serial port on the computer. The computer communicates with the stepper motor using a stepper control card in a PCI slot (National Instruments, PCI-7334) *via* a 68-pin I/O connector block (National Instruments, CB-68-LP). The connector block allows both dye lasers to communicate with the control card.

2.5 Detection

We employ TOF-MS for mass detection of the ions generated by REMPI. This routine mass spectrometric technique relies on the velocity different ions reach in an electric field of known strength due to their mass-to-charge ratios, which manifests as a unique flight time associated with a particular mass. The electric field for the TOF-MS is generated by ion optics with 2.25-inch diameter circular apertures that make the VMI technique possible.[1,2] The ion optics generate an inhomogeneous electric field that can focus the ionized photofragments by velocity onto a 2-D detector at the end of the TOF-MS flight tube. The following sections will detail the components of the TOF-MS and VMI detection.

2.5.1 Time-of-flight mass spectrometry

Three electrodes generate the electric field that guides ionized photofragments to the detector. The repeller electrode (R in Figure 2.1) kept at 2.56 kV is situated between the skimmer and the laser-interaction region. The opposite side of the laser-interaction region contains the extractor (E) and ground (G) electrodes at 1.80 and 0 kV, respectively. The potential energy E_p the electrodes impart on the ions is given by

$$E_p = qU \tag{2.1}$$

where q is the ion charge and U is the electric field strength. The ions accelerate in the field and E_p is converted to kinetic energy,

$$qU = \frac{1}{2}mv^2 \tag{2.2}$$

or

$$v = \sqrt{\frac{2qU}{m}} \tag{2.3}$$

where m is the ion mass and v is its velocity. Thus, within the field generated by the ion optics, ions with different mass-to-charge ratios will reach different velocities. These differing velocities lead to distinct residence times in the field-free flight tube region of the vacuum chamber before impinging on the detector. The detector is a chevron-style dual microchannel plate (MCP) phosphor screen assembly (Photonis, APD 3040FM). Impinging ions set off a cascade of electrons in the MCPs that collide with the phosphor screen, causing it to glow. An anode on the phosphor screen is wired through a home-built capacitor box, which picks off the low-voltage signal from the high-voltage phosphor screen output. A BNC cable runs the low-voltage signal to a boxcar averager (Stanford Research Systems, SR250),

which allows us to set an integration gate on the mass channel of interest. A 500 MHz digital oscilloscope (LaCroy, Waverunner LT372) allows us to visualize the mass peak and set the boxcar gate appropriately.

A pulse generator (Directed Energy, PVM 4140) applies voltage to the MCPs only during the arrival time for the mass channel of interest, which extends the lifetime of the MCPs and improves the background noise. To prevent arcing between the MCPs and the phosphor screen, we hold the second MCP at a base voltage of 1.4 kV and pulse it to 1.8 kV with the pulse generator. We ground the front MCP and keep the phosphor screen at a constant 3.0 kV. A home-built 2-MΩ shunt resistor circuit prevents voltage flow between the high and low voltage ports of pulse generator.

The integrated signal from the boxcar averager is sent to the computer as analog signal through a home-built breakout box. The breakout box consists of BNC connectors and a 68-pin I/O connector block (National Instruments, CB-68-LP) that connects to the motherboard of the computer through a DAQ card (National Instruments, PCI-6024E). The DAQ card converts the analog signal to digital signal and the LabView code described in Cornelia Heid's thesis records the signal as data.[9] The LabView code described in Chapter 4 has similar functionality insofar as analog data acquisition is concerned, so the reader should refer to that section as well as Cornelia Heid's thesis for the code specific to the TOF-MS experiments.

2.5.2 Velocity-map imaging

The theses of Michael Hause[6] and Amanda Case[8] contain more detail about the VMI setup than is given here. Nonetheless, a review of the methodology and the components of the setup follow. Figure 2.3 depicts the VMI technique schematically. The essential feature of VMI is that it spatially maps the velocities of the recoiling photofragments onto the detector such that a pixel-to-energy calibration can recover the kinetic energy of the fragments. Conservation of energy then gives the internal energy of the photofragments. VMI signal may appear as discrete rings on the detector corresponding with particular rovibrational states, although vibrational resolution is not guaranteed.

2.5.2.1 Focusing by velocity

The electron cascade generated through the MCPs when an ion arrives is spatially localized on the 2-D detector, such that the phosphor screen where the electrons strike after leaving the MCPs glows in the same spot as the impinging ion. An image of the glowing phosphor screen is captured by a CCD camera (LaVision, Imager 3QE) through a 28-mm lens (Nikkon, Nikkor AF 28 mm), producing a digital image. We optimize the ion optics such that all photofragments recoiling with a particular velocity are focused onto the same pixel in the digital image, which minimizes blurring due to the beam waist of the laser. This optimization is performed by ionizing NO with a (1 + 1) REMPI scheme through the $\tilde{A}$-state, which appears as a small dot on the center of the detector. We then minimize the size of this dot by adjusting the voltages on the ion optics.

Figure 2.3: Schematic representation of the velocity-map imaging technique. The photolysis laser initiates photodissociation, and the photofragments recoil in three dimensions. The 3-D distibution of recoiling photofragments is ionized by the REMPI laser and guided by an electric field to the 2-D detector. Software reconstructs the 3-D distribution from the 2-D projection by exploiting the symmetry inherent in the detection method. Pixel-to-energy conversion derived from a well-characterized system then generates kinetic energy distributions.

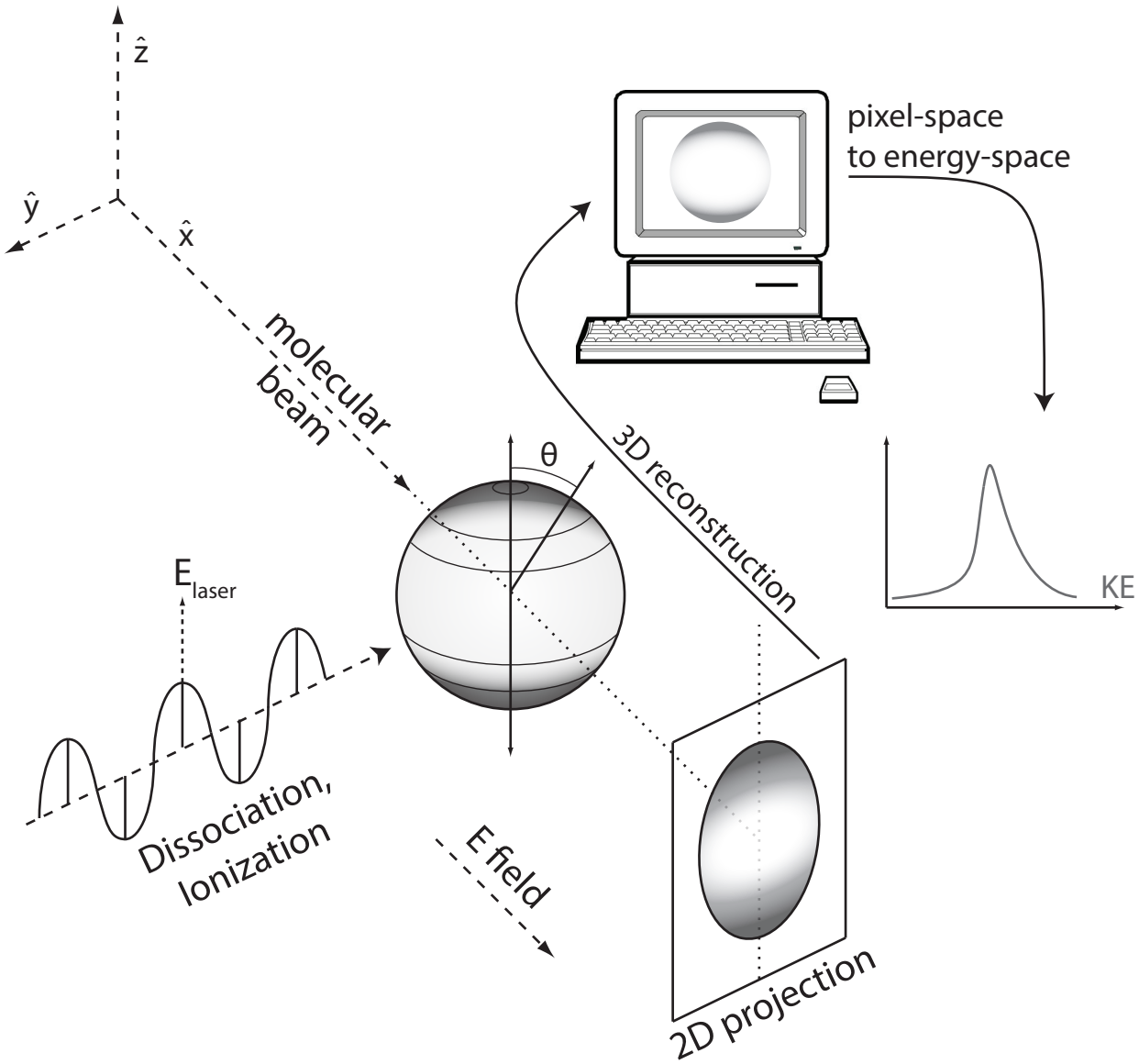
ẑ
ŷ
x̂
molecular
beam
pixel-space
to energy-space
3D reconstruction
θ
KE
E laser
Dissociation,
Ionization
E field
2D projection

2.5.2.2 Imaging and reconstruction

By integrating the images generated by successive laser shots, we generate a 2-D mapping of the velocities of the recoiling photofragments. The DaVis software package collects and integrates these images, and we refer to the mapping at this stage as a "raw image." The raw image is "reconstructed" by the BASEX software package, yielding the 3-D velocity distribution from the 2-D image.[10] Figure 2.4 shows a raw and reconstructed image of O^+ following O_2 dissociation (more on this in Section 2.5.2.3). The BASEX program exploits the cylindrical symmetry present in the 3-D Newton sphere to unambiguously reconstruct the distribution from the 2-D projection parallel to the symmetry axis. The polarization of the lasers described in section 2.4 ensures that this symmetry axis exists, and that it is parallel to the detector. A thin center slice of the 3-D distribution is produced from this process that we refer to as the "reconstructed image." BASEX generates a radial distribution of the ion signal by integrating over all angles of the reconstructed image at each pixel away from the image center. It also provides plots of the intensity as a function of angle at each radius, which shows the anisotropy present in the VMI data. If the timescale for dissociation is shorter than a rotational period for the parent, the anisotropy contains information about the transition dipole orientation relative to the polarization of the laser, and thus, about the excited states accessed upon photon absorption.

2.5.2.3 Kinetic energy distributions

The radial distribution of ion signal generated by BASEX is not quantitatively useful without a pixel-to-energy calibration from a well-characterized dissociation. We convert the pixel

Figure 2.4: Velocity map images and total kinetic energy release for O_2 dissociation following $(2+1)$ excitation at 225 nm through the $3d\pi(^3\Sigma_{1g}^-)$ Rydberg state to produce highly excited O_2. The excited O_2 can autoionize or dissociate to form ground- and excited-state O atoms. An additional photon ionizes the excited O atom to generate the cations we image. (A) is the raw image and (B) is the reconstructed image. (C) is the kinetic energy distribution we use to discern M in Equation 2.4.

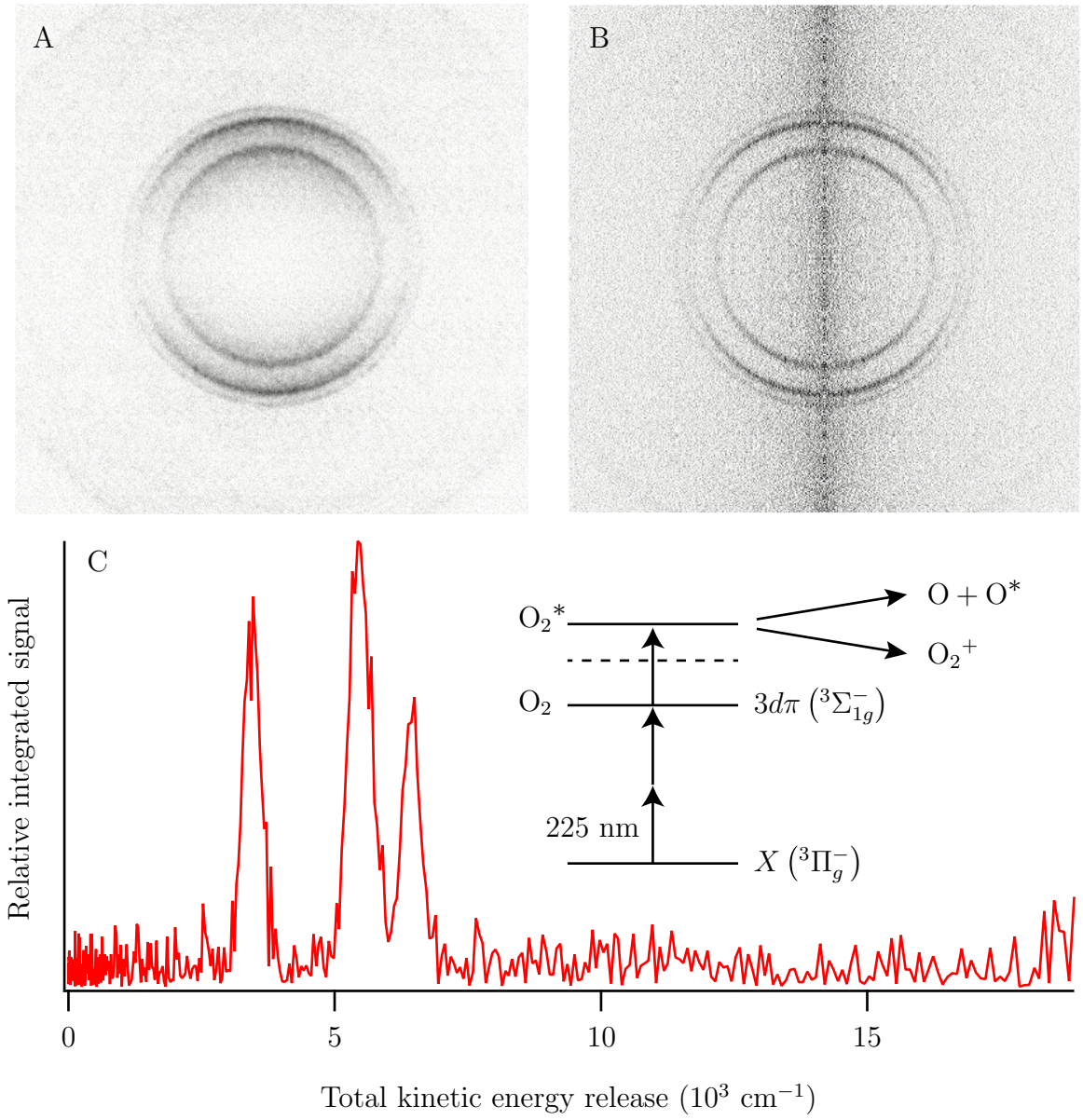
A
B
C
Relative integrated signal
O_2^*
$O + O^*$
O_2^+
O_2
$3d\pi\ (^3\Sigma_{1g}^-)$
225 nm
$X\ (^3\Pi_g^-)$
0
5
10
15
Total kinetic energy release (10^3 cm^{-1})

number N_{pix} to the detected fragment velocity v_d with

$$v_d(N_{pix}) = \frac{s_{pix} N_{pix} M}{t_{TOF}} \tag{2.4}$$

where s_{pix} is the size of a pixel, t_{TOF} is the ion flight time, and M is the magnification factor of the VMI setup that we determine from a well-characterized dissociation. The kinetic energy of the detected fragment KE_d is then

$$KE_d = \frac{1}{2} m_d v_d^2 \tag{2.5}$$

where m_d is the mass of the detected fragment. To obtain the total kinetic energy $TKER$ of *both* recoiling photofragments, conservation of energy and momentum is invoked to give

$$TKER = KE_d \frac{m_p}{m_u} \tag{2.6}$$

where m_p is the mass of the parent and m_u is the mass of the undetected fragment. The corresponding ion signal $f(v)$ must also be transformed from velocity space to energy space. This requires the Jacobian. The differential in velocity space

$$f(v)dv = f(KE)dKE \tag{2.7}$$

is equal to the differential in energy space. By substitution,

$$f(KE) = \sqrt{\frac{1}{2mKE}} f(v) \tag{2.8}$$

where $(2mKE)^{-1/2}$ is the Jacobian. For our VMI setup, s_{pix} is 6.45 μm. M is the only factor that needs to be determined for the pixel-to-energy conversion. We used the photodissociation of O_2 to achieve this, which is described in detail in Michael Hause's thesis.[6] Briefly, a two-photon 225-nm absorption takes O_2 to the $4s$-$3d\pi(^3\Sigma_{1g}^-)(v = 2, N = 2)$ Rydberg state,

and a third photon creates a highly excited O_2* state. From there, two basic events can occur: the O_2 autoionizes to form the O_2^+ cation, or the O_2* dissociates into ground- and excited-state O atoms.[11] A fourth photon can then ionize the excited-state O atom, or dissociate the O_2^+ cation. We image the resulting O^+ cations and assign the first strong peak as the ground state O + O(^3P) channel. Figure 2.4 shows the images and resulting TKER profile for this callibration.

The conversion from the BASEX reconstruction to the TKER profiles is achieved with a MATHCAD script that Michael Hause wrote.[6] With state-selective ionization and TKER measurements, we then obtain distributions of internal energy $E_{int,u}$ for the unmeasured fragment through energy conservation. That is,

$$E_{int,u} = h\nu - D_0 - E_{int,m} - TKER \tag{2.9}$$

where D_0 is the energy of the bond being cleaved and $E_{int,m}$ is the internal energy of the measured photofragment, which is known because REMPI ensures that only fragments in a particular quantum state are ionized for a given image.

2.6 Timing and synchronization

We synchronize the timing of the laser flash lamps, the laser Q-switches, the pulsed valve, the MCP pulser, and the boxcar integrator using two daisy-chained digital delay generators (Stanford Research Systems, DG535). Time zero (T_0) is internally generated by the first delay generator (DDG 1) and passed as an external trigger for the second delay generator (DDG 2). Table 2.2 provides a summary of the channel assignments and delay times for DDG 1 and DDG 2. The time delays we list in Table 2.2 between the lamps and the Q-

switch for the Nd:YAG lasers maximize power for a Lab 170 laser, but we use different time delays occasionally to reduce the laser power and on other Nd:YAG lasers.

Table 2.2: Timing assignments for DDG 1 and DDG 2 and typical time delays relative to the internal trigger for DDG 1 (T_0).

DDG 1		
Channel	Assignment	Time delay (ms)
A	Boxcar	3.143295
B		3.143367
C	Pulsed valve	2.300000
D	No Connection	
A/B	Pulser	
DDG 2		
Channel	Assignment	Time delay (ms)
A	Nd:YAG lamps (REMPI leg)	B-0.180
B	Nd:YAG Q-switch (REMPI leg)	3.138085
C	Nd:YAG lamps (Photolysis leg)	D-0.180
D	Nd:YAG Q-switch (Photolysis leg)	3.137867
C/D	Oscilloscope	

References

[1] D. W. Chandler and P. L. Houston. Two-dimensional imaging of state-selected photodissociation products detected by multiphoton ionization. *J. Chem. Phys.*, 87(2):1445–1447, 1987.

[2] A. T. J. B. Eppink and D. H. Parker. Velocity map imaging of ions and electrons using electrostatic lenses: Application in photoelectron and photofragment ion imaging of molecular oxygen. *Rev. Sci. Instrum.*, 68(9):3477–3484, 1997.

[3] S. Penn. *Low-energy electron-impact ionization techniques for the study of photofragmentation dynamics and vibrational overtone excitation.* PhD thesis, University of Wisconsin, 1987.

[4] K. Carlson Muyskens. *The photodissociation of nitromethane using energy-selective electron impact ionization and time-of-flight spectrometry.* PhD thesis, University of Wisconsin, 1987.

[5] G. Thorson. *Dimethyl sulfoxide photodissociation studies in a molecular beam: determining photofragment energy distributions and dissociation pathways.* PhD thesis, University of Wisconsin, 1991.

[6] M. Hause. *Influence of vibrations on passage through conical intersections: velocity map imaging of the photodissociation of ammonia and phenol.* PhD thesis, University of Wisconsin, 2007.

[7] Y. H. Yoon. *Characterization and vibrationally mediated photdissociation of jet-cooled formic acid dimer and phenol-carbon monoxide complexes.* PhD thesis, University of Wisconsin, 2007.

[8] A. S. Case. *Vibrational predissociation of the ammonia dimer.* PhD thesis, University of Wisconsin, 2011.

[9] C. G. Heid. *Vibrational predissociation dynamics of the ammonia trimer and the 3-aminophenol-ammonia complex.* PhD thesis, University of Wisconsin, 2014.

[10] V. Dribinski, A. Ossadtchi, V. A. Mandelshtam, and H. Reisler. Reconstruction of abel-transformable images: The gaussian basis-set expansion abel transform method. *Rev. Sci. Instrum.*, 73(7):2634–2642, 2002.

[11] D. H. Parker and A. T. J. B. Eppink. Photoelectron and photofragment velocity map imaging of state-selected molecular oxygen dissociation/ionization dynamics. *J. Chem. Phys.*, 107(7):2357–2362, 1997.

Chapter 3

$CHBrCl_2$ Photodissociation Studies

3.1 Introduction

If you read enough literature on photodissociation, you find "ubiquitous" is a rather ubiquitous word, and not without reason. Photodissociations of ostensibly simple systems such as HI, H_2O, or CH_3I have been test-cases for countless experimental and theoretical techniques spanning many decades. We rely on insights from those investigations as the foundation for studying related systems with increasing complexity, which often exhibit similar motifs in electronic structure, dynamics, scattering, etc. But even the aforementioned test-cases can feature a healthy degree of complexity, such as nonadiabatic transitions, strong spin-orbit coupling, or highly excited product states. Adding or changing substituents can exacerbate this complexity quite easily. Indeed, even the most ubiquitously studied classes of compounds present a challenge to modern *ab initio* predictions of photodissociation.

Halomethanes, in particular CH_3I, are the five-atom photodissociation target of choice for many studies.[1–10] Carbon-halogen bonds tend to be relatively weak and resonance-enhanced multiphoton ionization (REMPI) detection schemes are well characterized for the halogen photofragments. The $\tilde{A}$-band for halomethanes consists of $\sigma^* \leftarrow n$ transitions localized on the carbon-halogen bond leading to characteristically prompt dissociation. Morokuma and coworkers[11] have calculated full-dimensional potential energy surfaces (PES) for the CH_3I $\tilde{A}$-band, and measurements of dynamics and energy disposal following C–I bond cleavage have characterized CH_3I photodissociation in great detail. Although $\sigma^* \leftarrow n$ transitions to a

number of excited electronic states are possible, in CH_3I the $^3Q_{0^+}(2A_1)$ transition dominates the $\tilde{A}$-band absorption. The $^3Q_{0^+}(2A_1)$ state correlates diabatically with spin-excited iodine products, but an avoided crossing region facilitates the production of ground-state iodine.

This chapter covers the results of photodissociation experiments on $CHBrCl_2$ in the molecular beam apparatus.[12] There are similarities to CH_3I photodissociation, but a number of differences make $CHBrCl_2$ a more complicated system, and studies on trisubstituted halomethane photodissociations are sparse. A previous study on $CHBrCl_2$ characterized vacuum ultraviolet absorption and fluorescence from 106–200 nm,[4] and another determined the UV absorption cross-section from 210–320 nm.[13] A third study investigated multiphoton dissociation pathways for $CHBrCl_2$ at 266 nm and showed that Cl-atom production results from subsequent $CHCl_2$ photodissociation following the initial C–Br bond cleavage.[14] Building on the wealth of data for CH_3I and other halomethanes, we consider how differences in symmetry, excited electronic states, spin-orbit coupling, and nonadiabatic transitions influence the dynamics and product yields for $CHBrCl_2$ photodissociation over a broad range (215–265 nm) of photolysis wavelengths. Figure 3.1 shows the structure of $CHBrCl_2$ and the mirror plane through the H, C, and Cl atoms.

3.2 The $CHBrCl_2$ $\tilde{A}$-band

In $CHBrCl_2$, $\tilde{A}$-band absorption cleaves the C–Br bond, resulting in two distinct product channels

$$CHBrCl_2 \xrightarrow{h\nu} CHCl_2 + Br \tag{3.1}$$

$$CHBrCl_2 \xrightarrow{h\nu} CHCl_2 + Br^* \tag{3.2}$$

Figure 3.1: Structure of $CHBrCl_2$ with superimposed mirror plane through the H, C, and Cl atoms.

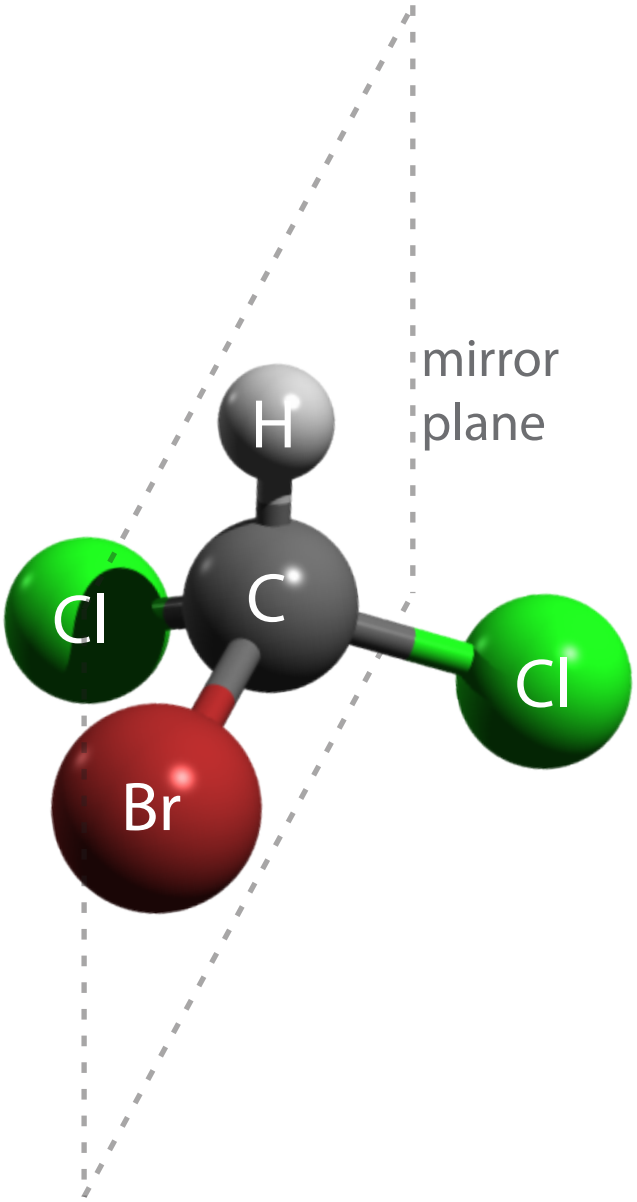
mirror
plane
H
C
Cl
Cl
Br

where Br is in the $4p^2P_{3/2}$ (ground) quantum state and Br* is in the $4p^2P_{1/2}$ (spin-orbit excited) quantum state. Figure 3.2 shows the REMPI scheme we use to selectively probe the two exit channels.[15]

Like CH_3I, there is a singlet to triplet transition to ${}^3Q_{0^+}(A')$ that correlates diabatically to Br* and an avoided crossing region with ${}^1Q_1(A')$ alters this exit channel correlation in adiabatic representation. Figure 3.3 demonstrates the similarity between the $CH3I$ and $CHBrCl2$ Ã-band. Unlike CH_3I, we cannot assume that excitation to the ${}^3Q_{0^+}(A')$ state will dominate absorption in the Ã-band. Spin-orbit interaction increases with atomic number, so heavier atoms like iodine exhibit stronger coupling than bromine. The spin-selection rule, which dictates that $\Delta s = 0$ for electronic transitions, is derived in the limit of small spin-orbit coupling. Thus, the especially strong coupling present in iodine is responsible for the nearly exclusive singlet to triplet transition in the CH_3I Ã-band. Studies of CH_3Br attribute the lower-energy portion of the Ã-band to ${}^3Q_{0^+}$ and ${}^3Q_1$ transitions, while the higher-energy portion is due to the ${}^1Q_1$ transitions.[8] Transition strengths to the ${}^3Q_{0^+}$ and ${}^1Q_1$ states in CH_2BrCl are similar throughout the Ã-band.[16]

The symmetry of $CHBrCl_2$ presents additional nuance. $CHBrCl_2$ belongs to the C_s symmetry group, having a mirror plane as its only symmetry element. Figure 3.3 demonstrates the differing Ã-band electronic states in a C_{3v} molecule (such as CH_3I) without spin-orbit coupling, a C_{3v} molecule with spin-orbit coupling, and a C_s molecule with spin-orbit coupling. Without spin-orbit coupling, only transitions to the ${}^1E$ state are permitted. The spin-orbit interaction splits the ${}^3E$ state, and a number of transitions are possible, although A_1 to A_2 symmetry transitions are dipole forbidden. C_s symmetry lifts the degeneracy of the E states into A' and A'' states, and there are no forbidden transitions.

Figure 3.2: REMPI scheme we use to detect Br and Br* photofragments. λ_{REMPI} at 263.80 nm ionizes Br *via* the $5p^4P_{1/2}$ intermediate state. λ_{REMPI} at 263.12 nm ionizes Br* *via* the $5p^4D_{3/2}$ intermediate state.

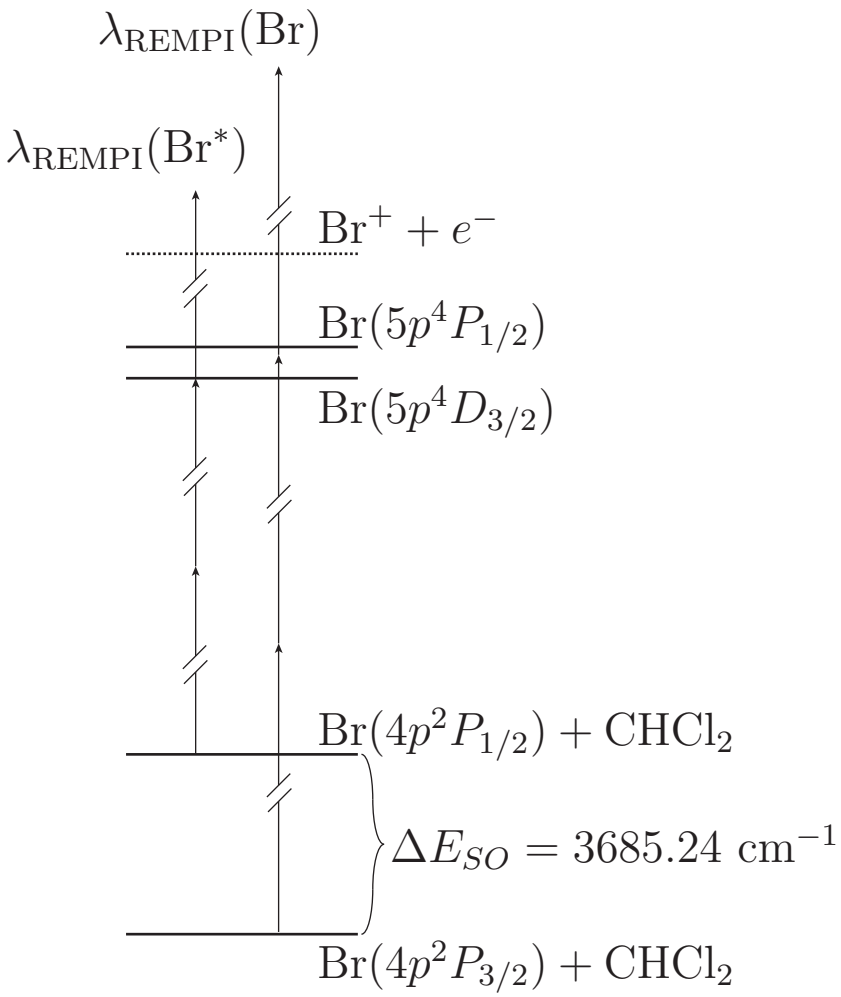
$\lambda_{\mathrm{REMPI}}(\mathrm{Br})$
$\lambda_{\mathrm{REMPI}}(\mathrm{Br}^*)$
$\mathrm{Br}^+ + e^-$
$\mathrm{Br}(5p^4P_{1/2})$
$\mathrm{Br}(5p^4D_{3/2})$
$\mathrm{Br}(4p^2P_{1/2}) + \mathrm{CHCl_2}$
$\Delta E_{SO} = 3685.24\ \mathrm{cm}^{-1}$
$\mathrm{Br}(4p^2P_{3/2}) + \mathrm{CHCl_2}$

Figure 3.3: Diabatic correlation diagram of $CHBrCl_2$ photodissociation. States of $CHBrCl_2$ are labeled in green, which account for spin–orbit coupling (SOC) and the intrinsic C_s symmetry of the molecule. Line weights qualitatively indicate anticipated oscillator strengths, and dashed lines indicate forbidden transitions. Inset: Enlarged rendering of the crossing region with adiabats (broken lines) forming an avoided crossing which changes the correlation of the A′ states. The $^3Q_{0^+}(\mathrm{A}')$ state (blue) correlates diabatically with Br^* products, but interaction with the $^1Q_1(\mathrm{A}')$ state (red) creates a dissociation channel of mixed-spin character leading adiabatically to Br production and nonadiabatically to Br^* from $^3Q_{0^+}(\mathrm{A}')$. The $^1Q_1(\mathrm{A}'')$ state retains its correlation with Br given that there are no nearby A″ states in the region to induce mixing.

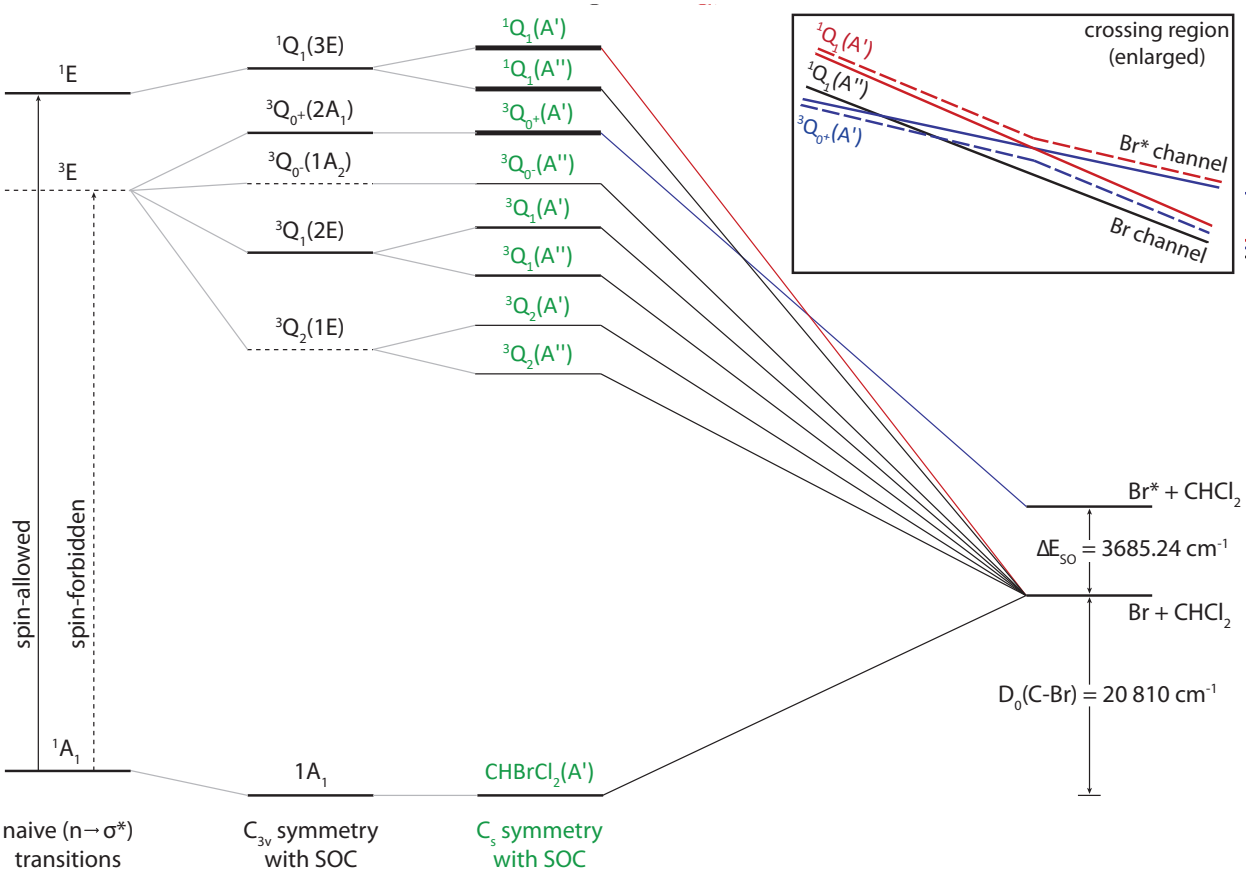
^{1}E
^{3}E
^{1}A$_1$
spin-allowed
spin-forbidden
^{1}Q$_1$(3E)
^{3}Q$_{0^+}$(2A$_1$)
^{3}Q$_{0^-}$(1A$_2$)
^{3}Q$_1$(2E)
^{3}Q$_2$(1E)
1A$_1$
^{1}Q$_1$(A')
^{1}Q$_1$(A'')
^{3}Q$_{0^+}$(A')
^{3}Q$_{0^-}$(A'')
^{3}Q$_1$(A')
^{3}Q$_1$(A'')
^{3}Q$_2$(A')
^{3}Q$_2$(A'')
CHBrCl$_2$(A')
crossing region
(enlarged)
^{1}Q$_1$(A')
^{1}Q$_1$(A'')
^{3}Q$_{0^+}$(A')
Br* channel
Br channel
Br* + CHCl$_2$
ΔE$_{SO}$ = 3685.24 cm^{-1}
Br + CHCl$_2$
D$_0$(C-Br) = 20 810 cm^{-1}
naive (n→σ*)
transitions
C$_{3v}$ symmetry
with SOC
C$_s$ symmetry
with SOC

The $^3Q_{0^+}(A')$ diabat crosses the $^1Q_1(A')$ and $^1Q_1(A'')$ diabats. Only states of the same symmetry can form an avoided crossing, so adiabatic treatment of the $^3Q_{0^+}(A')$ and $^1Q_1(A')$ states alters their exit channel correlation, while the $^1Q_1(A'')$ retains its correlation with the ground-state exit channel.

Objectives of our study include determining which Ã-band states are accessed as a function of photolysis energy as well as how the dynamics in the crossing region influence the relative quantum yields of the two exit channels and the internal energy deposited in the $CHCl_2$ fragment. We use REMPI detection (Section 1.1.5.1) of the Br and Br* fragments and the velocity map imaging (VMI) technique (Section 2.5.2) to pursue these objectives.

3.3 Energy Partitioning

When the $CHBrCl_2$ parent absorbs a photon of energy $h\nu$, some of that energy is used to break the C−Br bond, but since the recoiling photofragments are not thermalized, it is not obvious *a priori* how the remaining energy will partition among translational energy, Br spin-orbit excitation, and $CHCl_2$ internal energy. We assume that the expansion conditions in our molecular beam cool the sample rovibrationally, so that all of the available energy comes from the absorbed photon. That is,

$$h\nu = D_0 + E_{trans} + E_{SO} + E_{int} \tag{3.3}$$

where D_0 is the C−Br bond energy, E_{trans} is the translational energy of the recoiling photofragments, E_{SO} is the spin-orbit excitation of the Br fragment, and E_{int} is the internal energy of the $CHCl_2$ fragment. Thermochemical data[17] give $D_0 = 20810$ cm^{-1}, and E_{SO}

is zero for Br and 3685.24 cm^{-1} for Br*.[18] VMI measurements account for E_{trans} (Section 2.5.2), and E_{int} is therefore obtained through energy conservation.

Figure 3.3.1 shows the distribution of internal energy for the $CHCl_2$ fragment for both exit channels at each photolysis wavelength. We fit the distributions with Gaussian profiles and take the peak of the fit to be the most probable internal energy E_{int}^{mp}. Figure 3.5 shows plots of E_{int}^{mp} and the corresponding most probable translational energy E_{trans}^{mp} as a function of photolysis energy. Fractional energy in Figure 3.5 divides the absolute energy measurements by the leftover energy available after bond cleavage for a given exit channel. Table 3.1 summarizes the values appearing in Figures 3.3.1 and 3.5 and provides the width at half maximum (FWHM) for the Gaussian fits.

The distinct similarity between E_{trans}^{mp} for the two exit channels at each photolysis energy shows that Br spin-orbit excitation comes largely at the expense of E_{int}. There is perhaps a very slight increase in the fraction of energy deposited into translation at higher photolysis energies, but partitioning is nearly constant over all the photolysis energies we investigated. This is consistent with an "impulsive" dissociation, which Section 3.6 will discuss at length.

3.3.1 Kinematic particulars

One of the more evident features of the $CHCl_2$ internal energy distributions is a high degree of internal excitation. In virtually every case, E_{int} is well above the zero-point energy for $CHCl_2$ (3238 cm^{-1}) but below the energy necessary for electronic excitation.[19,20] Therefore, photodissociation imparts a large amount of rotational and/or vibrational energy to the $CHCl_2$ fragment. Unfortunately, the VMI measurements do not resolve vibrational structure,

Figure 3.4: Internal energy distributions for the $CHCl_2$ photofragments with Br (bottom) and Br^* (top) partner fragments. Photolysis wavelength decreases in 10 nm increments from left (265 nm, red) to right (215 nm, purple).

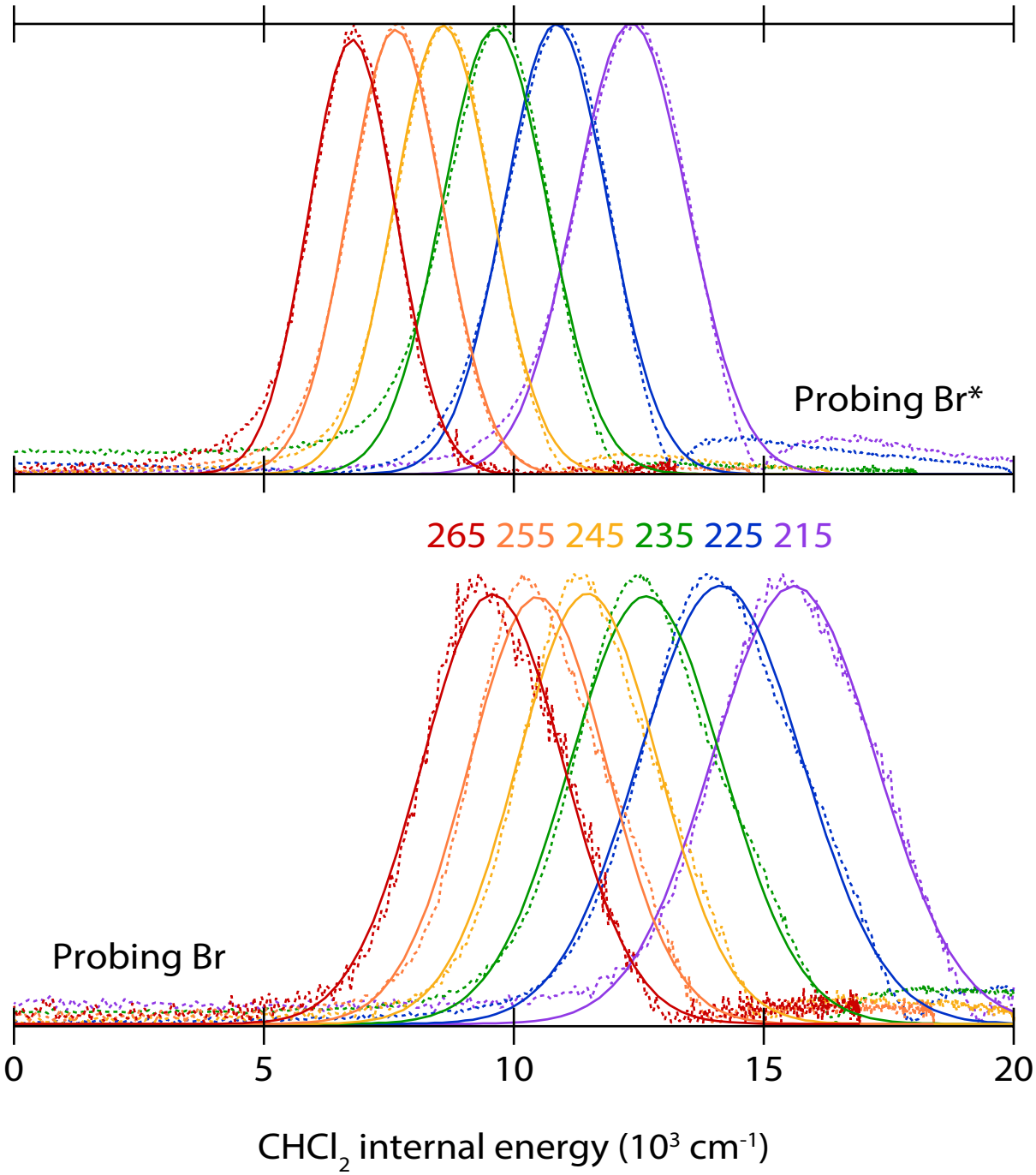
Probing Br*
265 255 245 235 225 215
Probing Br
0
5
10
15
20
CHCl2 internal energy (10³ cm⁻¹)

Figure 3.5: Product energy partitioning at each photolysis wavelength (a) as a fraction of available energy and (b) as a total. Data for the Br channel is in red and for the Br^* channel is in blue. The solid triangles correspond with total translational energy, and the open circles correspond with $CHCl_2$ internal energy.

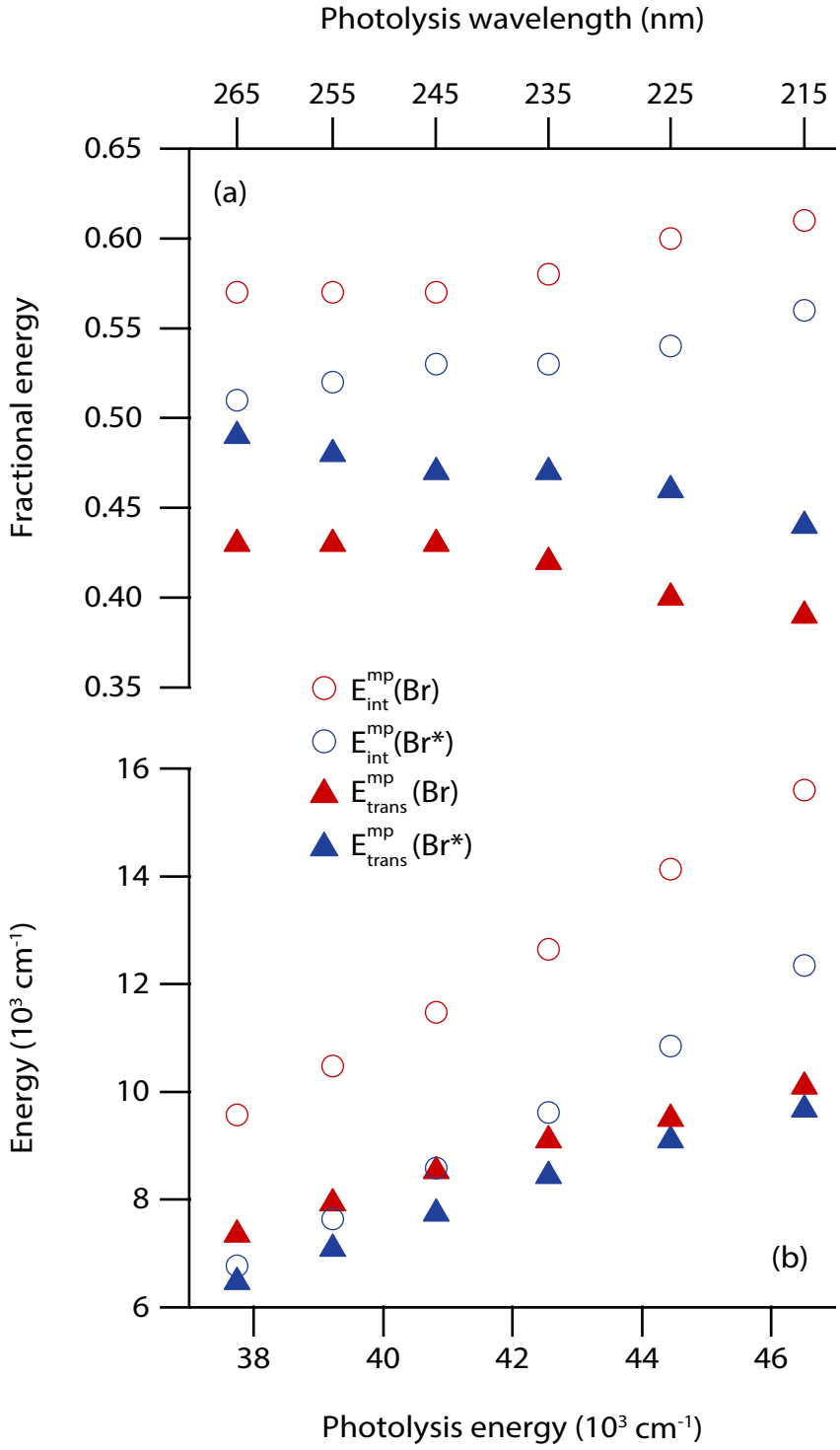
Photolysis wavelength (nm)
265
255
245
235
225
215
0.65
0.60
0.55
0.50
0.45
0.40
0.35
(a)
Fractional energy
E_{int}^{mp}(Br)
E_{int}^{mp}(Br*)
E_{trans}^{mp}(Br)
E_{trans}^{mp}(Br*)
16
14
12
10
8
6
Energy (10^3 cm^{-1})
(b)
38
40
42
44
46
Photolysis energy (10^3 cm^{-1})

Table 3.1: Summary of the translational energy disposal gleaned from VMI data. The most probable translational energy (E_{trans}^{mp}) refers to the peak of the Gaussian fit of the reconstructured VMI data, and FWHM refers to the width at half maximum of that Gaussian. E_{avl} refers to the available energy for a given exit channel following C−Br bond cleavage.

$\lambda_{\text{photolysis}}$ (nm)	Br state	E_{avl} (cm^{-1})	E^{mp}_{trans} (cm^{-1})	E^{mp}_{trans}/E_{avl}	FWHM (cm^{-1})
215	Br	25700	10100	0.39	3860
	Br*	22000	9670	0.44	2640
225	Br	23600	9500	0.40	3840
	Br*	19900	9100	0.46	2420
235	Br	21700	9100	0.42	3610
	Br*	18100	8440	0.47	2480
245	Br	20000	8530	0.43	3330
	Br*	16300	7740	0.47	2300
255	Br	18400	7930	0.43	3250
	Br*	14700	7080	0.48	2220
265	Br	16900	7350	0.43	3330
	Br*	13200	6470	0.49	2050

but we can still rationalize internal excitation on kinematic grounds.

We suggest a high degree of rotational excitation is present by way of comparison with CH_3I. Fast dissociation imparts mostly translational energy into the relatively light methyl fragment in CH_3I. C_{3v} geometry ensures that C−I repulsion is collinear with the methyl fragment center of mass, so impulsive excitation of CH_3 rotations is unlikely, and this is borne out in data from numerous studies. On the other hand, the $CHCl_2$ fragment center of mass is not along the C−Br bond axis in the parent molecule, and this arrangement results in considerably more torque accompanying bond cleavage. We will consider this rotational excitation in detail using impulsive modeling and comparison with reports of other C_s-symmetry halomethane dissociations in Section 3.6.

3.3.2 Internal excitation due to curve crossing and PES topology

The two exit channels for $CHBrCl_2$ lead to distinct $CHCl_2$ internal energy distributions. The ground-state Br channel leads to partner fragments with wider distributions centered at higher energies. We again begin with CH_3I studies to consider the origin of these exit-channel specific dynamics. Detailed *ab initio* studies[11,21] of CH_3I show that rotational energy builds up on the $^3Q_{0^+}$ diabat as the geometry evolves towards the crossing region, but persists in the methyl fragment only for trajectories that cross to the $^1Q_1$ diabat to produce ground-state I. This effect is due to the differing topology of the PES in the two exit channels. The exit channel leading to spin-orbit excited I is steeper with respect to the C−H−I bending motion, which hampers rotation. The relatively flat ground-state exit channel sustains the rotational excitation, consistent with the measurements of E_{int} we report for $CHCl_2$.

Vibrational excitation also accompanies curve crossing in CH_3I dissociation. The sudden change in the reaction coordinate in the crossing region promotes umbrella mode excitation in the CH_3 fragment. Studies of CH_3Br and CD_3Br found a similar exit-channel dependence.[8,22] For C_s-symmetry halomethanes, a greater number of excited states leading to ground-state halogen production outside of the crossing region are accessible. Studies of these halomethanes have invoked two distinct mechanisms to account for the greater spread of internal energy seen in the ground state channel: (1) direct dissociation from excited states correlating diabatically with ground-state products and (2) indirect dissociation *via* curve crossing from the $^3Q_{0^+}$ state. Although the topology of these potentials has not been determined with nearly the same detail as CH_3I, the second mechanism is qualitatively similar to CH_3I dissociation leading to ground-state I products, and therefore should promote rovibrational excitation in the molecular photofragment. Although we do not discern a clear bimodal distribution in our VMI data, the two-mechanism approach is consistent with the wider breadth of E_{int} we observe in the ground-state Br channel. The width of the $CHCl_2$ internal energy distribution as a fraction of the available energy decreases monotonically with increasing photolysis energy, and we cautiously regard this trend as evidence that curve crossing plays a larger role at lower photolysis energies.

3.4 Relative quantum yields

REMPI detection in conjunction with time-of-flight mass spectrometry (TOF-MS) discerns the relative quantum yield for the Br and Br* products as a function of photolysis wavelength. Three factors determine the TOF signal strength for a particular product state: (1) the

population of the product in the laser-interaction region, (2) the REMPI efficiency of the transition chosen to probe that product, and (3) laser power. To determine the relative quantum yield Φ of Br^*

$$\Phi(Br^*) = \frac{[Br^*]}{[Br] + [Br^*]} \tag{3.4}$$

we wish to measure the populations [Br] and [Br^*] in the laser-interaction region. Thus, factors (2) and (3) must be accounted for.

If the REMPI efficiencies of the transitions we utilize (Figure 3.2) to probe Br and Br^* were identical, the TOF signals we generate with a given laser power could be used directly as populations in Equation 3.4. In general, the REMPI efficiencies will differ, and we must derive a correction factor from a system that produces Br and Br^* with known relative yields using the same REMPI schemes. We chose CH_3Br photodissociation to accomplish this, relying on the yields reported by Gougousi, *et al.*[8] We prepare the sample by making a mixture of 10% CH_3Br in He from a lecture bottle and photolyze at 230 nm, where Gougousi, *et al.* report a relative yield for Br^* of 0.54. We record TOF signals with both lasers on, and with only the REMPI laser on. Subtracting the one-color REMPI signal from the two-color signal yields a difference signal due exclusively to fragments generated by the photolysis laser. We interface the oscilloscope with the computer and use Scope Explorer software (LeCroy) to capture the TOF traces.

To derive the correction factor from the CH_3Br data, we integrate the TOF traces with the Igor Pro software package. Since there are two isotopes of Br present in similar abundance (51% ^{79}Br and 49% ^{81}Br), we arbitrarily choose the ^{79}Br TOF peak for this integration. We determine the value of the quantum yield for the Br^* channel in the absence of a correction

factor, and divide the true value (0.54) by our value to arrive at a correction factor of 0.65 ± 0.06. Since this factor is due to the difference in efficiency between the two REMPI schemes we employ for Br and Br*, which is independent of the photolysis wavelength or the parent molecule, we can apply it to the Br TOF signals generated by $CHBrCl_2$ photodissociation at every photolysis wavelength we use. To ensure the laser power is consistent between the TOF traces we integrate, we take ten difference signals (five for each exit channel) alternating between Br and Br* successively. We do this at each wavelength on three separate days to ensure reproducibility and determine statistical uncertainty. We repeated measurements of the correction factor at other photolysis wavelengths (240 and 245 nm) reported by Gougousi, *et al* with less averaging and found they both agreed to within the uncertainty of the value we found at 230 nm. Figure 3.6 shows the TOF traces we used to obtain the correction factor.

The same protocol generates TOF traces for Br and Br* following $CHBrCl_2$ photolysis. We use Equation 3.4, scaled by the correction factor, to obtain the Br* yields. The Br yield is then $1 - \Phi(Br^*)$. Figure 3.7 shows the TOF traces we obtained at each wavelength, and Table 3.2 gives the relative quantum yields calculated from the integration of the TOF traces. Qualitatively, the branching between the two exit channels is split evenly at high photolysis energies, but at lower energy excitations the Br* yield declines. Nonetheless, Br* production extends to longer wavelengths, and we are able to see Br* signal as far out as 291 nm (although the signal was too faint to obtain quantitative yields). Section 3.5 will return to the VMI data to explore the origin of the relative quantum yields we measure.

Figure 3.6: TOF traces for Br and Br* following CH_3Br photodissociation at 230 nm. These are the traces we used to obtain a correction factor for the REMPI detection efficiencies in the $CHBrCl_2$ relative quantum yields.

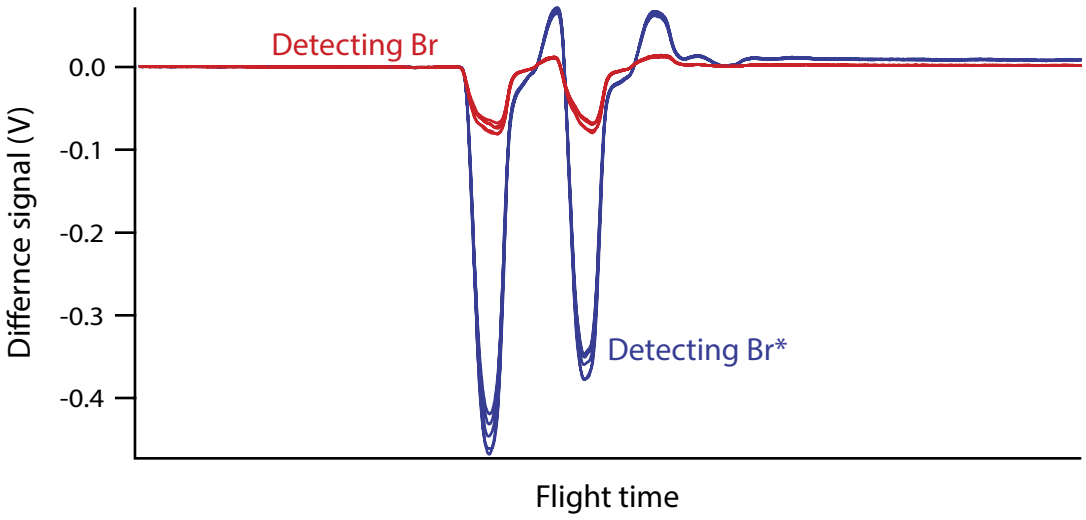
Detecting Br
Detecting Br*
0.0
-0.1
-0.2
-0.3
-0.4
Differnce signal (V)
Flight time

Figure 3.7: TOF traces for Br and Br* following $CHBrCl_2$ photodissociation at each photolysis wavelength we investigate.

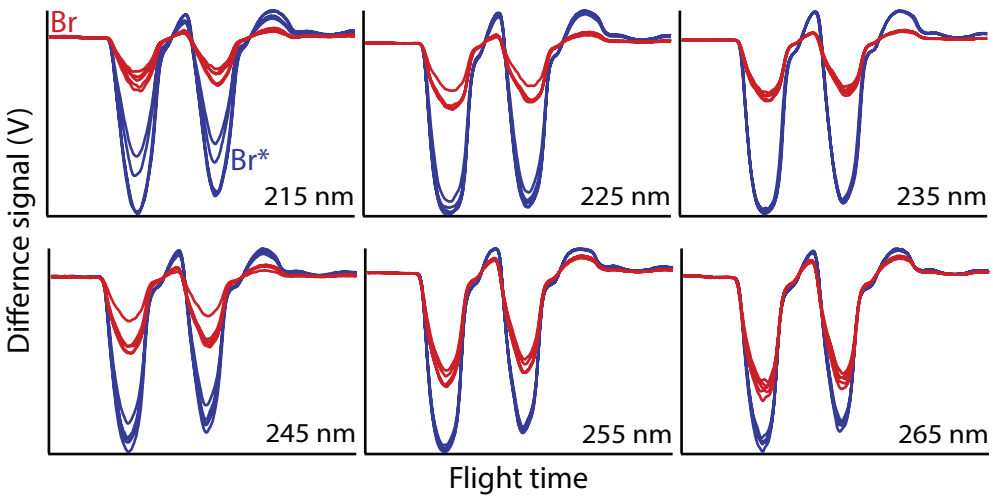
Br
Br*
215 nm
225 nm
235 nm
245 nm
255 nm
265 nm
Difference signal (V)
Flight time

Table 3.2: Relative quantum yields of Br and Br* following $CHBrCl_2$ photodissociation as a function of photolysis wavelength.

$\lambda_{\text{photolysis}}$ (nm)	Br state	Relative quantum yields
215	Br	0.50 ± 0.05
	Br*	0.50 ± 0.05
225	Br	0.52 ± 0.05
	Br*	0.48 ± 0.05
235	Br	0.51 ± 0.05
	Br*	0.49 ± 0.05
245	Br	0.55 ± 0.05
	Br*	0.45 ± 0.05
255	Br	0.60 ± 0.04
	Br*	0.40 ± 0.04
265	Br	0.62 ± 0.04
	Br*	0.38 ± 0.04

3.5 Anisotropy and partial absorption cross sections

The polarized electric field of the photolysis laser preferentially excites $CHBrCl_2$ parent molecules whose transition dipole moment is aligned with the field. Since the dissociation is characteristically quite rapid (much faster than a rotational period), this preferential directionality is preserved in the VMI measurements. If the transition dipole vector lies nominally parallel to the C−Br bond axis, fragments recoil up and down relative to the detector. If the transition dipole vector is perpendicular to the C−Br bond, fragments recoil left and right. Figure 3.8 shows the transition character of each excited state, that is, whether the transition dipole moment lies parallel ($\parallel$) or perpendicular ($\perp$) to the C−Br bond. Transition dipoles from the A' ground state to an A'' state in C_s symmetry molecules are oriented perpendicular to the mirror plane, and thus perpendicular to the C−Br bond in the case of $CHBrCl_2$.[23] Excited states of A' symmetry, on the other hand, have transition dipoles that lie in the mirror plane, and thus may be parallel or perpendicular to the C−Br bond axis. It is instructive to consider these excited states in the context of Figure 3.3. States that arise due to splitting of degenerate E states in C_{3v} symmetry have perpendicular character, consistent with anisotropy measurements for well-classified C_{3v} photodissociations. The only transition with parallel character is to the $^3Q_{0^+}$ state, which has A' symmetry in $CHBrCl_2$ and A_1 symmetry in C_{3v} analogues. We use this unique feature of the $^3Q_{0^+}$ state to infer details of the absorption and dynamics leading to the relative quantum yields we measure.

The anisotropy parameter β quantifies the degree to which the preferential directionality

Figure 3.8: Parallel and perpendicular transition character labels for the $CHBrCl_2$ $\tilde{A}$-band excited states. We show idealized transition dipole vectors (M_x, M_y, M_z) in green and the Br−C−H mirror plane in red.

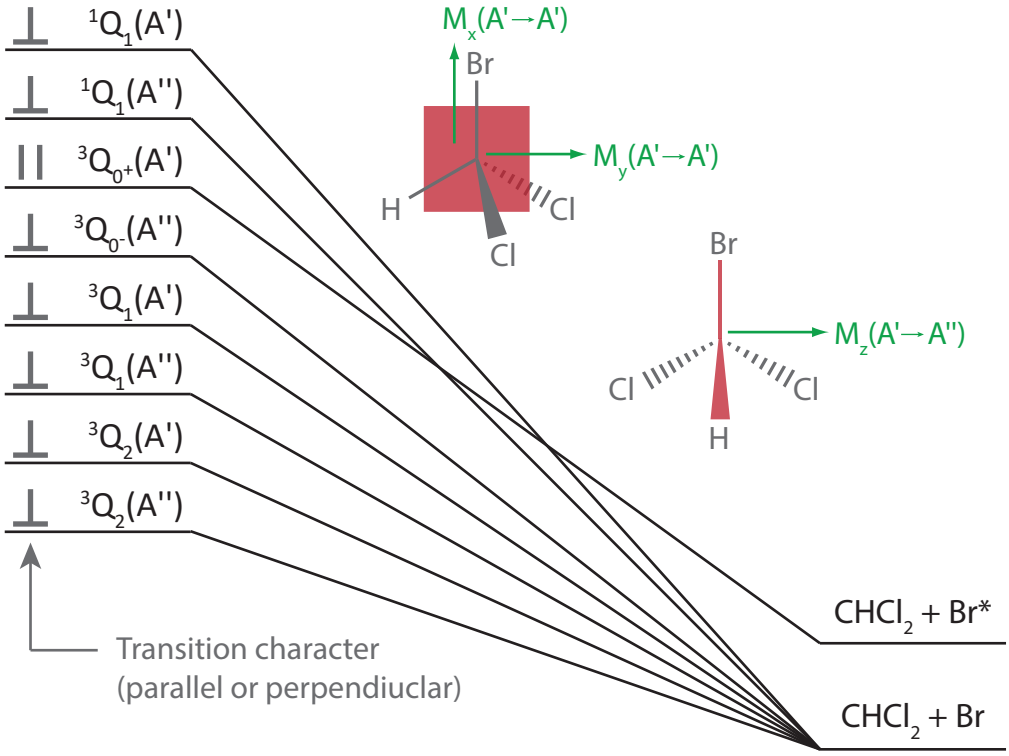
$^1Q_1(A')$
$^1Q_1(A'')$
$^3Q_{0^+}(A')$
$^3Q_{0^-}(A'')$
$^3Q_1(A')$
$^3Q_1(A'')$
$^3Q_2(A')$
$^3Q_2(A'')$
Transition character
(parallel or perpendiuclar)
$M_x(A' \rightarrow A')$
Br
$M_y(A' \rightarrow A')$
H
Cl
Cl
Br
$M_z(A' \rightarrow A'')$
Cl
Cl
H
$CHCl_2 + Br^*$
$CHCl_2 + Br$

of the recoiling photofragments is preserved in the VMI measurements. We obtain β by fitting angular distributions of the photofragments generated by BASEX at a given image radius to

$$I(\theta) \propto 1 + \beta P_2(\cos\theta) \tag{3.5}$$

where I is the signal intensity at angle θ away from the laser polarization vector and P_2 is the second Legendre polynomial. There are two limiting cases for the anisotropy parameter: $\beta \to -1$ for a single transition of perpendicular character, and $\beta \to 2$ for a single transition of perpendicular character. In reality, the transition dipole vectors will only be perfectly parallel or perpendicular to bond cleavage for a diatomic dissociation, so the vectors depicted in Figure 3.8 are somewhat idealized. Moreover, a measurement of β may contain contributions from a number of excited states of perpendicular or parallel character, particularly for a molecule like $CHBrCl_2$ in which all transitions in the $\tilde{A}$-band are spin- and dipole-allowed. Thus, we cannot expect our measurements of β to reach the limiting cases, but given that only one parallel transition is present in the $CHBrCl_2$ $\tilde{A}$-band, we can attribute trends towards positive β with excitation to the $^3Q_{0^+}$ state.

Figure 3.9 shows angular distributions at the peak of E_{trans} for both exit channels at each photolysis wavelength. We fit each distribution to Equation 3.5 to extract β. Figure 3.10 shows representative images from which we extract the angular distributions, as well as a plot of β as a function of photolysis wavelength, the the relative quantum yield of the two exit channels, and the total absorption cross section for $CHBrCl_2$ measured by Orlando and coworkers.[13] We explicate details of the $CHBrCl_2$ photodissociation process using the correspondence between these seemingly independent measurements.

Figure 3.9: Angular distributions of VMI intensity generated at the peak of the E_{trans} distribution. We fit each distribution to Equation 3.5 to extract the anisotropy parameter β.

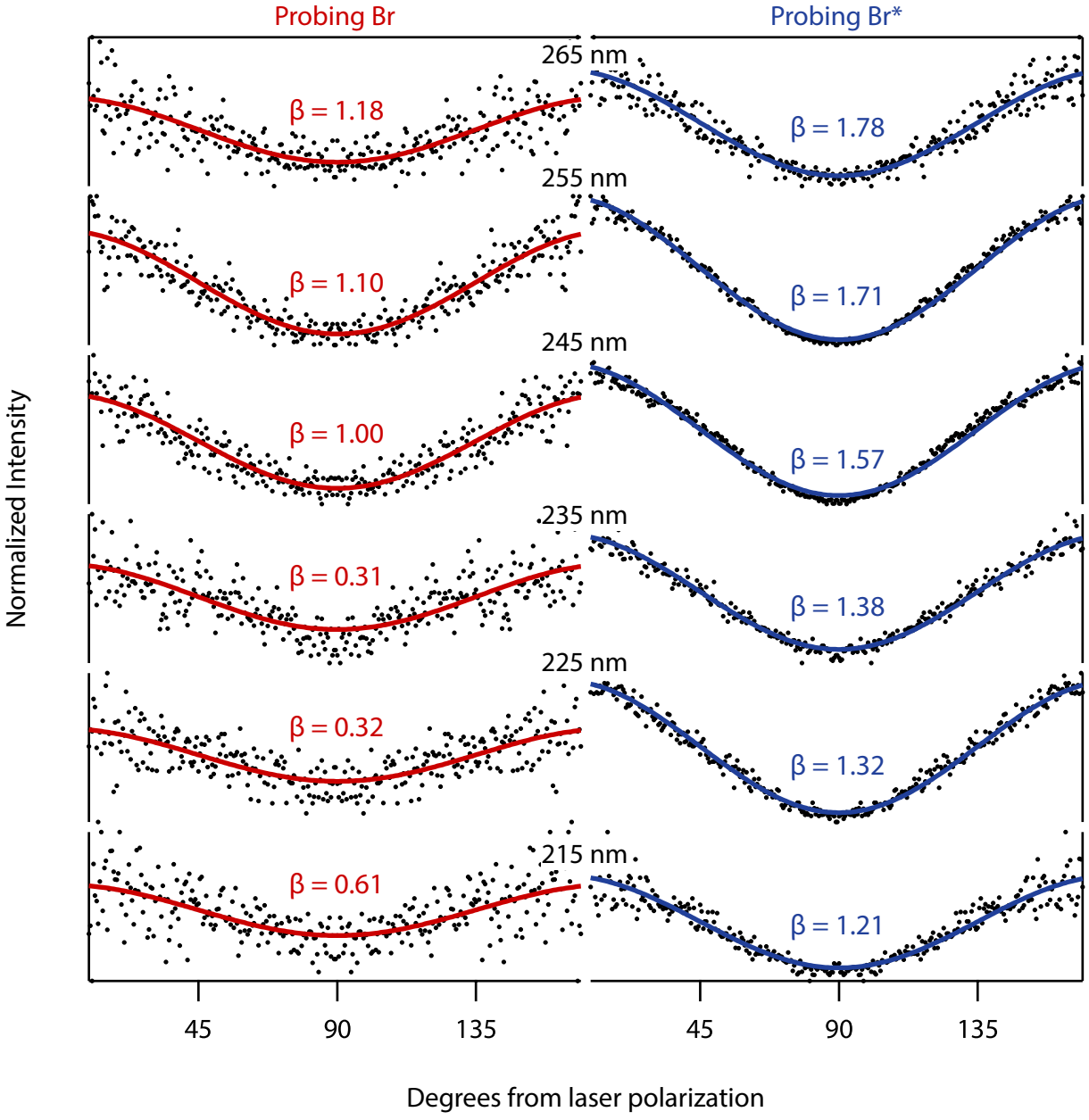
Probing Br
Probing Br*
265 nm
β = 1.18
β = 1.78
255 nm
β = 1.10
β = 1.71
245 nm
β = 1.00
β = 1.57
235 nm
β = 0.31
β = 1.38
225 nm
β = 0.32
β = 1.32
215 nm
β = 0.61
β = 1.21
45
90
135
45
90
135
Normalized Intensity
Degrees from laser polarization

Figure 3.10: (a) Reconstructed images at short (215 nm), intermediate (235 nm), and long (255 nm) photolysis wavelengths for both product channels. Trends as a function of photolysis wavelengths for (b) the anisotropy parameter determined in dissociations leading to Br^* (closed circles, blue) and Br (open circles, red) and (c) the Br^* yield (open circles, black) and the $CHBrCl_2$ absorption cross-section (broken line, green). The absorption cross section data is reproduced with permission from Orlando and coworkers.[13]

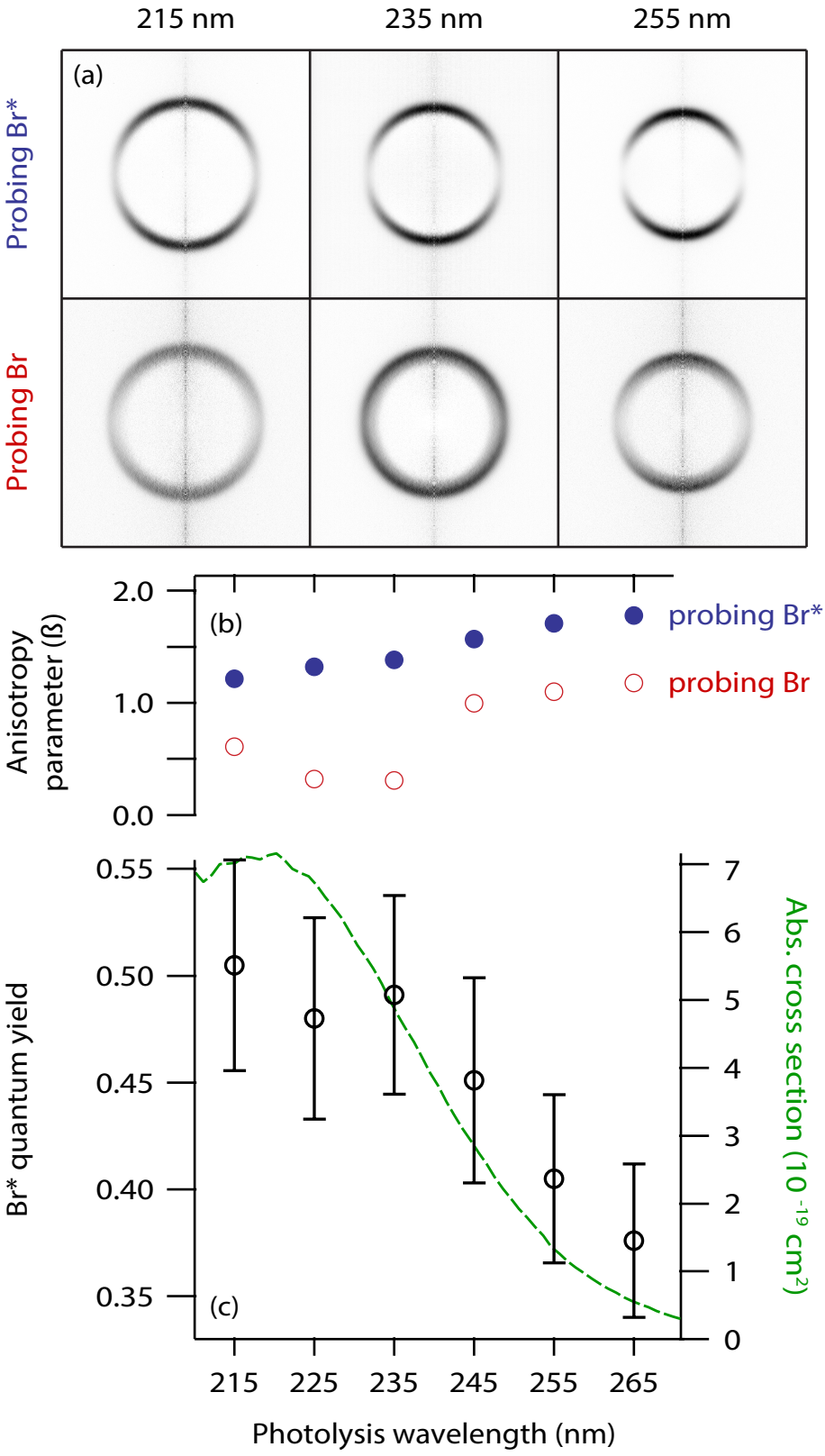
215 nm
235 nm
255 nm
(a)
Probing Br*
Probing Br
(b)
Anisotropy parameter (ß)
2.0
1.0
0.0
probing Br*
probing Br
(c)
Br* quantum yield
0.55
0.50
0.45
0.40
0.35
Abs. cross section (10 -19 cm2)
7
6
5
4
3
2
1
0
215
225
235
245
255
265
Photolysis wavelength (nm)

We begin unpacking Figure 3.10 by considering the Br* exit channel. The anisotropy parameter for this channel increases at longer photolysis wavelengths, indicating a growing prevalence of parallel transitions. Trajectories leading to Br* originate exclusively from perpendicular transitions to the $^1Q_1(A')$ and parallel transitions to the $^3Q_{0^+}(A')$ state, so the former appears to have strongest absorption at higher photolysis energies. Additionally, β is more positive at every photolysis energy for the Br* channel than the Br channel, so the $^3Q_{0^+}(A')$ state, with its parallel transition character, must play a bigger role in absorption generating Br* products. Nonetheless, both exit channels exhibit positive β values at every photolysis wavelength we investigated, indicating at least some contribution from transitions to $^3Q_{0^+}(A')$ are present and lead to both product states throughout the Ã-band.

Although excitation to $^3Q_{0^+}(A')$ dominates the production of Br* at longer photolysis wavelengths, we see the relative quantum yield of Br* decline in this region. There are two reasonable explanations for this behavior: (1) trajectories originating on the $^3Q_{0^+}(A')$ PES are more prone to adiabatic passage through the crossing region, producing Br or (2) direct excitation to the lower-lying excited states ($^3Q_2$,$^3Q_1$, and $^3Q_{0^-}$), which lead to Br production below the crossing region, competes with $^3Q_{0^+}(A')$ excitation. The anisotropy data for the ground-state exit channel suggest that the former explanation is more likely. As the relative quantum yield for Br* drops, β increases in *both* exit channels. If the yield was hampered by competition with the lower-lying excited states, transitions producing Br should be increasingly perpendicular and β should decline. Thus, at longer photolysis wavelengths, the relative quantum yield of Br and Br* is dictated largely by the dynamics in the crossing region.

At intermediate photolysis energies, β declines for the ground-state exit channel, while

the Br yields are essentially constant. We tentatively attribute this decrease in β at 225 and 235 nm to contributions from perpendicular transitions that are not subject to the crossing region. Despite competition from excited states outside of the crossing region, the relative quantum yield at these intermediate photolysis energies is unaffected. Thus, a tradeoff occurs in which trajectories from the $^3Q_{0^+}(A')$ state proceed through the crossing region in a less adiabatic manner (generating Br*) while trajectories from other excited states generate Br directly with similar efficiency. As the partial absorption cross sections for these other excited states diminish, curve crossing from the $^3Q_{0^+}(A')$ begins to dictate the Br* yield. Unfortunately, with the exception of transitions to the $^1Q_1(A')$ state leading to Br* products, our analysis of the data has no way of deconvolving the individual contributions from the many possible perpendicular transitions.

Figure 3.11 provides a qualitative rendering of partial absorption cross-sections consistent with our explanation of the anisotropy and branching data. We label the two transitions that produce Br* in this cartoon, but we cannot assign the remainder of the transitions, which all have perpendicular character. Calculations that include spin–orbit interaction to determine oscillator strengths of the lower-lying excited states in $CHBrCl_2$ as a function of excitation energy would be valuable in understanding their individual contributions to the absorption cross-section. We note that the waning total absorption cross-section of $CHBrCl_2$ at longer wavelengths tracks the decline of relative Br* quantum yield, and the data we took at 291 nm photolysis confirm this trend. Difference signals were small at 291 nm, but we estimate a Br* yield of ~ 0.3, which implies that absorption to the $^3Q_{0^+}(\mathrm{A}')$ state extents into the low-energy regime of the $CHBrCl_2$ $\tilde{\mathrm{A}}$-band, as shown in Figure 3.11.

Figure 3.11: Cartoon rendering of potential partial absorption cross-sections for transitions to the ${}^3Q_{0^+}(\mathrm{A}')$ (blue) and ${}^1Q_1(\mathrm{A}')$ (red) states. Potential contributions from all other perpendicular transitions are shown in gray. The total absorption cross-section (black) is reproduced with permission from Orlando and coworkers.[13]

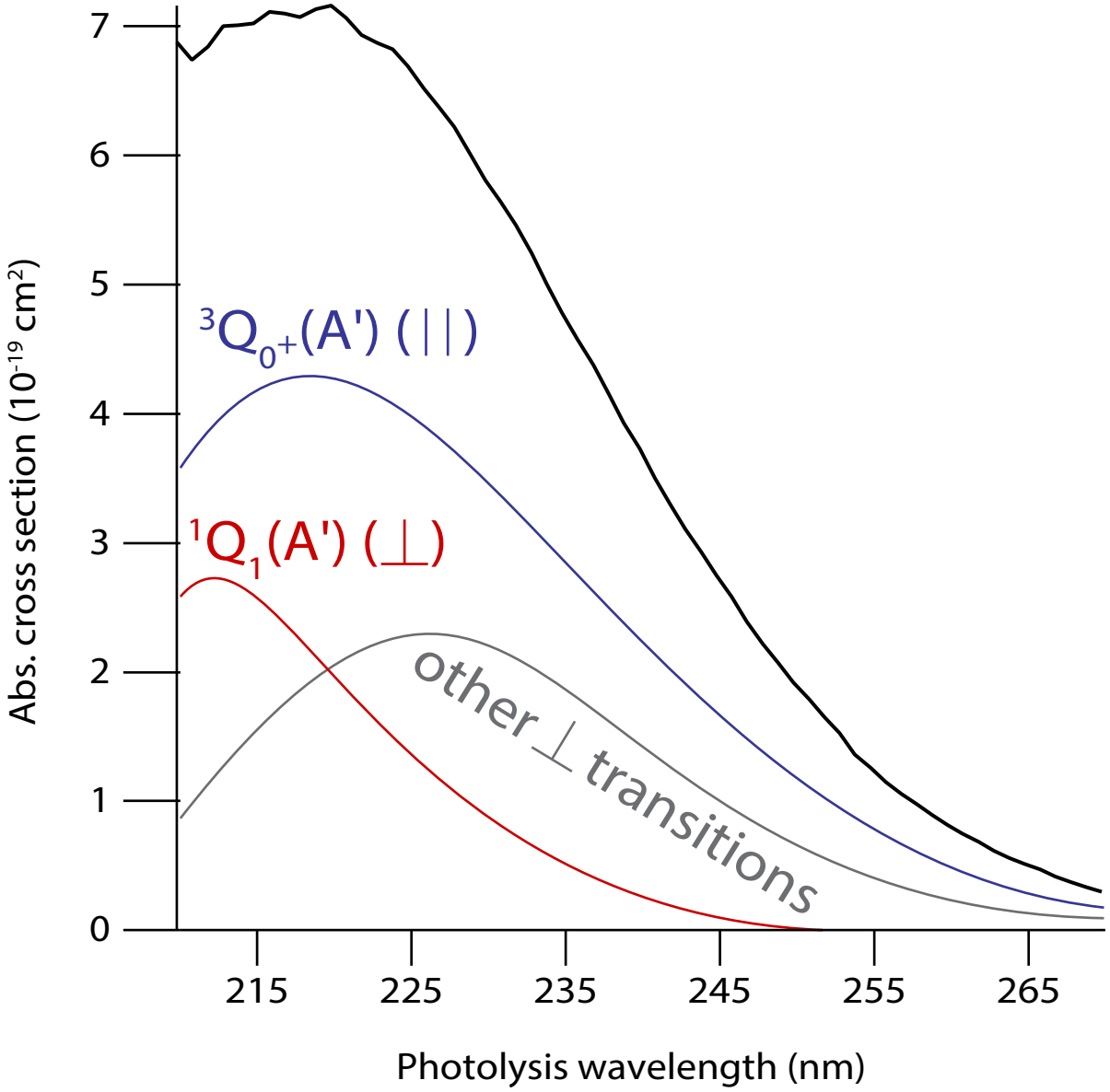
7
6
5
4
3
2
1
0
Abs. cross section (10^{-19} cm^2)
$^3Q_{0^+}$(A') (||)
$^1Q_1$(A') (⊥)
other ⊥ transitions
215
225
235
245
255
265
Photolysis wavelength (nm)

3.6 Impulsive modeling and comparison with similar systems

We wish to consider the partitioning of E_{int} between vibrational and rotational energy in the $CHCl_2$ fragment. In lieu of structural features in the VMI data, we turn to classical impulsive models and findings from studies on similar halomethane photodissociations. Impulsive models treat atoms as noninteracting, and the repulsive force acts entirely and instantaneously along the bond-breaking axis in the equilibrium geometry of the parent molecule. Conservation of energy and momentum then dictate energy partitioning between the photofragments.[24]

3.6.1 Wilson model

Wilson and coworkers developed an early version of the impulsive model to interpret rotational state distributions in dissociations of triatomic molecules.[25,26] Figure 3.12 depicts $CHBrCl_2$ simplified as a triatomic CBrY, where Y is the center-of-mass for the H and Cl atoms. The repulsion between the C and Br atoms generates torque about the C−Y center-of-mass, reducing the Br−C−Y angle θ. In the original conception of the model, the so-called "soft limit," the initial impulse of the dissociation imparts momentum only to the C and Br atoms undergoing bond cleavage and the remaining atoms are frozen. The C atom then "collides" with the rest of the molecular fragment where translational energy is lost somewhat to internal excitation. In the soft limit, the C and Br atoms initially recoil with translational

Figure 3.12: Schematic of impulsive model treatment for $CHBrCl_2$ dissociation. Y is the center of mass of the H and Cl atoms, θ is the angle formed by Br, C, and Y, and j is the rotational angular momentum. Repulsion (red) between Br and C generates torque (blue) about the C−Y center of mass.

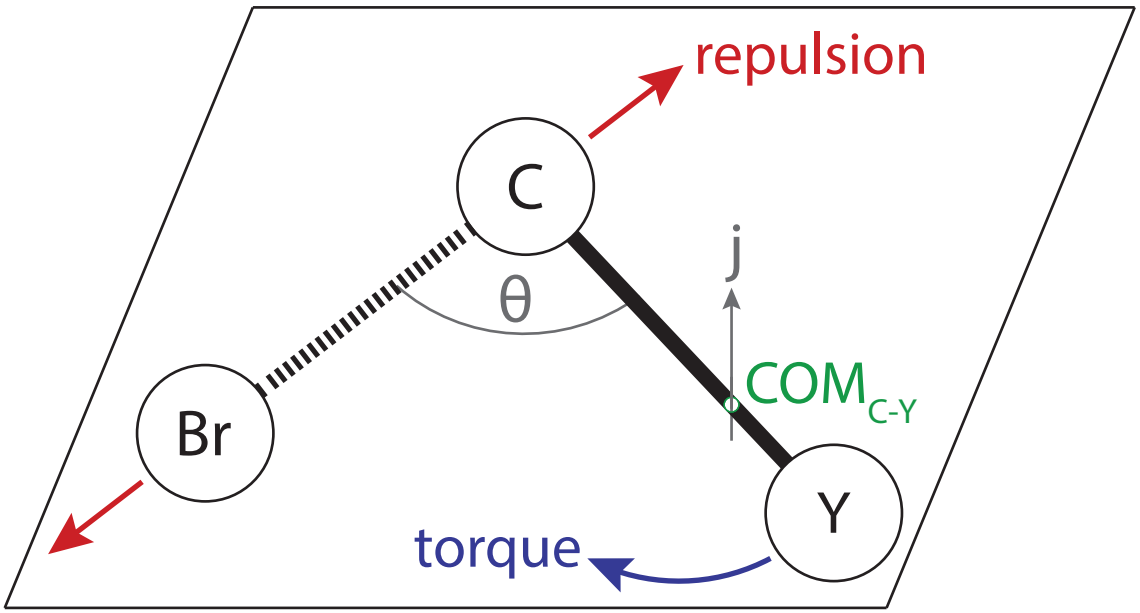
repulsion
C
θ
j
COM C-Y
Br
Y
torque

energy equal to E_{avl}. In other words,

$$E_{avl} = \frac{1}{2}\left(\frac{p_{\mathrm{C}}^2}{m_{\mathrm{C}}} + \frac{p_{\mathrm{Br}}^2}{m_{\mathrm{Br}}}\right) \tag{3.6}$$

where p_{C} and p_{Br} are the magnitudes of the momenta initially imparted to the C and Br atoms, respectively, and m_{C} and m_{Br} are their masses. After some portion of the translational energy in the C atom is transferred to internal excitation of CY, the total remaining translational energy is given by

$$E_{trans} = \frac{1}{2}\left(\frac{p_{\mathrm{CY}}^2}{m_{\mathrm{CY}}} + \frac{p_{\mathrm{Br}}^2}{m_{\mathrm{Br}}}\right) \tag{3.7}$$

where P_{CY} and m_{CY} are the momentum and mass of the CY fragment, respectively. Conservation of momentum dictates that $p_{\mathrm{Br}} = p_{\mathrm{C}} = p_{\mathrm{CY}}$. Thus,

$$\begin{aligned}
\frac{E_{trans}}{E_{avl}} &= \left(\frac{p_{\mathrm{CY}}^2}{m_{\mathrm{CY}}} + \frac{p_{\mathrm{Br}}^2}{m_{\mathrm{Br}}}\right)\left(\frac{p_{\mathrm{C}}^2}{m_{\mathrm{C}}} + \frac{p_{\mathrm{Br}}^2}{m_{\mathrm{Br}}}\right)^{-1} \\
&= \left(\frac{m_{\mathrm{C}} m_{\mathrm{Br}}}{m_{\mathrm{CY}} m_{\mathrm{Br}}}\right)\left(\frac{m_{\mathrm{Br}} p_{\mathrm{CY}}^2 + m_{\mathrm{CY}} p_{\mathrm{Br}}^2}{m_{\mathrm{Br}} p_{\mathrm{C}}^2 + m_{\mathrm{C}} p_{\mathrm{Br}}^2}\right) \\
&= \left(\frac{m_{\mathrm{C}} m_{\mathrm{Br}}}{m_{\mathrm{C}} + m_{\mathrm{Br}}}\right)\left(\frac{m_{\mathrm{CY}} + m_{\mathrm{Br}}}{m_{\mathrm{CY}} m_{\mathrm{Br}}}\right) \\
&= \frac{\mu_a}{\mu_f}
\end{aligned} \tag{3.8}$$

where μ_a is the reduced mass for the atoms constituting the cleaved bond and μ_f is the reduced mass for the two photofragments, respectively. We apply Equation 3.8 to our results for $CHBrCl_2$ and to a number of other photodissociation studies on low-symmetry halomethanes similar to $CHBrCl_2$, namely: CH_2I_2,[27] ICH_2Cl,[28,29] CH_2ClBr,[16,30–33] and CH_3CH_2I.[34,35] Figure 3.13 (top) shows the translational energy partitioning for these photodissociations. The horizontal axis is the result of the soft limit for the Wilson impulsive model. The vertical axis is the measured translational energy disposal. Equation 3.8 indicates that translational

Figure 3.13: Top: comparison of measured and modeled fractional energy partitioning for $CHBrCl_2$ photodissociation with similar alkyl halides: CH_3CH_2I,[34,35] (purple), CH_2ClBr[16,30–33] (blue), ICH_2Cl[28,29] (green), $CHCl_2Br$ (this work, orange), and CH_2I_2[27] (red). Experimental data taken at various photolysis energies is averaged and shown as one point, and we use a soft impulsive model[25] for comparison. Open markers denote dissociations leading to spin-excited halogen fragments, and closed markers denote ground-state halogen fragments. In the case of CH_2I_2, Xu et al. were able to distinguish between ground-state I atoms formed directly (square marker) and indirectly via curve-crossing (triangle marker). Bottom: data used for averaging in the top figure. The hash marks on the right-hand axis denote the value calculated with the soft impulsive model.

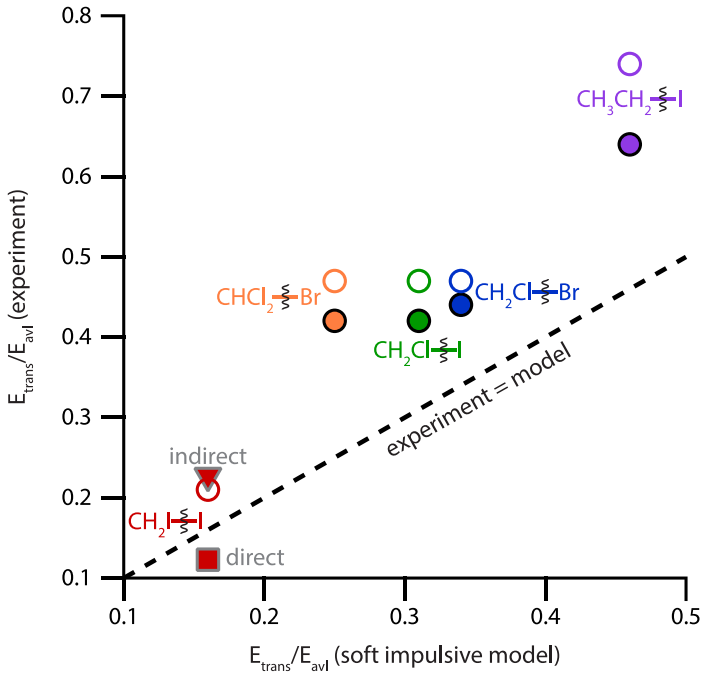
0.8
0.7
0.6
0.5
0.4
0.3
0.2
0.1
E_{trans}/E_{avl} (experiment)
CH_3CH_2–I
$CHCl_2$–Br
CH_2Cl–Br
CH_2Cl–I
experiment = model
indirect
CH_2I–I
direct
0.1
0.2
0.3
0.4
0.5
E_{trans}/E_{avl} (soft impulsive model)

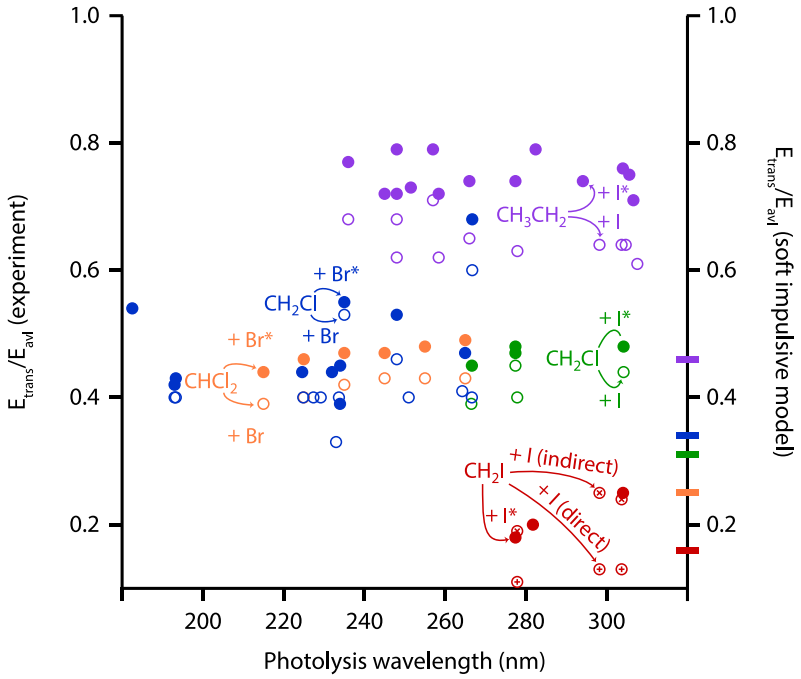
1.0
0.8
0.6
0.4
0.2
E_{trans}/E_{avl} (experiment)
CH_3CH_2
+ I*
+ I
+ Br*
CH_2Cl
+ Br
$CHCl_2$
CH_2I
+ I (indirect)
+ I (direct)
200
220
240
260
280
300
Photolysis wavelength (nm)
E_{trans}/E_{avl} (soft impulsive model)

energy should scale linearly with available energy, and thus that fractional energy partitioning should be constant. The bottom portion of Figure 3.13 confirms this notion by plotting the translational energy disposal in each study as a function of photlysis wavelength. We therefore average the fractional energy partitioning over all of the photolysis wavelengths employed by the various studies depicted in the top portion of Figure 3.13. Qualitatively, the figure confirms the trend predicted by the impulsive model that lighter fragments recoil from photodissociation with more translational energy than heavier fragments. However, the model consistently underestimates the measured translational energy (and thus overestimates the internal energy of molecular photofragment). We proceed by utilizing a more sophisticated version of the classical impulsive model that incorporates our measurement of E_{trans} and assess whether this brings our measurements into better agreement.

3.6.2 Butler model

Butler and coworkers have developed an improvement to the impulsive model that utilizes measured translational energy to predict vibrational and rotational excitation in the molecular photofragment.[36] The model foregoes pseudo-triatomic simplification used in the Wilson model in favor of a 3-D inertia tensor, and calculates the rotational energy imparted to the molecular photofragment with the angular momentum vector. We coded the model in MATLAB from scratch in a way that is general enough to easily apply it to any parent molecule undergoing photodissociation provided the geometry is known and the kinetic energy of the recoiling photofragments is measured. Figure 3.14 shows the body of the code `butler_model.m`. Appendix A shows and describes the individual subroutines the code im-

Figure 3.14: MATLAB code for the impulsive model developed by Butler and coworkers.[36] Comments describing each subroutine are in green. The individual subroutines are detailed in Appendix A.

```
function Erot = butler_model(input_matrix,C,X,TKER)

mass = input_matrix(1,:);           % extract top row of input matrix to
                                    % get masses

mass_SI = mass/6.0221409e23/1000;   % put masses in kg

cart_coord = input_matrix(2:4,:);   % extract bottom three rows of input
                                    % matrix to get cartesian coordinates

cart_coord_SI = cart_coord/(10^10); % put coordinates in m

cart = zero_cart(cart_coord_SI,C);  % translate molecule to put carbon atom
                                    % at origin

sph = makesph(cart);                % switch to spherical coordinate system

rot = rot_bond(sph,X);              % rotate molecule to put C-X bond along
                                    % y-axis

newcart = makecart(rot);            % switch back to cartesian coordinates

com = comfind(newcart,mass_SI,X);   % find center of mass for molecular
                                    % fragment

comframe = comtrans(newcart,com);   % translate molecule to put molecular
                                    % fragment COM at origin

tensor = itensor(comframe,mass_SI,X); % calculate inertia tensor in center
                                      % of mass frame

relv = findrelv(TKER,mass_SI,X);    % find relative velocity of the
                                    % recoiling photofragments from TKER
                                    % and conservation of momentum

J = findj(relv,comframe,mass_SI,X); % calculate angular momentum vector

Erot_joules = 1/2*transpose(J)*(tensor^-1)*J; % calculate Erot

Erot = Erot_joules/(1.9863e-23); % convert Erot to wavenumbers
```

plements. For a parent molecule with N atoms, the variable `input_matrix` is a 3 by N matrix. The top row contains the mass of each atom in atomic units and corresponding coordinates of each atom in Å appear in the bottom three rows beneath their respective mass. The variables `C` and `X` are the columns of `input_matrix` containing the mass and coordinates for the carbon and halogen atoms constituting the cleaved bond, respectively. The variable `TKER` is the measured total kinetic energy release. The calculations we perform with this code use E_{trans}^{mp} for `TKER`. The angular momentum vector $\vec{J}$ is given by

$$\vec{J} = \vec{r} \times \mu \vec{v}_{rel} \tag{3.9}$$

where $\vec{r}$ is the position vector between the center of mass of the molecular radical moiety and the atomic moiety in the parent geometry, $\vec{v_{rel}}$ is their measured relative recoil velocity, and μ is their reduced mass. The rotational energy E_{rot} imparted to the molecular photofragment is then

$$E_{rot} = \frac{1}{2} \vec{J}^T I^{-1} \vec{J} \tag{3.10}$$

where $\vec{J}^T$ is the transpose of the angular momentum vector. The remaining internal energy goes into vibrational degrees of freedom.

We optimize the $CHBrCl_2$ geometry with the Gaussian 09 Program using the B3LYP density functional and the aug-cc-pVTZ basis set. The `input_matrix` variable for the `butler_model.m` code containing the results of this optimization is

$$\begin{bmatrix} 12.0 & 1.01 & 35.4 & 34.5 & 79.9 \\ 0.00000000 & 0.90340200 & 0.00000000 & 0.00000000 & -1.48869400 \\ 0.00000000 & 0.59060400 & -1.00026400 & -1.00026400 & 1.26896000 \\ 0.00000000 & 0.00000000 & 1.46858200 & -1.46858200 & 0.00000000 \end{bmatrix}$$

where the columns from left to right contain the masses and coordinates for the C, H, Cl, Cl, and Br atoms, respectively. Figure 3.15 shows the results of the Butler model using this geometry. Clearly, the model does not allot a realistic amount of energy to vibrational excitation. The vibrational energy predicted the $CHCl_2$ fragment is nonphysical (negative) in many cases and very slight at higher photolysis energies. We conclude that the Butler impulsive model, while strictly more accurate than the Wilson impulsive model, over predicts rotational excitation for the molecular fragment following $CHBrCl_2$ photodissociation.

To further verify the overestimation of rotational energy by the Butler model, we turn to the experimental results of Cheng *et al.*, who were able to resolve rovibrational structure for the CH_2Cl fragment following ICH_2Cl photodissociation at 304.02 and 277.38 nm.[29] The optimized geometry for the ICH_2Cl parent is taken from the NIST Web Book, which uses B3LYP/6-31G(d) for the C, H, and Cl atoms and an SSD pseudopotential for the I atom. Figure 3.16 demonstrates a systematic over prediction of E_{rot} using this geometry and the Butler model. We plot the measured and modeled rotational energy as a function of the measured translational energy reported by Cheng *et al.* and see the model overestimates rotational energy disposal by thousands of wavenumbers at every measurement.

3.6.3 Impulsive model assessment

Both impulsive models overestimate internal energy partitioning following photodissociations of low-symmetry halomethanes. Important features of the photodissociation process are evidently missing from the classical impulsive description, but their conspicuous limiting assumptions provide some insight about the nature of the photodissociation dynamics. In

Figure 3.15: Results for energy disposal following $CHBrCl_2$ photodissociation as predicted by the impulsive model developed by Butler and coworkers.[36] The model uses the translational energy we measure (red) to calculate the angular momentum imparted to the $CHCl_2$ photofragment. Then, with a three-dimensional inertia tensor for the fragment, the model determines the rotational energy of $CHCl_2$ (blue). The remaining available energy is vibrational (green). We show the results for the Br channel as solid circles and the Br^* channel as empty triangles.

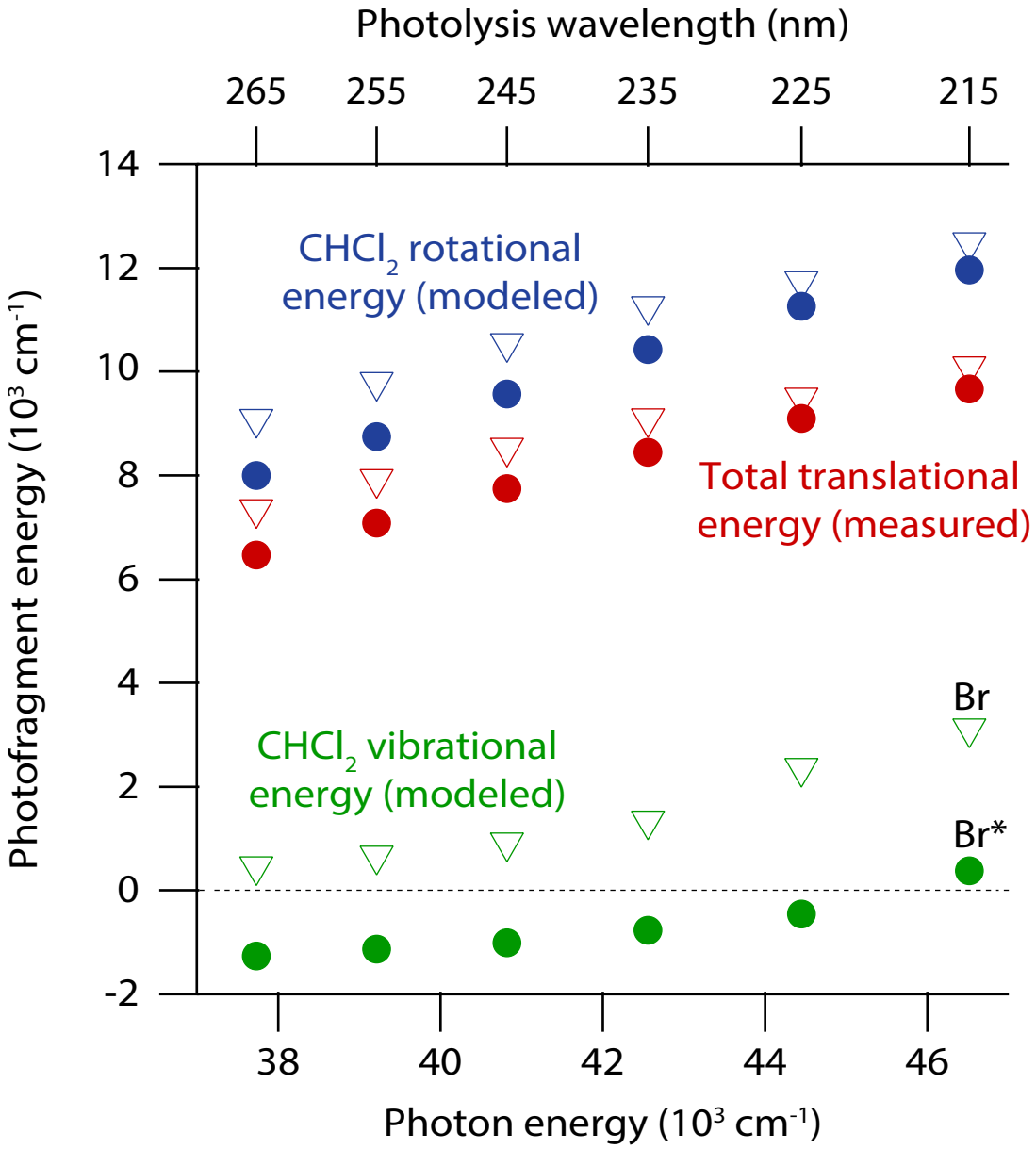
Photolysis wavelength (nm)
265
255
245
235
225
215
14
12
10
8
6
4
2
0
-2
Photofragment energy (10³ cm⁻¹)
CHCl₂ rotational energy (modeled)
Total translational energy (measured)
CHCl₂ vibrational energy (modeled)
Br
Br*
38
40
42
44
46
Photon energy (10³ cm⁻¹)

Figure 3.16: Comparison of measured (red) and modeled (blue) rotational energy partitioning for ICH_2Cl photodissociation. The measured and modeled values for E_{rot} are plotted against the measured translational energy. Modeling was done using the Butler impulsive model,[36] and measurements were taken by Cheng and coworkers.[29]

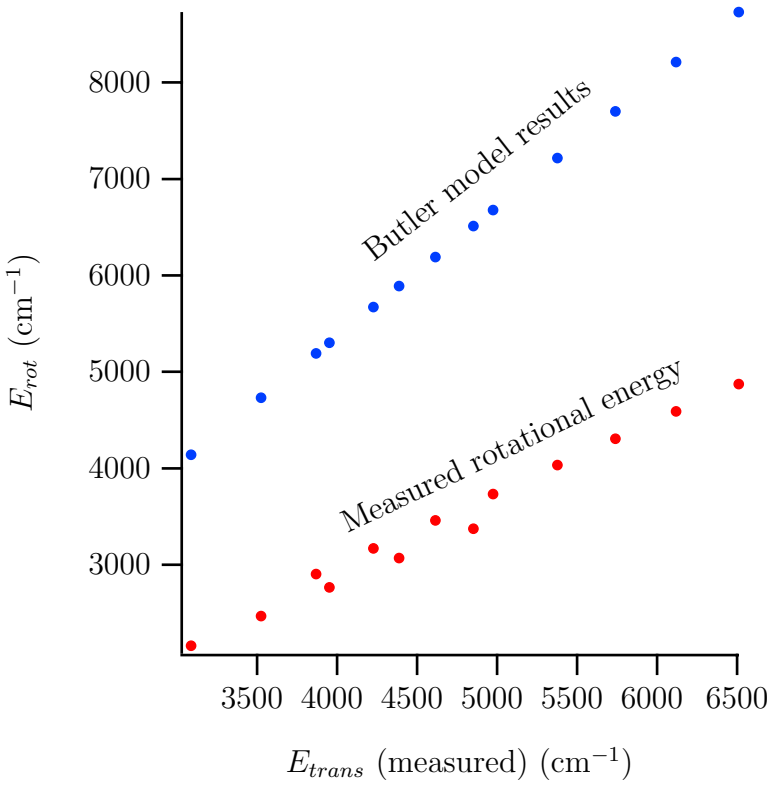
8000
7000
6000
5000
4000
3000
E_{rot} (cm^{-1})
Butler model results
Measured rotational energy
3500
4000
4500
5000
5500
6000
6500
E_{trans} (measured) (cm^{-1})

di- or tri-substituted halomethanes, the torque generated by the impulse demonstrated in Figure 3.12 brings the halogen atoms closer together at short times. Repulsion between the halogen atoms should oppose this torque and hampers rotational excitation, but atoms in the classical impulsive model are treated as non-interacting. Their interaction is borne out in the angular dependence of the PES, so attention to this aspect of trajectory calculations for di- or tri-substituted halomethanes is likely to be crucial to their accuracy. Additionally, during the course of photodissociation, the nominally trigonal pyramidal $CHCl_2$ moiety in the parent molecule evolves to the trigonal planar structure in the isolated $CHCl_2$ fragment at equilibrium. This motion should promote bending and umbrella excitations in the products, which allots less energy for rotation.

3.7 Summary

We have investigated the dynamics and relative quantum yields for $CHBrCl_2$ photodissociation between 215 and 265 nm using TOF-MS and VMI techniques. State-selective product detection using REMPI allows for exit-channel specific analysis of energy partitioning, and impulsive models and comparison to similar systems lends insight to the partitioning we cannot resolve experimentally. Anisotropy present in the VMI measurements allows us to distinguish somewhat between the many excited electronic states in the $CHBrCl_2$ $\tilde{A}$-band. Fractional energy partitioning throughout the range of photolysis energies we study is essentially constant, which is consistent with an impulsive dissociation. However, classical impulsive dissociation models fail to capture the partitioning between rotational and vibrational energy in the molecular photofragment accurately. Full dimensional trajectory

calculations that account for spin-orbit coupling and accurately capture the angular dependence of the PES would be valuable in further explaining the dynamics leading to the exit channel branching and energy disposal we measure.

The photodissociation dynamics of $CHBrCl_2$ are demonstrably more complex than the more widely studied C_{3v} halomethanes, but those studies inform our analysis in a number of ways, particularly for examining the role of curve crossing in the dynamics and exit channel branching. Transitions to low-lying excited states that are forbidden in C_{3v} geometries are important, and rotational excitation in the molecular photofragment is kinematically distinct from C_{3v} dissociations. Although we do not directly measure this rotational excitation, we do observe internally excited $CHCl_2$ photofragments, and comparison with other studies affirms the distinct dynamics associated with C_s symmetry halomethane dissociations.

References

[1] M. D. Barry and P. A. Gorry. Photofragmentation dynamics of CH_3I at 248 nm. *Mol. Phys.*, 52(2):461–473, 1984.

[2] S. M. Penn, C. C. Hayden, K. J. Carlson Muyskens, and F. F. Crim. The photodissociation of methyl iodide at 229.4 nm: A determination of the fragment recoil anisotropy using energy-selective electron impact ionization and time-of-flight mass spectrometry. *J. Chem. Phys.*, 89(5):2909–2917, 1988.

[3] M. D. Person, P. W. Kash, and L. J. Butler. The influence of parent bending motion on branching at a conical intersection in the photodissociation of cx3i (x=h,d,f). *J. Chem. Phys.*, 94(4):2557–2563, 1991.

[4] T. Ibuki, A. Hiraya, and K. Shobatake. Vacuum ultraviolet absorption spectra and photodissociative excitation of $CHBr_2Cl$ and $CHBrCl_2$. *J. Chem. Phys.*, 96(12):8793–8798, 1992.

[5] R. A. Hertz and J. A. Syage. Detection of the perpendicular ã state transitions of CH_3I by imaging of photofragment angle-velocity distributions. *J. Chem. Phys.*, 100(12):9265–9268, 1994.

[6] A. Furlan, T. Gejo, and J. R. Huber. Probing curve crossing by wavelength-dependent recoil anisotropy: The photodissociation of CF_3I at 275-303 nm studied by photofragment translational spectroscopy. *J. Phys. Chem.*, 100(19):7956–7961, 1996.

[7] H. Ohoyama, T. Ogawa, H. Makita, T. Kasai, and K. Kuwata. A direct determination of the direction for the transition dipole moment by the polarized laser photolysis of the oriented CH_3I beam. *J. Phys. Chem.*, 100(12):4729–4733, 1996.

[8] T. Gougousi, P. C. Samartzis, and T. N. Kitsopoulos. Photodissociation study of CH_3Br in the first continuum. *J. Chem. Phys.*, 108(14):5742–5746, 1998.

[9] A. T. J. B. Eppink and D. H. Parker. Methyl iodide ã-band decomposition study by photofragment velocity imaging. *J. Chem. Phys.*, 109(12):4758–4767, 1998.

[10] A. T. J. B. Eppink and D. H. Parker. Energy partitioning following photodissociation of methyl iodide in the a band: A velocity mapping study. *J. Chem. Phys.*, 110(2):832–844, 1999.

[11] Y. Amatatsu, S. Yabushita, and K. Morokuma. Full nine-dimensional *ab initio* potential energy surfaces and trajectory studies of ã-band photodissociation dynamics: $CH_3I\cdot \rightarrow CH_3{}^+I$, $CH_3{}^+I\cdot$, and $CD_3I\cdot \rightarrow CD_3{}^+I$, $CD_3{}^+I\cdot$. *J. Chem. Phys.*, 104(24):9783–9794, 1996.

[12] W. G. Merrill, F. F. Crim, and A. S. Case. Dynamics and yields for $CHBrCl_2$ photodissociation from 215-265 nm. *Phys. Chem. Chem. Phys.*, 18:32999–33008, 2016.

[13] M. Bilde, T. J. Wallington, C. Ferronato, J. J. Orlando, G. S. Tyndall, E. Estupiñan, and S. Haberkorn. Atmospheric chemistry of CH_2BrCl, $CHBrCl_2$, $CHBr_2Cl$, $CF_3CHBrCl$, and CBr_2Cl_2. *J. Phys. Chem. A*, 102(11):1976–1986, 1998.

[14] S. Yang, G. Hou, J. Dai, C. Chang, and B. Chang. Spectroscopic investigation of the multiphoton photolysis reactions of bromomethanes ($CHBr_3$, $CHBr_2Cl$, $CHBrCl_2$, and

CH_2Br_2) at near-ultraviolet wavelengths. *J. Phys. Chem. A*, 114(14):4785–4790, 2010. PMID: 20041692.

[15] Y. Tang, L. Ji, B. Tang, R. Zhu, S. Zhang, and B. Zhang. Studies on photodissociation of alkyl bromides at 234 and 267 nm. *Chem. Phys. Lett.*, 392(4):493 – 497, 2004.

[16] P. Zou, W. S. McGivern, and S. W. North. Adiabatic and diabatic dynamics in the photodissociation of CH_2BrCl. *Phys. Chem. Chem. Phys.*, 2:3785–3790, 2000.

[17] N. S. Shuman, L. Y. Zhao, M. Boles, T. Baer, and B. Sztáray. Heats of formation of $HCCl_3$, $HCCl_2Br$, $HCClBr_2$, $HCBr_3$, and their fragment ions studied by threshold photoelectron photoion coincidence. *J. Phys. Chem. A*, 112(42):10533–10538, 2008. PMID: 18823098.

[18] A. I. Chichinin. Chemical properties of electronically excited halogen atoms x($^2p_{1/2}$) (x=f,cl,br,i). *J. Phys. Chem. Ref. Data*, 35(2):869–928, 2006.

[19] S. A. Kafafi and J. W. Hudgens. *Ab initio* calculations of the electronic structure and vibrational frequencies of the dichloromethyl radical and cation. *J. Phys. Chem.*, 93(9):3474–3479, 1989.

[20] P. B. Roussel, P. D. Lightfoot, F. Caralp, V. Catoire, R. Lesclaux, and W. Forst. Ultraviolet absorption spectra of the CH_2Cl and $CHCl_2$ radicals and the kinetics of their self-recombination reactions from 273 to 686 K. *J. Chem. Soc., Faraday Trans.*, 87:2367–2377, 1991.

[21] Y. Amatatsu, K. Morokuma, and S. Yabushita. Ab initio potential energy surfaces and trajectory studies of a-band photodissociation dynamics: $CH_3I^* \rightarrow CH_3^+I$ and $CH_3^+I^*$. *J. Chem. Phys.*, 94(7):4858–4876, 1991.

[22] W. P. Hess, D. W. Chandler, and J. W. Thoman. Photofragment imaging: the 205-nm photodissociation of CH_3Br and CD_3Br. *Chem. Phys.*, 163(2):277 – 286, 1992.

[23] G. Herzberg. *Molecular Spectra and Molecular Structure.* D. Van Nostrand Company, Inc., New York, 1966.

[24] R. Schinke. *Photodissociation Dynamics: Spectroscopy and Fragmentation of Small Polyatomic Molecules.* Cambridge University Press, Cambridge, 1993.

[25] K. E. Holdy, L. C. Klotz, and K. R. Wilson. Molecular dynamics of photodissociation: Quasidiatomic model for ICN. *J. Chem. Phys.*, 52(9):4588–4599, 1970.

[26] G. E. Busch and K. R. Wilson. Triatomic photofragment spectra. i. energy partitioning in no2 photodissociation. *J. Chem. Phys.*, 56(7):3626–3638, 1972.

[27] H. Xu, Y. Guo, S. Liu, X. Ma, D. Dai, and G. Sha. Photodissociation dynamics of CH_2I_2 molecules in the ultraviolet range studied by ion imaging. *J. Chem. Phys.*, 117(12):5722–5729, 2002.

[28] C. Zhang, Y. Zhang, S. Zhang, and B. Zhang. Photodissociation dynamics of chloroiodomethane in the Ã-band. *Acta. Phys. -Chim. Sin.*, 25(8):1708–1712, 2009.

[29] M. Cheng, D. Lin, L. Hu, Y. Du, and Q. Zhu. Photodissociation dynamics of $ICH_2Cl \rightarrow CH_2Cl + I^*/I$: photofragment translational spectroscopy at 304 and 277 nm. *Phys. Chem. Chem. Phys.*, 18:3165–3172, 2016.

[30] S. Lee, Y. Jung, and K. Jung. Photodissociation dynamics of CH_2BrCl at 234 nm. *Chem. Phys.*, 260(1–2):143 – 150, 2000.

[31] W. S. McGivern, R. Li, P. Zou, and S. W. North. Photodissociation dynamics of CH_2BrCl studied using resonance enhanced multiphoton ionization (rempi) with time-of-flight mass spectrometry. *J. Chem. Phys.*, 111(13):5771–5779, 1999.

[32] J. Zhou, K. Lau, E. Hassanein, H. Xu, S. Tian, B. Jones, and C. Y. Ng. A photodissociation study of CH_2BrCl in the $\tilde{A}$-band using the time-sliced ion velocity imaging method. *J. Chem. Phys.*, 124(3):034309, 2006.

[33] Q. Li, R. Zhu, J. Lu, X. Zhang, and B. Tang. Vibrational excitations in chloromethyl radical formed by the photodissociation of chlorobromomethane. *J. Chem. Phys.*, 140(3):034303, 2014.

[34] S. H. Gardiner, M. L. Lipciuc, T. N. V. Karsili, M. N. R. Ashfold, and C. Vallance. Dynamics of the $\tilde{A}$-band ultraviolet photodissociation of methyl iodide and ethyl iodide via velocity-map imaging with 'universal' detection. *Phys. Chem. Chem. Phys.*, 17:4096–4106, 2015.

[35] C. Paterson, F.G. Godwin, and P.A. Gorry. Photofragmentation dynamics of C_2H_5I and CF_3CH_2I at 248 nm. *Mol. Phys.*, 60(4):729–747, 1987.

[36] M. D. Brynteson, C. C. Womack, R. S. Booth, S. H. Lee, J. J. Lin, and L. J. Butler. Radical intermediates in the addition of OH to propene: Photolytic precursors and angular momentum effects. *J. Phys. Chem. A*, 118(18):3211–3229, 2014. PMID: 24758210.

Chapter 4

Flow tube apparatus

4.1 Overview

Studies of elementary gas-phase kinetics support a variety of broader investigative efforts in combustion analysis, astrochemistry, and atmospheric chemistry. For instance, the reliability of atmospheric models, which have implications for policy regarding air quality, human health, and climate, depends on accurate reaction rate data. To this end, studies of bimolecular rate constants near 300 K have widely utilized the flow tube technique.[1] The essential feature of a flow tube apparatus is a vacuum system that pulls a sample at a well-defined flow rate through a tube. Reactions begin in one portion of the tube and products are detected in another. Varying the time between reaction initiation and product detection yields kinetics information. An assortment of traditional flow tube techniques exist, but most variants seek to measure bimolecular rate constants, typically with a movable injector that initiates reactions in different regions of the flow tube. Spectroscopic or mass-spectrometric detection then quantifies the appearance of products (or disappearance of reactants). These studies typically deliver one reactant well in excess of the other, so that reactions proceed with pseudo first-order kinetics.

We designed and fabricated a new flow tube apparatus to study unimolecular decomposition. Rather than utilize an injector to initiate bimolecular reactions, we photodissociate a precursor species entrained in the flow using a pulsed ns-laser. We probe the products of the photodissociation (or subsequent chemistry) after they are transported in the flow to

a laser-induced fluorescence (LIF) detection region. By studying unimolecular reactions in our flow tube, we forego the excess reagent and thorough mixing required in a bimolecular experiment. Our setup also offers precision in terms of timing, bond-cleavage specificity, and species-specific probing by employing narrow-bandwidth laser pulses. Additionally, our flow tube apparatus easily adapts to more than one configuration, which provides flexibility in terms of characterization and kinetics timescales of interest. This chapter details the components of the flow tube and the methods of characterization we employ to prepare the apparatus for kinetics measurements of atmospherically relevant unimolecular chemistry.

4.2 General description

The flow tube apparatus consists of four distinct regions: the flow development region, the photolysis region, the flow characterization region, and the LIF region. Figure 4.1 depicts these regions and the two configurations we assemble the flow tube in. Typically, gaseous samples are introduced to the flow tube through the flow development region. In the "long-flow" configuration, the flow development region leads to the photolysis region where unimolecular photodissociation is initiated by a pulsed-ns laser before the sample is passed into the flow characterization region. In the "short-flow" configuration, the flow characterization region comes before the photolysis region. In either configuration, the sample subsequently passes through the LIF region where products are detected using LIF.

Stainless steel (SS) tubing with a 34-mm ID makes up the main body of the flowtube, and fittings for windows, gauges, probes, etc. are welded or flanged to the tube. A corrosion-resistant inert coating (SiloTek Coproration, Dursan) covers the inner portion of the tube.

Figure 4.1: Diagram of the flow tube in both configurations. Optical components are blue. The long-flow configuration (top) puts the flow characterization region between the photolysis region and the LIF region. The short-flow configuration (bottom) puts the photolysis region between the flow characterization region and the LIF region. Nominal lengths are based off the machine shop drawings but may vary by a few mm.

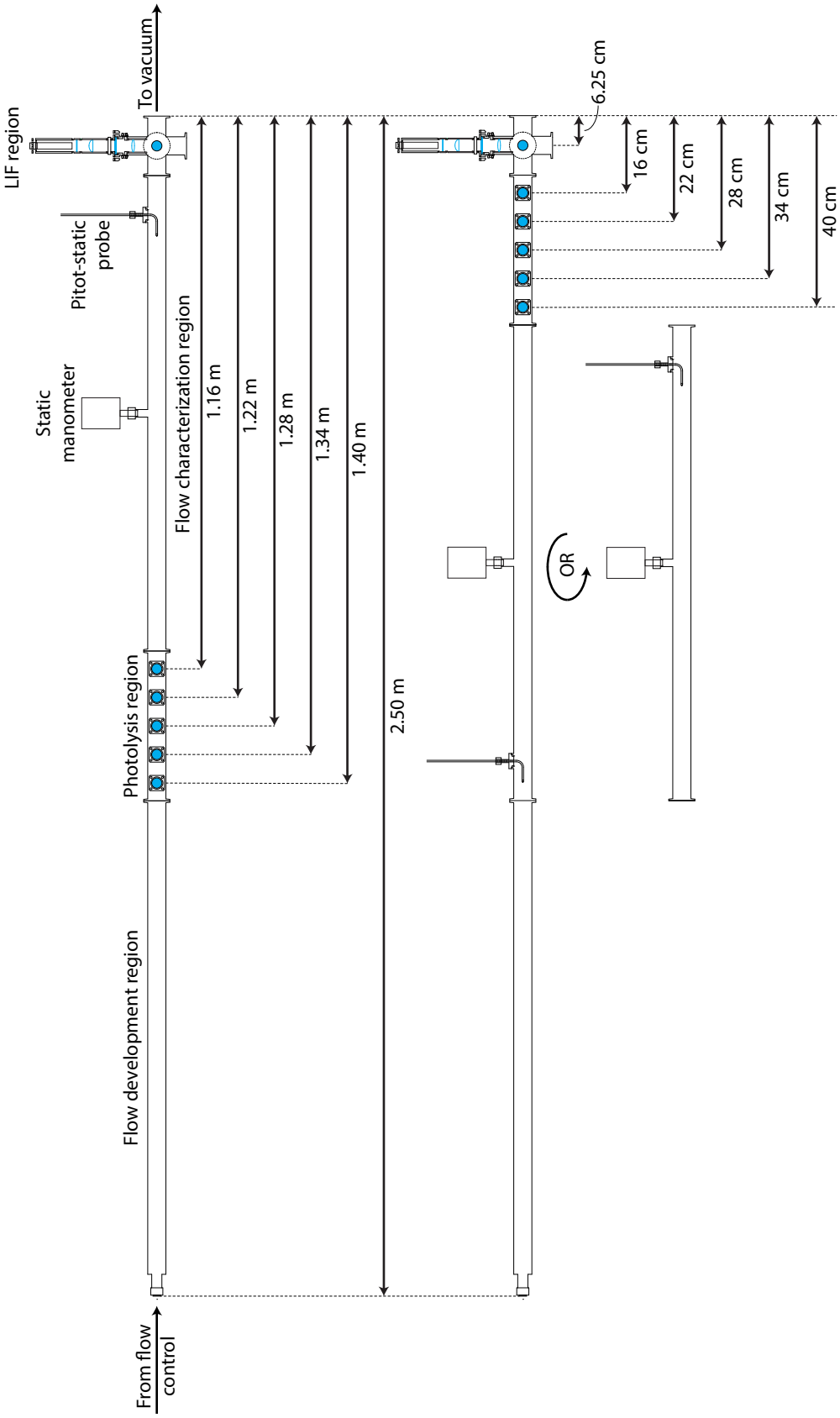
To vacuum
LIF region
Pitot-static probe
Static manometer
Flow characterization region
1.16 m
1.22 m
1.28 m
1.34 m
1.40 m
2.50 m
Photolysis region
Flow development region
From flow control
6.25 cm
16 cm
22 cm
28 cm
34 cm
40 cm
OR

The tube is mounted on four home-built supports that adjust to keep the tube level. Figure 4.2 shows a drawing of the mount. Not shown in the drawing are two additional 0.25-inch threaded holes on top of the mount that we use to secure a bracket on the top side of the flow tube that keeps the tube flush with the mount. We found this was necessary because the welding on the tubing induced a curvature on the flow characterization region, so leveling the flow tube is impossible without securing it to the mounts. Because the regions are held together by Kwik-Flange connections with o-rings, there is some play in the rigidity of the apparatus that allows us to level it without significant strain.

4.2.1 Sample introduction and vacuum system

Nitrogen and oxygen are carrier gases for liquid samples we introduce to the flow tube. A home-built SS containment houses the liquid samples. The sample resides in a PTFE reservoir inside the containment. The containment has a bored-through 0.25-inch Swagelok connection where the gas is introduced to bubble through the liquid or flow over the head space. Pressurized cylinders house the carrier gasses and 0.25-inch ID PTFE tubing brings the gas into the sample containment. The outlet of the sample containment has a KF-40 connection, which allows us to interface it directly with the LIF-region if we wish to introduce the sample with minimal recondensation or wall loss. We typically use a KF-40 to 0.25-inch Swagelok adapter and additional PTFE tubing to introduce the sample *via* mass flow controllers (MFCs) at the other end of the flow tube. The forelines leading to the MFCs are kept at 20-30 psi by gas regulators (Matheson, 3530A).

The majority of the work detailed in this thesis uses two MFCs, operating simultaneously

Figure 4.2: Machine shop drawing for the flow tube mounts. Not shown in the diagram are additional threaded 0.25-inch holes on the top of the mounts that are used to secure a bracket on the top side of the flow tube. Lengths are shown in inches.

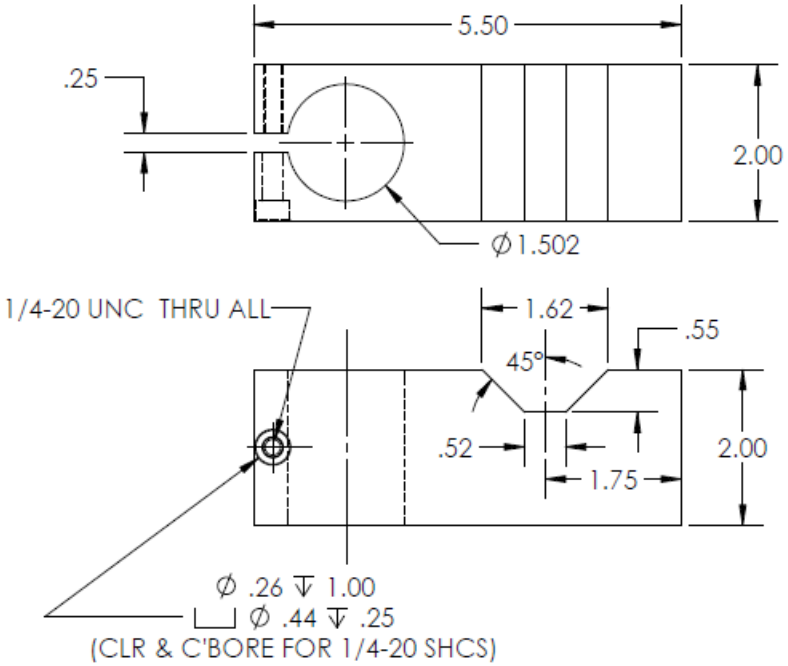
5.50
.25
2.00
Ø1.502
1/4-20 UNC THRU ALL
1.62
.55
45°
.52
1.75
2.00
Ø .26 ↧ 1.00
⌴ Ø .44 ↧ .25
(CLR & C'BORE FOR 1/4-20 SHCS)

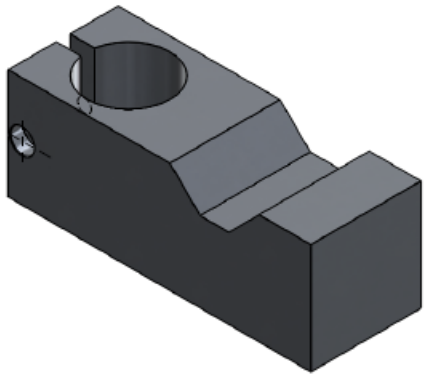

or (more often) independently, to achieve a desired flow rate through the tube in standard liters per minute (SLM). One MFC contains metal seals and is calibrated for nitrogen flow (MKS Instruments, GM50A013304RBM020), the other contains Kalrez elastomer seals and is calibrated for oxygen flow (MKS Instruments, GE50A015304RBK020). The elastomer-sealed MFC is generally better suited for introducing reactive samples. Both MFCs have a full scale flow range of 30 SLM and Swagelok 4 VCR male fittings at the inlet and outlet ports. Since the MFCs do not feature positive shut-off capabilities, we run the outlet of each MFC through a needle valve that can provide positive shut off as needed. The valves lead to a three-way cross where mixing takes place if both MFCs are in use, and the mixture continues to the flow development region of the flow tube. The flow rate is monitored and controlled by a vacuum system controller (MKS Instruments, Series 946). Section 4.3 will cover details of the flow control capabilities and procedures. The characterization and experiments described herein all utilize the MFCs described above unless otherwise noted.

Additionally, we use a mass flow meter (MFM) capable of flow rate measurement (but not control) that facilitates flows up to 200 SLM (Aalborg, GFMS-010016). We also have an MFC similar to the 30 SLM MFCs but with a full scale flow range of 250 SLM calibrated for nitrogen flow (MKS Instruments, GE250A013255TBV0020). The 250 SLM MFC features viton elastomer seals and Swagelok 8 VCR fittings at the intlet and outlet ports. These high flow-rate devices make turbulent flows possible (see Section 4.3.1).

A single-stage, oil-sealed rotary vane pump (Œrlikon Leybold, Sogevac SV200-BR2) evacuates the flow tube and facilitates transport through the tube in conjunction with the MFCs or MFM. The nominal pumping speed of the pump is 220 m^3h^{-1}, but it operates closer to 200 m^3h^{-1} with clean oil. This pumping speed should be sufficient to reach pressures below

8×10^{-2} mbar with the gas ballast closed and 0.7 mbar with the gas ballast open. There is a particle filter at the inlet of the pump (Œrlikon Leybold, F 200-300 Paper cartridge - DN 63 ISO-K) capable of removing particulate as small as 5 μm in diameter. The foreline between the pump and the flow tube consists of KF-40 flanged SS tubing. A thermocouple gauge (Agilent, Type 0531) connected to a controller (Varian, 843) reads the pressure in the vacuum foreline. There are two valves on the foreline between the particle filter and the flow tube: a ball valve (Edwards, C360-00-300) and a diaphragm valve (Edwards,SP40K Speedivalve FKM GP Diaphragm). We typically use the ball valve to isolate the pump and the diaphragm valve to throttle the flow.

4.2.2 Flow development region

The flow development region is where the flow becomes uniform and therefore amenable to characterization of reproducible transport properties. Figure 4.3 depicts the flow development region. A 5/8-inch Swagelok connection couples the MFC output to the entrance of the flow development region, which is 39-inches long. Upon entering the region, viscous forces propagate from the interior of the pipe wall towards the center of the flow, and viscous forces within the fluid compensate for this disturbance. As these viscous effects equilibrate, local flow velocities are in flux, and the distance traveled during this time is known as the hydrodynamic entrance length. Section 4.3.1 will consider this length in more detail for the regimes we wish to investigate. Once the flow is uniform, the radial velocity profile is constant as transport continues down the tube. It is necessary to develop uniform flow prior to the photolysis region in order to extract reliable kinetics data. In the long-flow configu-

Figure 4.3: Machine shop drawing for the flow development region of the flow tube. Lengths are shown in inches.

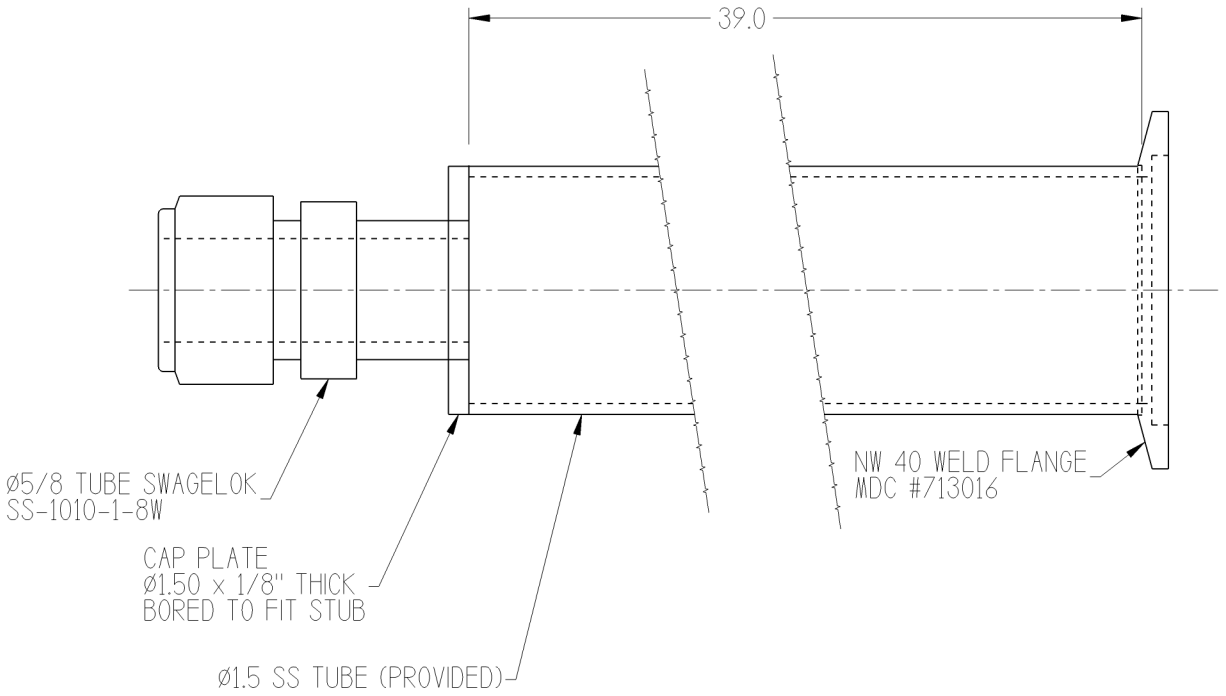
39.0
Ø5/8 TUBE SWAGELOK
SS-1010-1-8W
CAP PLATE
Ø1.50 x 1/8" THICK
BORED TO FIT STUB
Ø1.5 SS TUBE (PROVIDED)
NW 40 WELD FLANGE
MDC #713016

ration, the flow covers only the 39-inch length of the flow development region before passing to the photolysis region, but in the short-flow configuration the flow passes through the flow characterization region as well, resulting in a total length of 78 inches prior to photolysis (see Figure 4.1).

4.2.3 Photolysis region

In the photolysis region, a ns laser pulse photodissociates a precursor to initiate the unimolecular chemistry we wish to study. For the purposes of characterization, we photodissociate HNO_3 to generate OH and NO_2, but future studies could produce OH (or another product amenable to LIF detection) in a less direct manner. Figure 4.4 depicts the region. It consists of five sets of two windows on opposite sides of the flow tube. The center-to-center distance between the windows is 2.36 inches, and the full length of the region is 12.39 inches. By choosing which window to send the laser through, we vary the transport length to the LIF probe, and thus, the reaction time for a given flow rate. The unabsorbed photons pass through the opposite side of the flow tube where they may be dumped, or used to monitor laser power.

4.2.4 Flow characterization region

In the flow characterization region of the apparatus, static and differential pressure measurements characterize transport properties of the flow. This section will cover the components of the region, and Section 4.3 will detail how these measurements are used for flow characterization. Figure 4.5 shows a drawing of the flow characterization region.

Figure 4.4: Machine shop drawing for the photolysis region of the flow tube. Lengths are shown in inches.

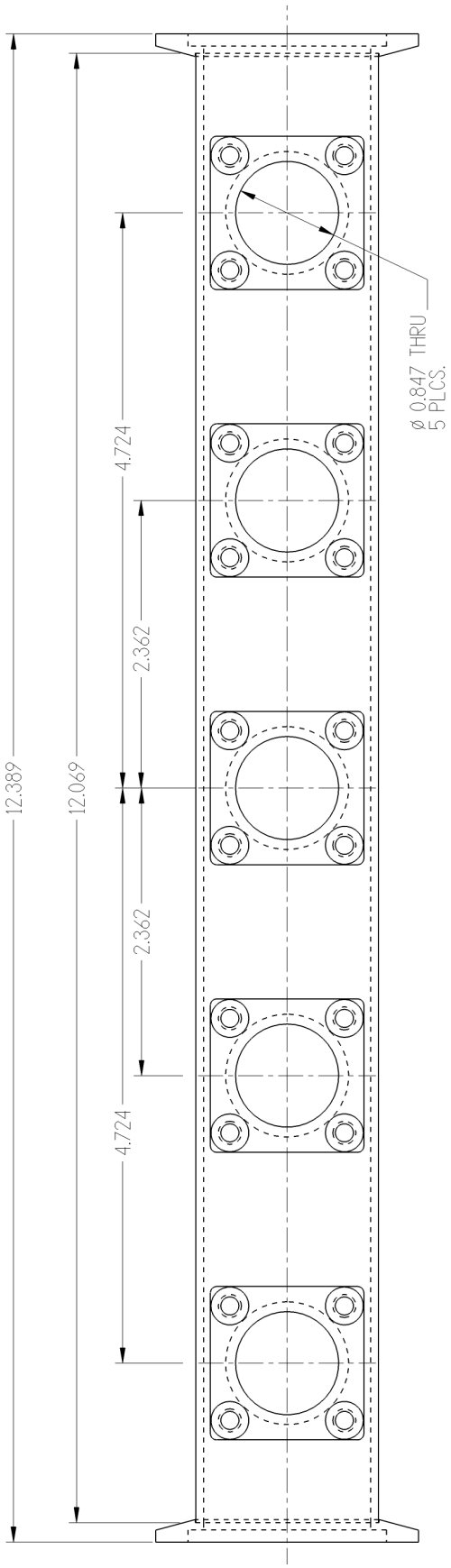
ø 0.847 THRU
5 PLCS.
4.724
2.362
2.362
4.724
12.069
12.389

Figure 4.5: Machine shop drawing for the flow characterization region of the flow tube. Lengths are shown in inches.

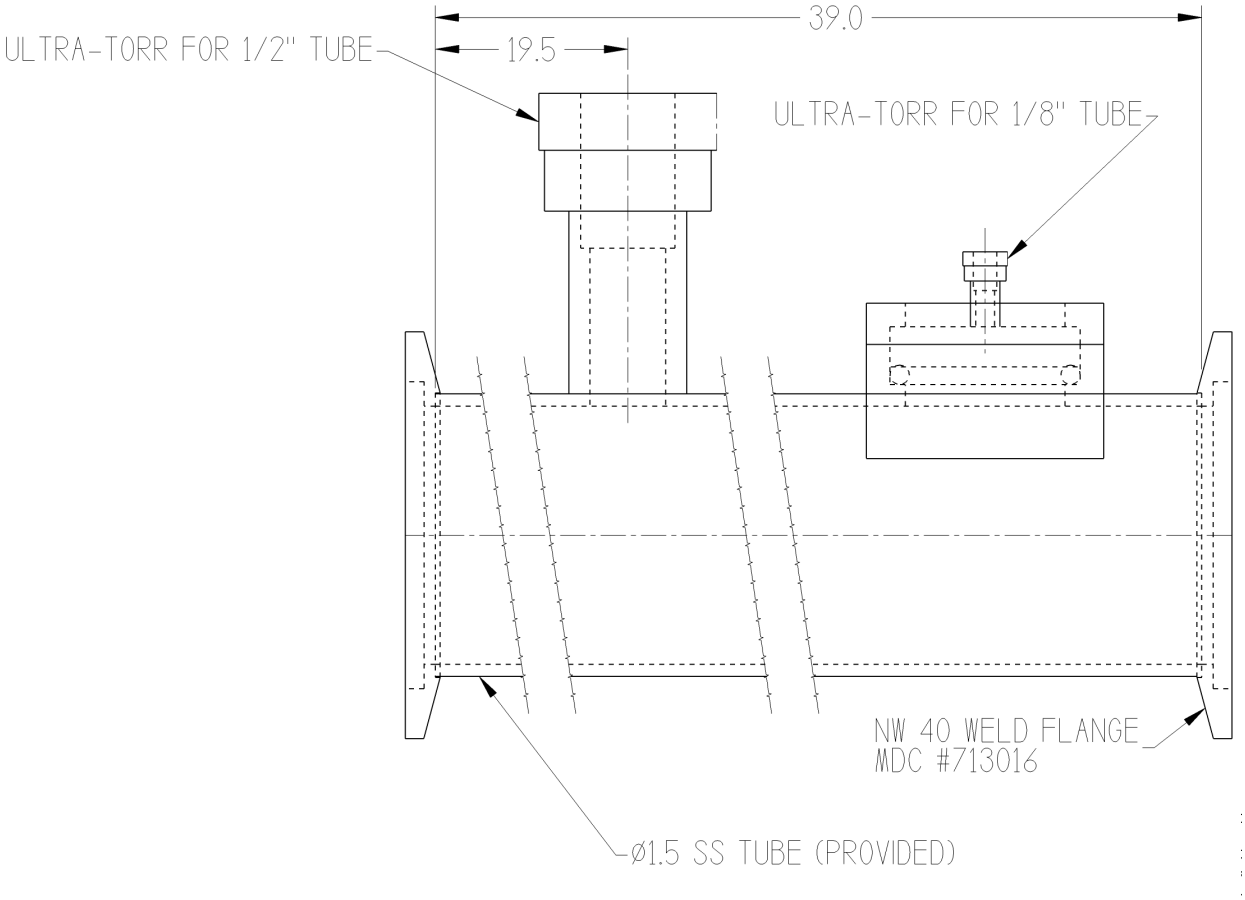
39.0
19.5
ULTRA-TORR FOR 1/2" TUBE
ULTRA-TORR FOR 1/8" TUBE
NW 40 WELD FLANGE
MDC #713016
Ø1.5 SS TUBE (PROVIDED)

Figure 4.6: Machine shop drawing for the plug adapter for the pitot-static tube. When the pitot-static tube is not in use, a similar plug is used without the Ultra-Torr component and through-hole. Lengths are shown in inches.

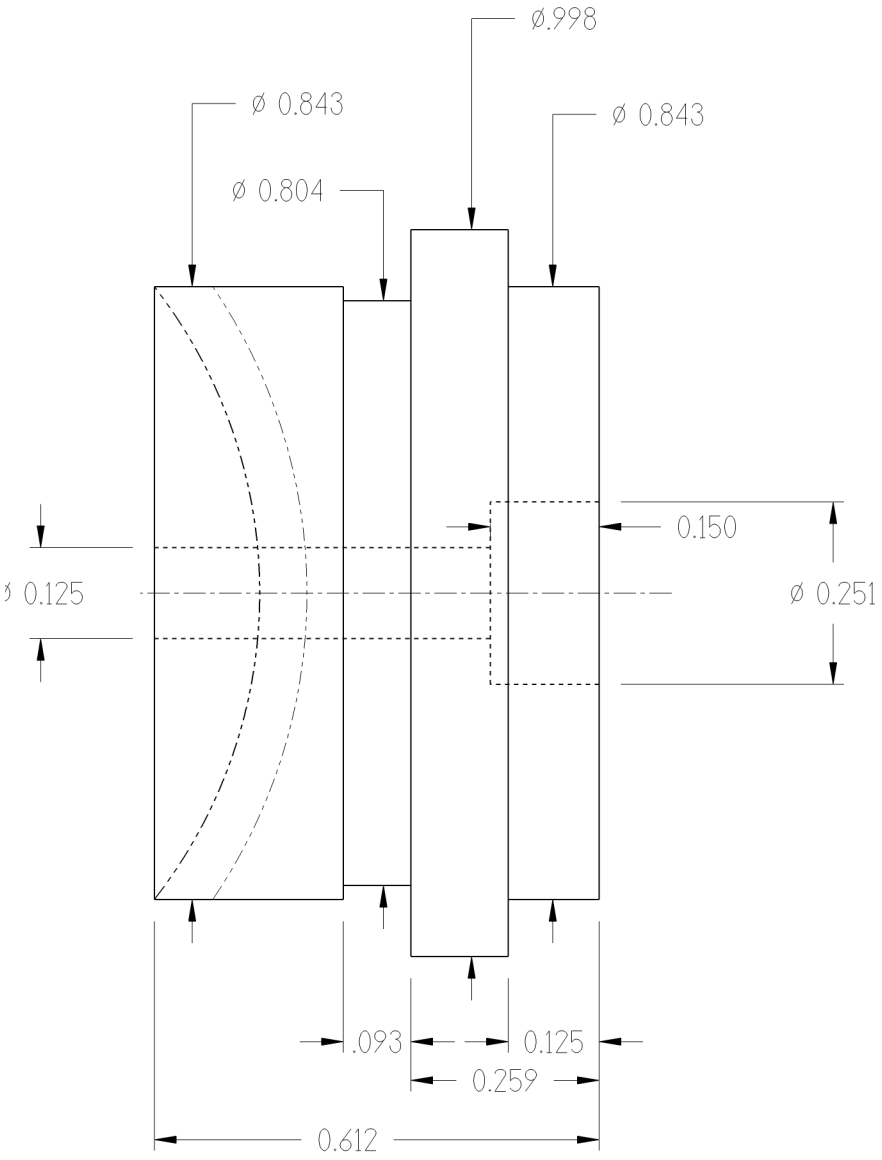
Ø.998
Ø 0.843
Ø 0.843
Ø 0.804
0.150
Ø 0.125
Ø 0.251
.093
0.125
0.259
0.612

A Baratron absolute capacitance manometer (MKS Instruments, 626C13TAD) quantifies the static pressure in the tube through a 1/2-inch Ultra-Torr fitting welded at the midpoint of the 39-inch span of the region. The absolute manometer has a 1000 Torr full scale range with 0.1 Torr resolution and ±0.15% accuracy. A pitot-static tube (United Sensor, PCC-8-KL) engages the flow tube through a 1/8-inch Ultra-Torr fitting. This fitting is welded to a plug adapter that is rounded on the bottom half to maintain the shape of flow tube's inner circumference. Figure 4.6 shows a drawing of the adapter. When the pitot-static tube is not in use, the adapter is replaced with a blank of the same shape (but no Ultra-Torr component and through-hole). The height of the pitot-static tube is controlled by a height gauge (Mitutoyo 570) with 0.01-mm resolution. We set the pitot-static tube radially in the flow, where it makes localized "head-on" dynamic pressure measurements and "side-on" static pressure measurements. The difference between these pressures is monitored by a Baratron differential manometer (MKS Instruments, 220DD-00001B2B) with a 1-Torr full scale range, 0.01-Torr resolution, and ±0.15% accuracy. We interface both of the Baratron manometers with the vacuum controller system used to control the MFCs (MKS Instruments, Series 946).

4.2.5 LIF region

In the LIF region we detect products generated by the chemistry initiated in the photolysis region. This region consists of a six-way SS cross with KF-40 flanges at each port. One port couples to the rest of the flow tube, and the vacuum foreline couples to the port on the opposite side. UV fused silica windows (Thorlabs, VPW42-UV) at ports perpendicular to

the flow tube transmit laser light into the LIF region to excite products. We machined the face plate for these window ports to mate with components from Thorlabs with male SM1 threading (1.035-40). Often we use the threading for alignment targets (Thorlabs, SM1A7) or lens tubes. We have found focusing the LIF light is not necessary to generate LIF signal, but it does aid in selecting the center of the flow for detection.

The port extending upwards from the flow tube couples to a photomultiplier tube (PMT) assembly, which collects fluorescence generated by the relaxation of excited products. The port extending below the flow tube can couple to the sample containment described in Section 4.2.1. Figure 4.7 shows the PMT assembly in detail. A number of components on the PMT assembly are home built, indicated in red. Figure 4.8 shows the drawings for each retainer. Parts of the PMT assembly that engage with threading have 1.035-40 threads, which are compatible with SM1 components offered by Thorlabs. The flange retainer and the home-built lens tube it secures are stainless steel, and the lens tube has identical dimensions to the aluminum SM1L15 lens tube from Thorlabs. Stainless steel is ideal for these two components since they are situated within the six-way cross of the photolysis region and thus exposed to the sample under study.

Fluorescing molecules emit light in all directions. The optics in the PMT assembly act to collect as much of that diverging light as possible on the PMT while limiting the amount of scattered laser light reaching the PMT. To achieve this, a 50-mm focal length biconvex lens (Thorlabs, LB4096) focuses the divergent light from the center of the LIF region through a UV fused silica window (Thorlabs, VPW42) to an adjustable iris (Thorlabs, SM1D12D). A 35-mm focal length plano-convex lens (Thorlabs, LA4052-UV) collimates the light diverging on the opposite side of the iris. The collimated light passes through one or more bandpass

Figure 4.7: Cross section of the PMT assembly for detecting LIF signal. Optical components are blue and various home-built retainers (shown in detail in Figure 4.8)are red. The divergent fluorescence (yellow) is focused through an iris and then collimated onto the PMT.

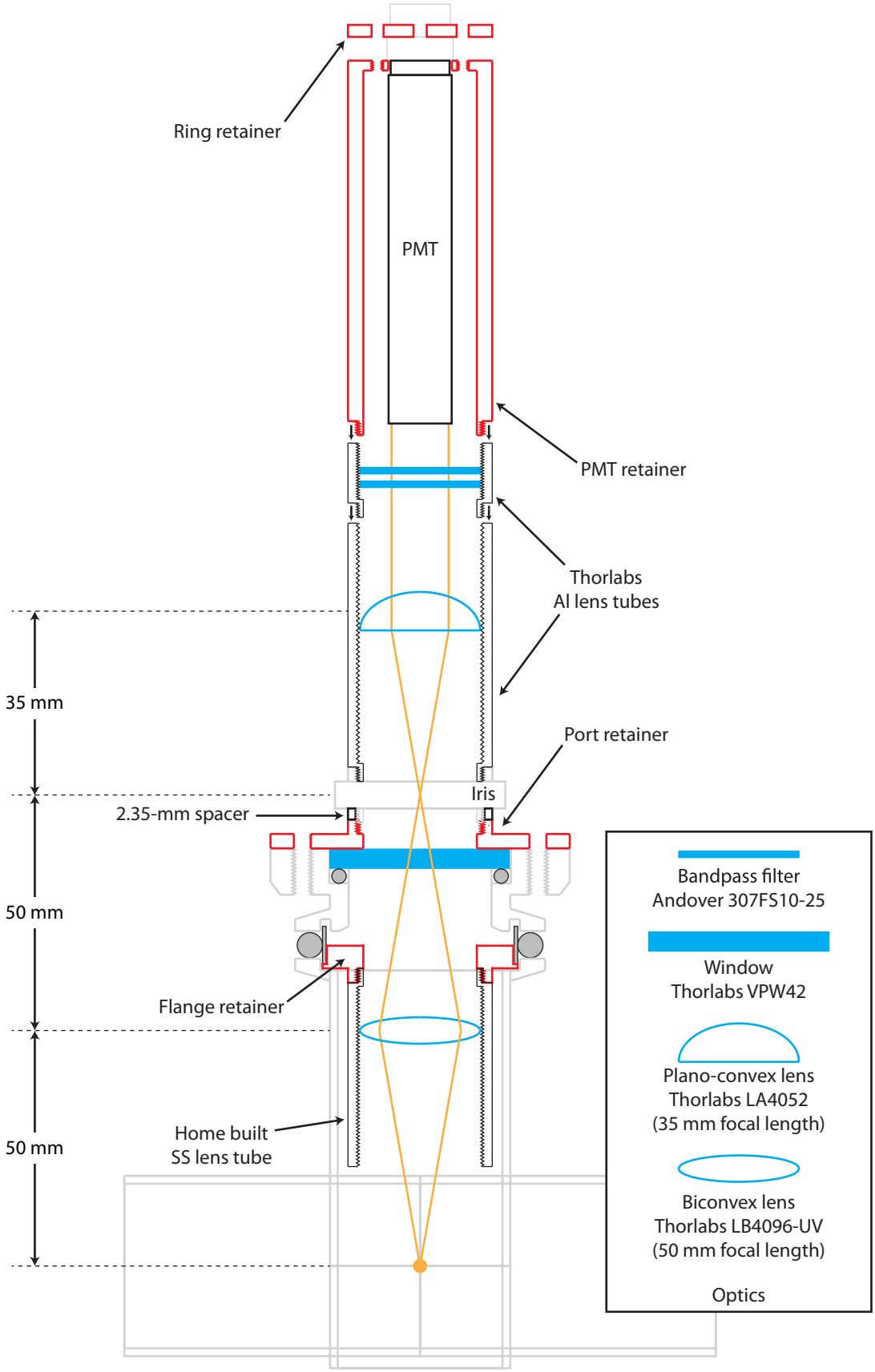
Ring retainer
PMT
PMT retainer
Thorlabs
Al lens tubes
Port retainer
Iris
2.35-mm spacer
35 mm
50 mm
50 mm
Flange retainer
Home built
SS lens tube
Bandpass filter
Andover 307FS10-25
Window
Thorlabs VPW42
Plano-convex lens
Thorlabs LA4052
(35 mm focal length)
Biconvex lens
Thorlabs LB4096-UV
(50 mm focal length)
Optics

Figure 4.8: Drawings of the various home-built retainers for the PMT assembly. Each drawing shows the side view of the retainer above the top view. The SS flange retainer holds a home-built SS lens tube in place inside the flow tube. The port retainer replaces the face plate of a commercial window port and is threaded to couple with an iris. The aluminum PMT and ring retainers are anodized black to minimize scattered light. All of the threading for the retainers is machined for compatibility with Thorlabs SM1 components (1.035-40). Lengths are shown in inches.

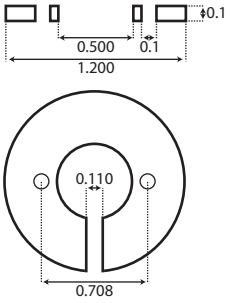

Ring retainer

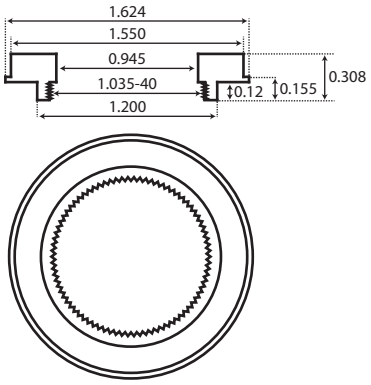

Flange retainer

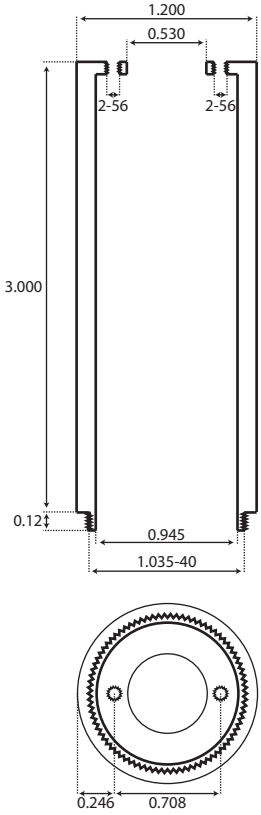

PMT retainer

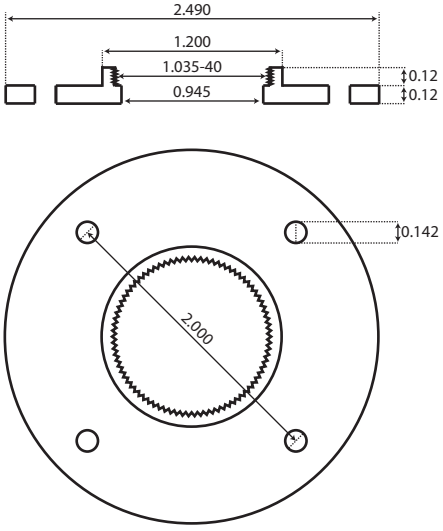

Port retainer

filters (Andover Corporation, 307FS10-25) centered at 307.1 nm with a 10-nm FWHM before impinging on the PMT. The number of bandpass filters we use depends on the strength of the signal. This particular bandpass filter is well suited for LIF on OH products (more on this in Section 4.4). Spacer rings set the height of the optics in the lens tubes.

The PMT (Hamamatsu, R960) is a head-on type with UV-glass rated for spectral response from 185–650 nm. The ten dynodes on the PMT connect to a D-type socket assembly (Hamamatsu, E849-90) that serves as a voltage divider. The socket assembly is connected to a high-voltage DC power supply (Hamamatsu, C9525) that delivers -1250 kV to the PMT. A BNC cable leading from the socket assembly carries a current signal proportional to the incident light on the PMT.

4.2.6 Laser setup and flame box

The laser setup is similar to that for the molecular beam apparatus, and both legs (photolysis and LIF) have a similar configuration. Figure 4.9 shows the laser setup schematically for the long-flow configuration of the flow tube. The photlysis light in the figure is sent through the first window in the photolysis region, but is easily realigned through the other windows. We can also send both lasers into the LIF region for characterization purposes. On both legs, the first harmonic of an Nd:YAG laser (Spectra-Physics, Lab 170) running at 20 Hz pumps a dye laser (Continuum, ND6000). A β-barium borate (BBO) crystal facilitates second harmonic generation (SHG) of the dye output, and a color filter (Thorlabs, FGUV11M) separates the harmonic from the fundamental. A wavemeter (Coherent, WaveMaster) reads the dye wavelength from the back-reflection off the color filter. On the LIF leg, the BBO crystal

Figure 4.9: Schematic of the laser setup for the flow tube apparatus in the long-flow configuration. We utilize other setups for characterization purposes, such as short-flow configuration and overlapping the beams in the LIF region, but we generate light in those cases in the same manner.

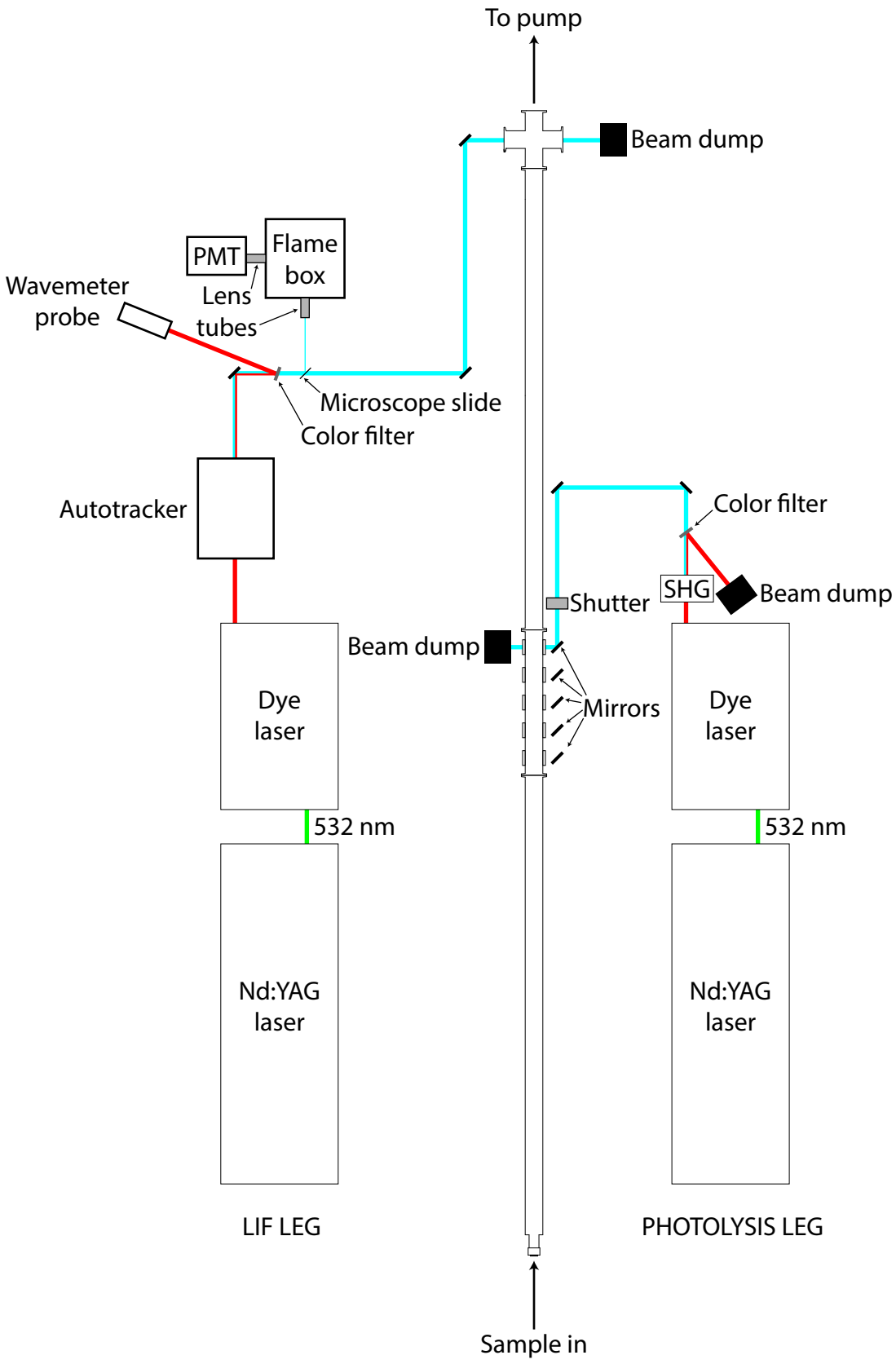
To pump
Beam dump
PMT
Flame box
Wavemeter probe
Lens tubes
Microscope slide
Color filter
Autotracker
Color filter
SHG
Beam dump
Shutter
Beam dump
Mirrors
Dye laser
Dye laser
532 nm
532 nm
Nd:YAG laser
Nd:YAG laser
LIF LEG
PHOTOLYSIS LEG
Sample in

is housed in an autotracker (Inrad Optics, AT-II) that maintains SHG during wavelength scanning. The photolysis light passes through a shutter (Thorlabs, SHB1T) before entering the photolysis region. Shuttering the photolysis light allows us to take difference spectra, whereby the LIF-only signal is subtracted from the two-color signal. We typically send 3-4 mJ of UV light into the photolysis region.

The flame from a Bunsen burner is a convenient source of OH with high number density. We therefore constructed a flame box to find OH LIF transitions more easily. Figure 4.10 contains the drawings for the components of the flame box we machined. A quartz microscope slide splits off a small amount ($\sim 1\%$) of the LIF beam and sends it into the flame box through a 100-mm focal length plano-convex lens (Thorlabs, LA4380-UV) focused into the center of the flame. This light excites OH radicals generated by the flame when tuned to a resonant rovibronic transition in the radical. The excited OH radicals relax, and a portion of their fluorescence is focused through a second 100-mm focal length plano-convex lens (Thorlabs, LA4380-UV) perpendicular to the beam path. Both lenses are mounted in adjustable lens tubes (Thorlabs, SM1V15) that fine tune their focus into the flame. The light leaving the flame box travels through baffling and impinges on a PMT (Thorlabs, PMTSS) powered by a home-built 9-V variable power supply. We remove a plug on the side of the flame box to light the Bunsen burner and replace it during scans to maintain a consistent flame. The inside of the flame box is painted with a flat black finish to minimize scatter. By finding transitions with the flame box, we ensure that our LIF laser is tuned to the correct wavelength before searching for signal in the flow tube.

Figure 4.10: Machine shop drawings of the various flame box components The main body of the flame box is a square tube with various holes cut for lens tubes, natural gas tubing, and a large plug. We drilled additional holes not shown in the drawing near the bottom of the square tube to improve air flow. The square tube couples to a slotted base with a recessed area in the center where the Bunsen burner sits.

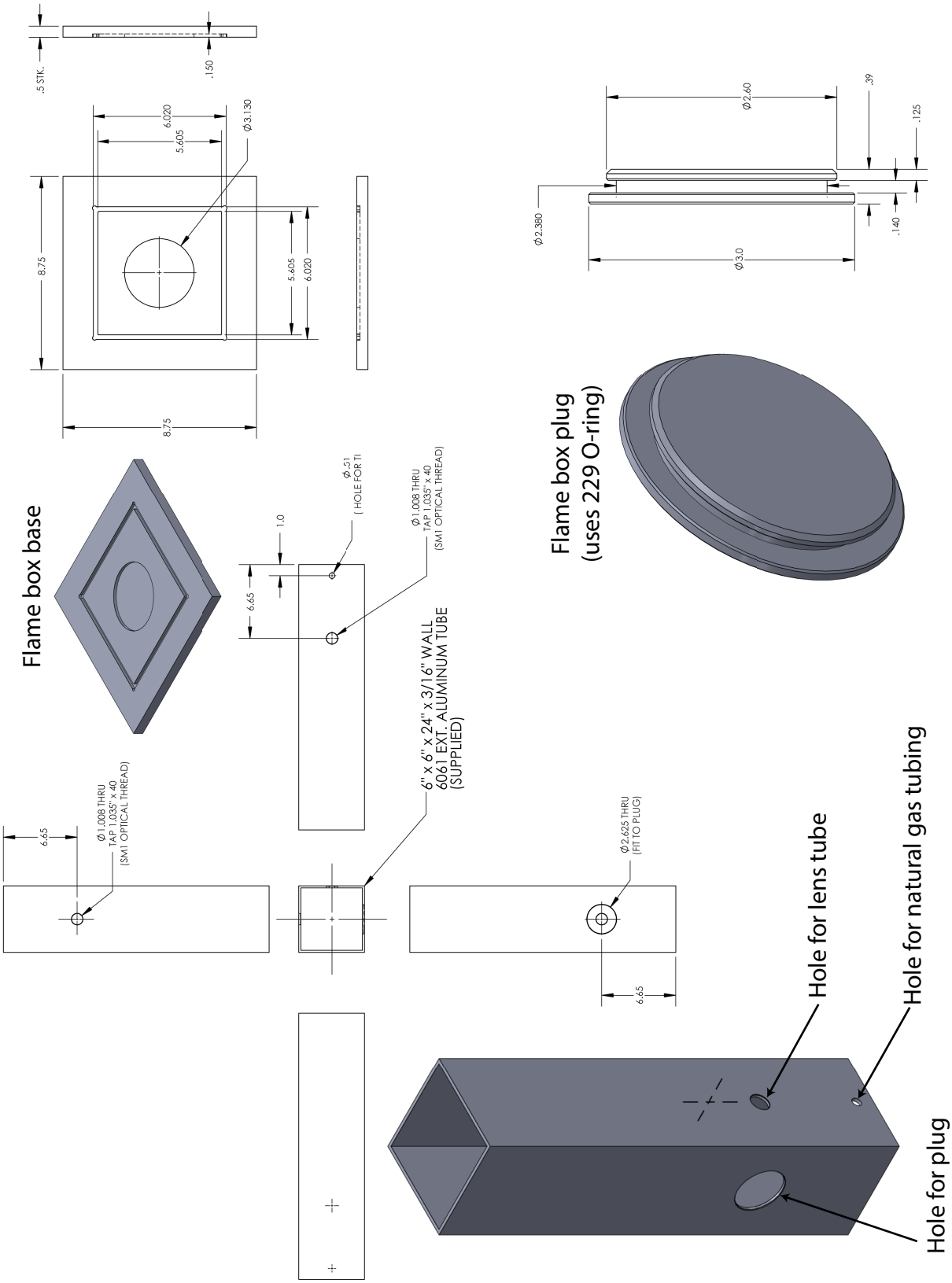
.5 STK.
.150
6.020
5.605
Ø3.130
8.75
5.605
6.020
8.75
Flame box base
Ø .51
(HOLE FOR T1
1.0
6.65
Ø 1.008 THRU
TAP 1.035" x 40
(SM1 OPTICAL THREAD)
6" x 6" x 24" x 3/16" WALL
6061 EXT. ALUMINUM TUBE
(SUPPLIED)
Ø 1.008 THRU
TAP 1.035" x 40
(SM1 OPTICAL THREAD)
6.65
Ø 2.625 THRU
(FIT TO PLUG)
6.65
Ø 2.60
.39
.125
Ø 2.380
Ø3.0
.140
Flame box plug
(uses 229 O-ring)
Hole for lens tube
Hole for natural gas tubing
Hole for plug

4.2.7 Data collection, timing, and LabView code

A PC (Dell, Precision Tower 5810) handles the data collection and automation for the flow tube apparatus. The PC has five PCIe slots and a conventional PCI slot on the motherboard, which makes it compatible with modern peripheral components but still capable of utilizing older connectivity standards as needed. We updated the operating system to a 64-bit version of Windows 10 and installed LabView 2015. The same stepper control card (National Instruments, PCI-7334) used in the molecular beam apparatus to drive the stepper motors in the dye lasers plugs into the PCI slot of the new PC. The stepper control card communicates with the dye lasers *via* a 68-pin I/O connector block (National Instruments, CB-68-LP) housed in a breakout box built by Andrew Berke.[2] We updated Cornelia Heid's code[3] for communicating with the dye laser stepper motors. The newest version of this code is `MoFlow_Dye_Mover_v3.vi`. The PC also contains a serial port we use for RS-232 communication with the wavemeter to read in the dye laser wavelength with LabView. The code for this communication is contained in `WL_reader.vi`. Appendix B contains details of these LabView VIs.

A multifunction I/O device (National Instruments, PCIe-6321) handles analog (AI) and digital (DI) inputs and generates digital outputs (DO) for the flow tube experiments. The device is part of the DAQ X Series offered by National Instruments, and we refer to it as the DAQ card herein. A homebuilt breakout box with BNC connections houses a connector block (National Instruments, SCB-68A) for the DAQ card. The breakout box mediates the exchange of AI, DI, and DO signals between the DAQ card and the instrumentation we use. Figure 4.11 diagrams the connections leading to the DAQ card *via* the connector block. We wire AI signal sources with a differential configuration to the connector block. This means we use two AI terminals (AI+ and AI-) and an AI ground (AI GND) terminal on the connector block for each AI signal. Figure 4.12 highlights which terminals on the DAQ card accept the AI+ and AI- signals for our apparatus and the corresponding differential wiring diagram we utilize for each AI source in the connector block. Differential connections are ideal for signal sources with isolated grounds. Because two AIs are used simultaneously for a single source, the DAQ card can reject noise common to both inputs. By wiring a 100 kΩ bias resistor between the negative signal source and AI GND, we improve this common-mode rejection by balancing the noise coupled electrostatically to AI+ and AI- that would otherwise be present mostly in AI+.

A boxcar averager (Stanford Research Systems, SR250) processes signal from the PMT (on the LIF region or the flame box) prior to the breakout box. The scattered laser light and LIF signal associated with each laser pulse only persists for 10s of ns, which is too fast for the DAQ card to measure reliably without the use of the boxcar averager. We set the boxcar gate on the LIF signal and pass the last sample output from the boxcar averager to the breakout box using differential connections AI terminals 1 and 9.

Figure 4.11: Diagram of the connections leading to the DAQ card *via* the connector block in the breakout box. Color coding is only intended to guide the eye for individual signals. Labels for inputs and outputs are device-specific wherever possible.

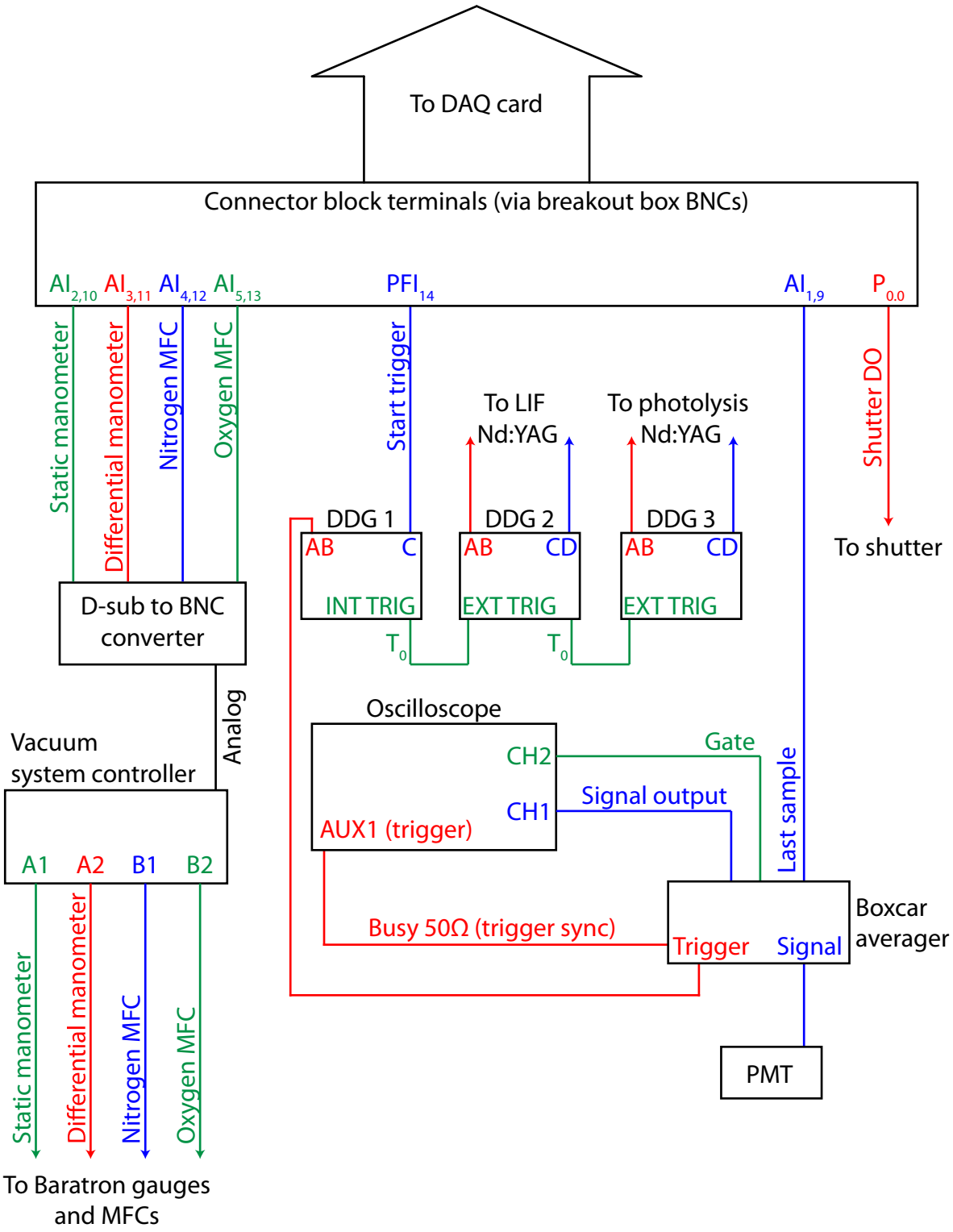
To DAQ card
Connector block terminals (via breakout box BNCs)
AI2,10
AI3,11
AI4,12
AI5,13
PFI14
AI1,9
P0.0
Static manometer
Differential manometer
Nitrogen MFC
Oxygen MFC
Start trigger
To LIF Nd:YAG
To photolysis Nd:YAG
Shutter DO
To shutter
DDG 1
AB
C
INT TRIG
DDG 2
AB
CD
EXT TRIG
DDG 3
AB
CD
EXT TRIG
T0
T0
D-sub to BNC converter
Analog
Vacuum system controller
A1
A2
B1
B2
Oscilloscope
CH2
CH1
AUX1 (trigger)
Gate
Signal output
Last sample
Busy 50Ω (trigger sync)
Trigger
Signal
Boxcar averager
PMT
Static manometer
Differential manometer
Nitrogen MFC
Oxygen MFC
To Baratron gauges and MFCs

Figure 4.12: Pinouts for the DAQ card an wiring diagram for the differential configuration we use to read in AI signals. Pairs of AI+ and AI- terminals we use for the differential connections are color coded.

National Instruments
PCIe-6321 pinouts

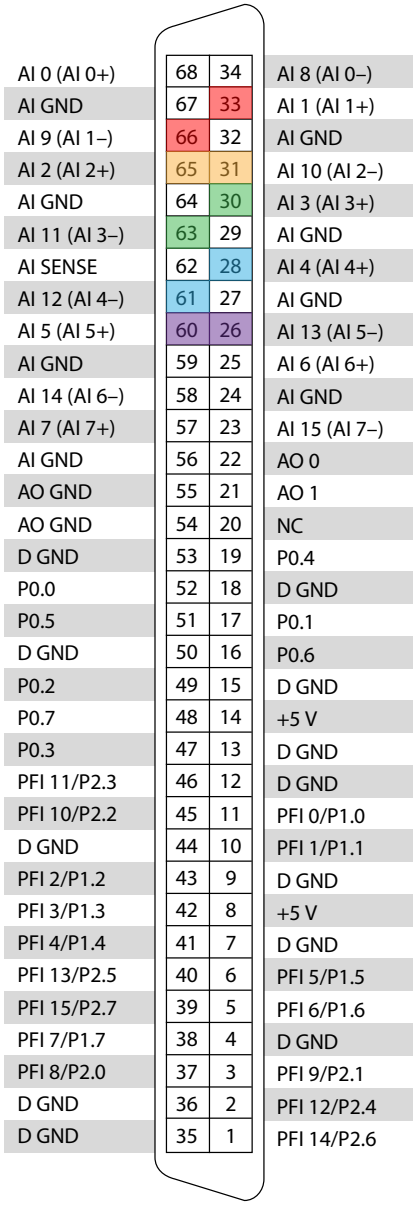

AI 0 (AI 0+)	68	34	AI 8 (AI 0–)
AI GND	67	33	AI 1 (AI 1+)
AI 9 (AI 1–)	66	32	AI GND
AI 2 (AI 2+)	65	31	AI 10 (AI 2–)
AI GND	64	30	AI 3 (AI 3+)
AI 11 (AI 3–)	63	29	AI GND
AI SENSE	62	28	AI 4 (AI 4+)
AI 12 (AI 4–)	61	27	AI GND
AI 5 (AI 5+)	60	26	AI 13 (AI 5–)
AI GND	59	25	AI 6 (AI 6+)
AI 14 (AI 6–)	58	24	AI GND
AI 7 (AI 7+)	57	23	AI 15 (AI 7–)
AI GND	56	22	AO 0
AO GND	55	21	AO 1
AO GND	54	20	NC
D GND	53	19	P0.4
P0.0	52	18	D GND
P0.5	51	17	P0.1
D GND	50	16	P0.6
P0.2	49	15	D GND
P0.7	48	14	+5 V
P0.3	47	13	D GND
PFI 11/P2.3	46	12	D GND
PFI 10/P2.2	45	11	PFI 0/P1.0
D GND	44	10	PFI 1/P1.1
PFI 2/P1.2	43	9	D GND
PFI 3/P1.3	42	8	+5 V
PFI 4/P1.4	41	7	D GND
PFI 13/P2.5	40	6	PFI 5/P1.5
PFI 15/P2.7	39	5	PFI 6/P1.6
PFI 7/P1.7	38	4	D GND
PFI 8/P2.0	37	3	PFI 9/P2.1
D GND	36	2	PFI 12/P2.4
D GND	35	1	PFI 14/P2.6

Differential configuration
wiring diagram

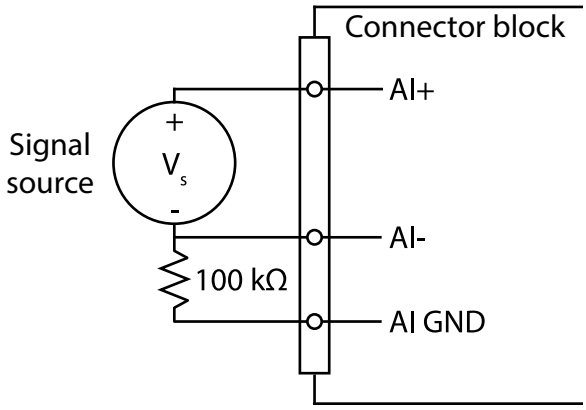

The `FlowTube_Megastation.vi` program uses hardware-timed single point (HWTSP) acquisition to synchronize AI signal collection with the firing of the lasers. A series of three daisy-chained digital delay generators (Stanford Research Systems, DG535) operate with the same 20-Hz trigger to provide TTL pulses to the Nd:YAG lasers, the boxcar averager, and the DAQ card before a subsequent trigger arrives. Figure 4.11 depicts this wiring scheme. The TTL pulses to the lasers establish the time delay between the lamps and the Q-switch, which we keep optimized at 180 μs for most experiments. The same TTL pulses also determine the delay between the firing of the two Nd:YAG lasers, which varies based on the distance between the lasers along the length of the flow tube and the flow conditions we choose. The TTL pulse to the DAQ card is a DI wired to a programmable function interface (PFI) terminal on the connector block. This DI triggers the HWTSP acquisition in LabView, ensuring that each AI sample is associated with exactly one laser shot. The timing for the shutter is controlled by a DO from the DAQ card ($P_{0.0}$) synchronized with the HWTSP data acquisition in LabView.

The primary LabView program we use, `FlowTube_Megastation.vi`, communicates with the DAQ card, the stepper motors, and the wavemeter simultaneously. It also logs the data and automatically tags it with a time stamp and a tag chosen by the user on the front end. Figure 4.13 shows the front end of the VI where the user sets the parameters for the experiment. In addition to choosing a tag for the data, the user controls which AI signals the VI reads in, and which settings to use for controlling the shutter and dye laser scanning. The front end displays raw AI data plotted versus time during data collection, but the VI also saves `.txt` files in which the data is binned by shutter state (open or closed) and by step (when scanning the dye laser wavelength). Here, a "step" refers to the period in which

Figure 4.13: Labview front end for the `FlowTube_Megastation.vi` code. Here, the user selects a number of parameters for the experiment prior to running the VI, including which AIs are in use, shutter settings, wavelength scan settings, and saving settings. The front end displays plots of the raw AI data versus time as data is collected. It also displays flow characteristics (speed and Reynolds number) when the differential and static manometers are both in use.

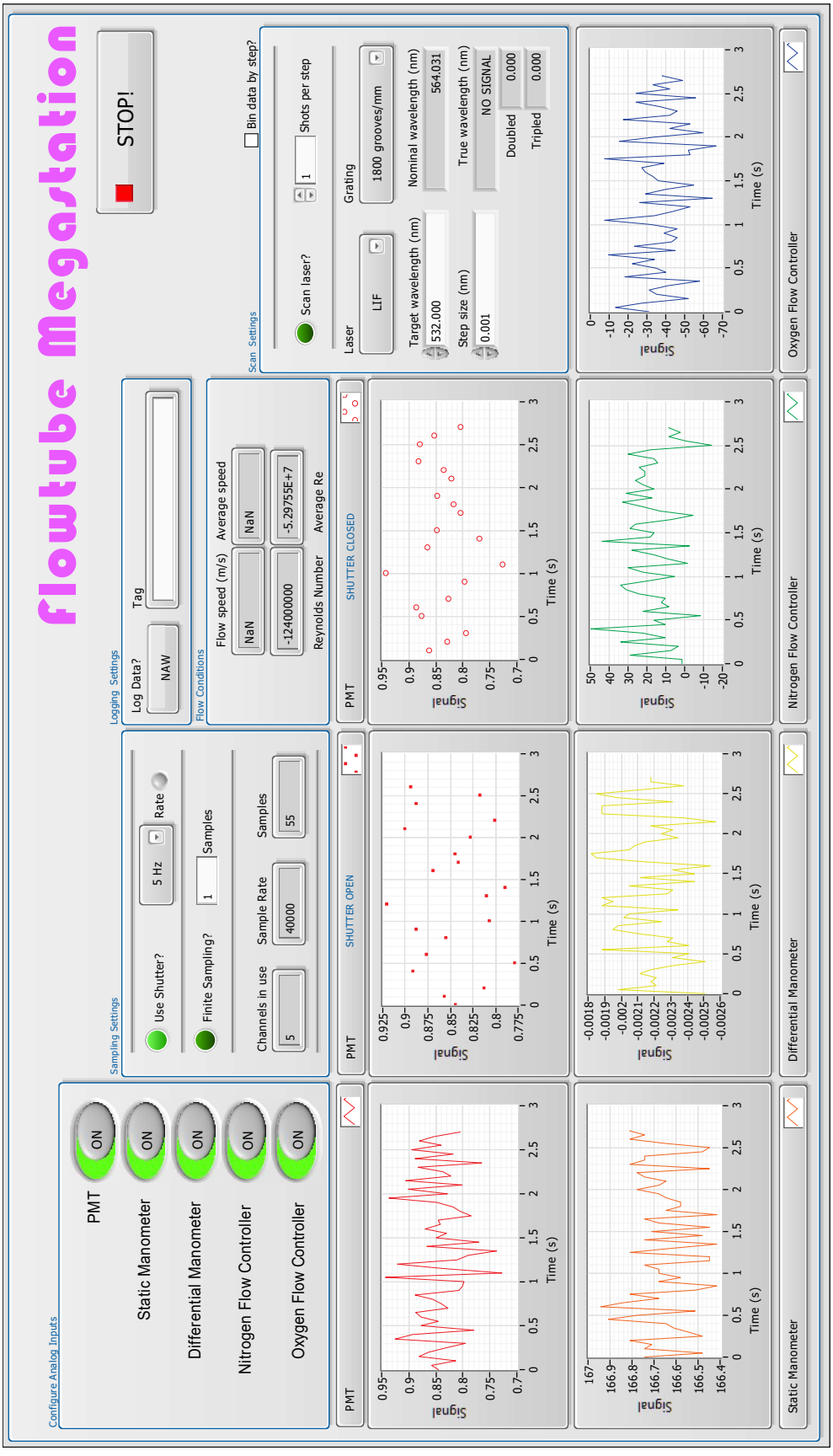
Flowtube Megastation
STOP!
Configure Analog Inputs
PMT
Static Manometer
Differential Manometer
Nitrogen Flow Controller
Oxygen Flow Controller
ON
Sampling Settings
Use Shutter?
5 Hz
Rate
Finite Sampling?
1
Samples
Channels in use
5
Sample Rate
40000
Samples
55
Logging Settings
Log Data?
NAW
Tag
Flow Conditions
Flow speed (m/s)
NaN
Average speed
NaN
Reynolds Number
-124000000
Average Re
-5.29755E+7
Scan Settings
Bin data by step?
Scan laser?
1
Shots per step
Laser
LIF
Grating
1800 grooves/mm
Target wavelength (nm)
532.000
Nominal wavelength (nm)
564.031
Step size (nm)
0.001
True wavelength (nm)
NO SIGNAL
Doubled
0.000
Tripled
0.000
PMT
SHUTTER OPEN
SHUTTER CLOSED
Static Manometer
Differential Manometer
Nitrogen Flow Controller
Oxygen Flow Controller
Signal
Time (s)

the dye laser stepper motor is stationary during a scan. The user indicates on the front end of `FlowTube_Megastation.vi` the number of laser shots taken at each step and the size (in nm) between each step. The program records the wavemeter value and AI sample for each laser shot and averages the values for a given step to produce the binned data. Appendix B details the back-end block diagram and the subVIs for `FlowTube_Megastation.vi`.

4.3 Flow characterization

The general description of the apparatus covered components of the flow tube that measure flow properties such as static pressure, local differential pressure, and flow rate. These measurements are valuable to our kinetics studies insofar as they describe transport between the photolysis region and the LIF region, specifically with regard to timescales for flow development and unimolecular dissociation. The ensuing sections will connect the measurements we make with quantities relevant to transport and kinetics in the flow tube. Section 4.3.1 covers basic fluid dynamics related to flow characterization. Section 4.3.2 then quantifies flow properties under a wide range of conditions and details the accompanying experimental protocols.

4.3.1 Transport and fluid dynamics

The Reynolds number Re

$$Re = \left(\frac{\rho D_H}{\mu}\right)\bar{v} \tag{4.1}$$

is a unitless quantity that characterizes gas flow behavior through a tube with hydraulic diameter D_H, fluid density ρ, dynamic viscosity μ, and bulk flow velocity $\bar{v}$. For a circular

tube, D_H is simply the inner diameter, and for the thermodynamic regimes of studies herein the ideal gas law

$$\rho = \frac{P_s M}{RT} \tag{4.2}$$

approximates ρ well, where P_s, T, and M are the static pressure, temperature, and molar mass of the gas respectively and R is the gas constant. Figure 4.14 depicts the two flow patterns that manifest for small and large values of Re. In general, Re represents competition between viscous forces in the gas due to differing local velocities and inertial forces due to net transport of the gas. For $Re < 1800$, the flow is laminar and viscous forces dominate, giving rise to a parabolic velocity profile and smooth fluid motion. For $Re > 2100$, inertial forces dominate, producing turbulent flow with chaotic fluid motion and a relatively flat velocity profile. A transition range from the laminar regime to turbulent regime typically occurs between $Re = 1800$ and $Re = 2100$.[4]

The hydrodynamic entrance length (Section 4.2.2) differs for laminar and turbulent flows.[5] For a laminar flow, the entrance length L_{lam} is

$$L_{lam} = 0.05 D_H Re \tag{4.3}$$

while for a turbulent flow,

$$L_{turb} = 1.349 D_H (Re)^{1/4} \tag{4.4}$$

where L_{turb} is the turbulent hydrodynamic entrance length. Figure 4.15 summarizes the hydrodynamic entrance lengths of the flow tube for both regimes up to $Re = 6000$. The figure shows that in general, turbulent conditions achieve uniform flow considerably faster than most laminar conditions. In the long-flow configuration, Reynold's numbers below

Figure 4.14: Laminar and turbulent velocity profiles in flow through a pipe. Below $Re = 1800$ the flow is laminar and smooth with a parabolic velocity profile, abover $Re = 2100$ the flow becomes turbulent and chaotic with a flat velocity profile.

Laminar regime

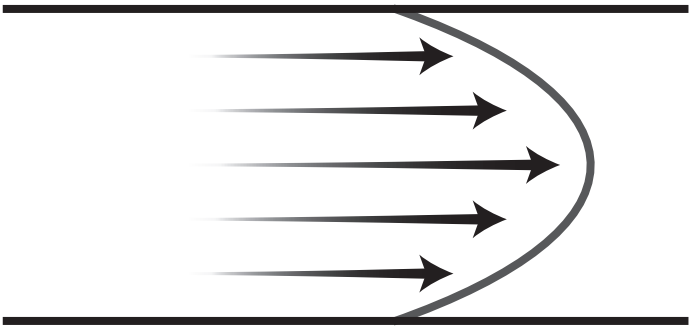

$Re < 1800$

Turbulent regime

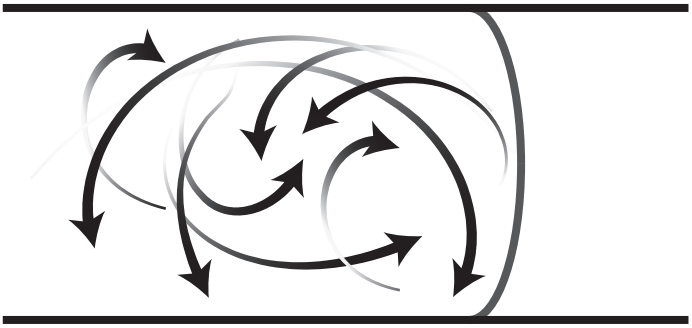

$Re > 2100$

Figure 4.15: Hydrodynamic entrance lengths for laminar (red) and turbulent (blue) flow conditions. The dashed lines show the length necessary to achieve uniform flow prior to the photolysis region in the short- and long-flow configurations of the flow tube.

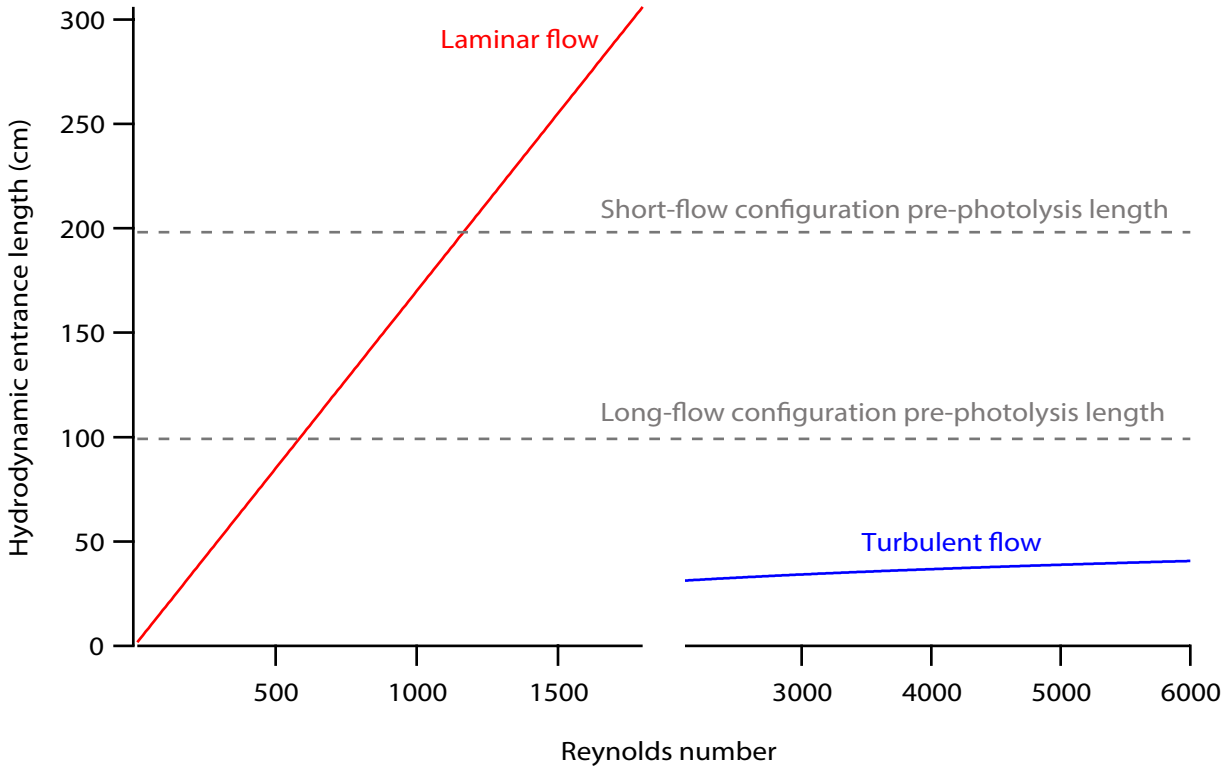
Laminar flow
Short-flow configuration pre-photolysis length
Long-flow configuration pre-photolysis length
Turbulent flow
Hydrodynamic entrance length (cm)
300
250
200
150
100
50
0
500
1000
1500
3000
4000
5000
6000
Reynolds number

500 should establish uniform flow prior to photolysis, while the short-flow configuration can develop uniform flow up to $Re = 1200$.

Figure 4.15 makes clear the need to measure Re in order to ensure that uniform flow is established prior to photolysis. The bulk flow velocity in Equation 4.1 is simply the flow rate Q through the pipe cross section A. That is,

$$\begin{aligned} \bar{v} &= \frac{Q}{A} \\ &= \frac{4Q}{\pi(D_H)^2} \end{aligned} \tag{4.5}$$

where Q is the flow rate at the temperature and pressure in the flow tube. The flow rate we measure with the MFCs is calibrated for standard temperature (273 K) and pressure (760 Torr). Therefore, we convert the flow rate in Equation 4.5 to

$$Q = Q_0 \left(\frac{T}{P_s}\right)\left(\frac{P_0}{T_0}\right) \tag{4.6}$$

where Q_0 is the flow rate measured by the MFCs, and T_0 and P_0 are standard temperature and pressure, respectively. By substitution with Equation 4.1,

$$\begin{aligned} Re &= \left(\frac{\rho D_H}{\mu}\right)\frac{Q}{\left(\pi\left(D_H/2\right)^2\right)} \\ &= \left(\frac{4P_sM}{\pi\mu D_H RT}\right)\left[Q_0\left(\frac{T}{P_s}\right)\left(\frac{P_0}{T_0}\right)\right] \\ &= Q_0\left(\frac{4MP_0}{\pi\mu D_H RT_0}\right) \end{aligned} \tag{4.7}$$

we arrive at an expression for Re in terms of measured flow rate Q_0. For our apparatus, equation 4.7 establishes a useful relationship for characterizing the flow regime, as we measure Q_0 with the MFCs and the remaining variables are held constant.

With the Reynolds number in hand, we know the nature of the flow (laminar or turbulent) and the hydrodynamic entrance length. The next characteristic we desire is the transport

time between the photolysis region and the LIF region, which requires knowledge of the flow velocity. The bulk flow velocity is given by Equation 4.5, but we can also measure local, radially-resolved velocities with the use of the pitot-static tube. The local velocity measured by the pitot-static tube is derived from Bernoulli's equation. Dynamic pressure P_d is defined as

$$P_d = \frac{1}{2}\rho v^2 \tag{4.8}$$

where v is the gas velocity. Bernoulli's equation states that total pressure is the sum of static and dynamic pressures. That is,

$$P_t = P_s + \frac{1}{2}\rho v^2 \tag{4.9}$$

where P_t is the total pressure. The pitot-static tube measures P_{diff}, the difference between the total pressure and the static pressure. Solving for v

$$v = \sqrt{\frac{2P_{diff}}{\rho}} \tag{4.10}$$

yields an expression for the local velocity the pitot-static tube measures. By varying the height of the pitot-static tube, we generate radially-resolved velocity profiles.

4.3.2 Flow measurements and analysis

Figure 4.16 shows the flow rates necessary for our appartus to achieve laminar or turbulent conditions as predicted by Equation 4.7. Previous studies have successfully characterized kinetics in both laminar[6] and turbulent[7,8] regimes. In addition to the shorter hydrodynamic entrance length, the use of a turbulent flow is advantageous for generating thorough mixing and avoiding chemical wall-loss. The latter phenomenon is due to a thin laminar sublayer that exists near the wall and forms a no-slip boundary with the otherwise turbulent flow.[9]

Figure 4.16: Plot of Reynolds number as a function of flow rate at standard temperature and pressure for the flow tube apparatus, as calculated by Equation 4.7. Blue and red shading indicates the laminar and turbulent flow regimes, respectively. We show the transition region between the two regimes in purple. The dashed line indicates the region of the laminar regime we can generate with the MFCs that deliver a maximum of 30 SLM.

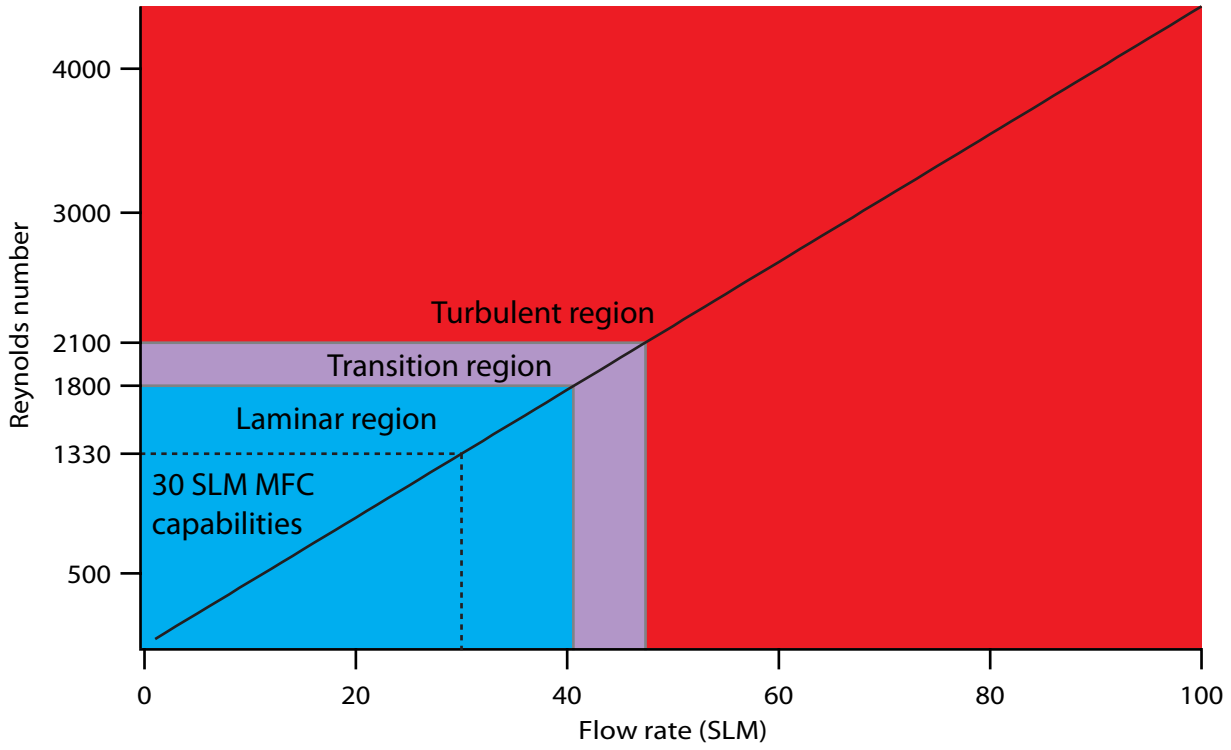
4000
3000
2100
1800
1330
500
Reynolds number
Turbulent region
Transition region
Laminar region
30 SLM MFC
capabilities
0
20
40
60
80
100
Flow rate (SLM)

However, the substantial flow rates necessary to achieve turbulence necessitate a tremendous amount of gas, and thorough mixing is not necessary for the one-step unimolecular photodissociations we use to characterize the flow tube. Thus, we resort to laminar flows generated by our 30 SLM MFCs in the majority of the characterization we do.

We begin characterization with pitot-static measurements taken in the long-flow configuration of the flow tube. Measurements with the pitot-static tube serve two purposes: (1) they verify the radial velocity profile predicted by the Reynolds number (Figure 4.14), and (2) they put a lower bound on transport time between the photolysis region and the LIF region. The lower bound for the transport time is found by measuring the maximum local velocity (which should occur in the center of the flow tube). The transport time t is then given by

$$\begin{aligned} t &= \frac{z}{v} \\ &= \sqrt{\frac{\rho z^2}{2P_{diff}}} \end{aligned} \tag{4.11}$$

where z is the distance from the photolysis beam to the LIF beam along the length of the flow tube. The bulk flow transport time $\bar{t}$ is given by

$$\begin{aligned} \bar{t} &= \frac{\pi z (D_H)^2}{4Q} \\ &= \left(\frac{\pi z T_0 (D_H)^2}{4TP_0}\right)\left(\frac{P_s}{Q_0}\right) \end{aligned} \tag{4.12}$$

and depends on both the pressure and the flow rate for a given transport distance z. Thus, we can modulate the time available for chemical reactions in the flow tube in a quantifiable manner by changing the pressure, the flow rate, or the window used for photolysis. The vacuum controller can maintain constant pressure (whereby the flow rate varies to maintain the set point) or constant flow rate (whereby the pressure equilibrates at a given flow rate

enforced by the controller). If we set the flow rate of the MFCs with the vacuum controller, we throttle the flow with the diaphragm valve on the vacuum foreline to obtain the pressure we desire. Alternatively, with a pressure set point on the vacuum controller, throttling the flow with the diaphragm valve tunes the flow rate. We have found the latter method is more convenient for generating the constant pressures and flow rates we desire. The vacuum controller uses proportional-integral-derivative (PID) control to maintain a pressure set point. Appendix C covers the aspects of the PID recipe and the parameters we typically employ.

Figure 4.17 demonstrates the breadth of radial velocity profiles we can generate in the laminar regime, as measured by the pitot-static tube. We find the midpoint of the 34-mm ID flow tube by zeroing the height gauge with the pitot-static tube abutting the bottom of the flow tube and moving it up by 17 mm. We typically generate local velocity measurements every 3 mm radially. The radius of curvature for the pitot-static tube prevents it from reaching the topmost portion of the flow tube. In the laminar regime, we can reach flow speeds as fast as 70 ms^{-1} or as slow as 1 ms^{-1} and still discern parabolic velocity profiles. Equivalently, we can generate a range of transport times between the photolysis region and the LIF region in the laminar regime simply by tuning the flow rate and the pressure. Figure 4.18 uses the data in Figure 4.17 to demonstrate the range of transport times we can achieve in the long-flow configuration of the flow tube. We confirm with our radially-resolved measurements that the peak flow velocity occurs in the center of the flow tube, and we use this measurement to derive the flow times on the left side of Figure 4.18. Bulk flow velocity measurements generate the flow times on the right of the figure. The spread of flow times for each pressure region we measured is due to the difference in transport time between

Figure 4.17: Radial flow velocity profiles at various pressures in the laminar regime. The top and bottom plots are of the same data set. The top plots group profiles by pressure while the bottom plots group profiles by Reynolds number. The differential pressure was below the sensitivity of the pitot-static tube at $Re = 300$ and 900 for 100 and 300 Torr measurements.

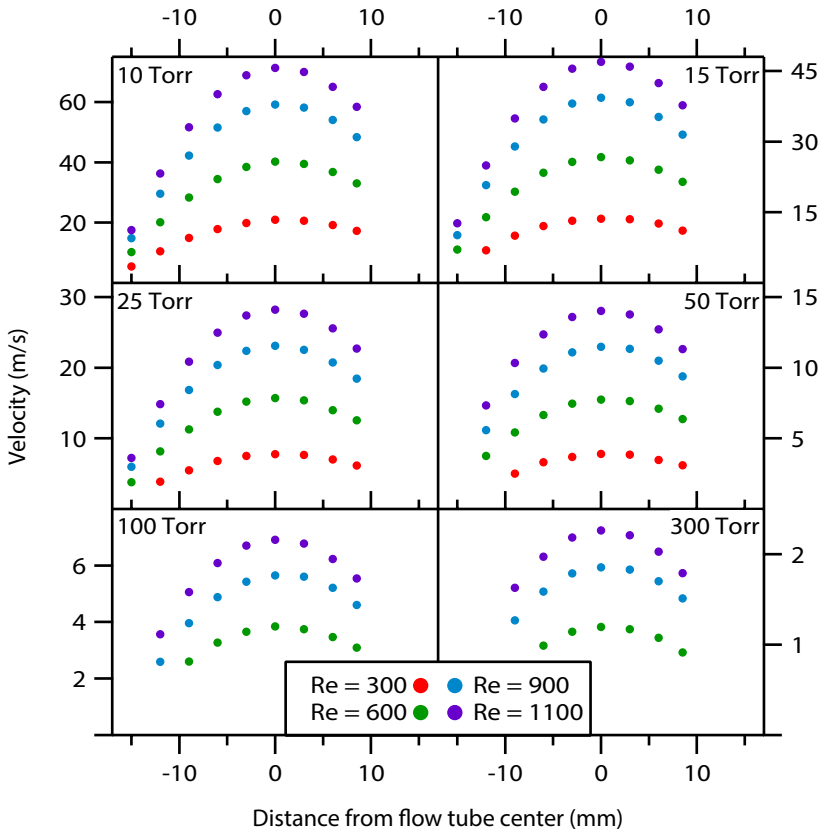
10 Torr
15 Torr
25 Torr
50 Torr
100 Torr
300 Torr
Re = 300
Re = 600
Re = 900
Re = 1100
Velocity (m/s)
Distance from flow tube center (mm)

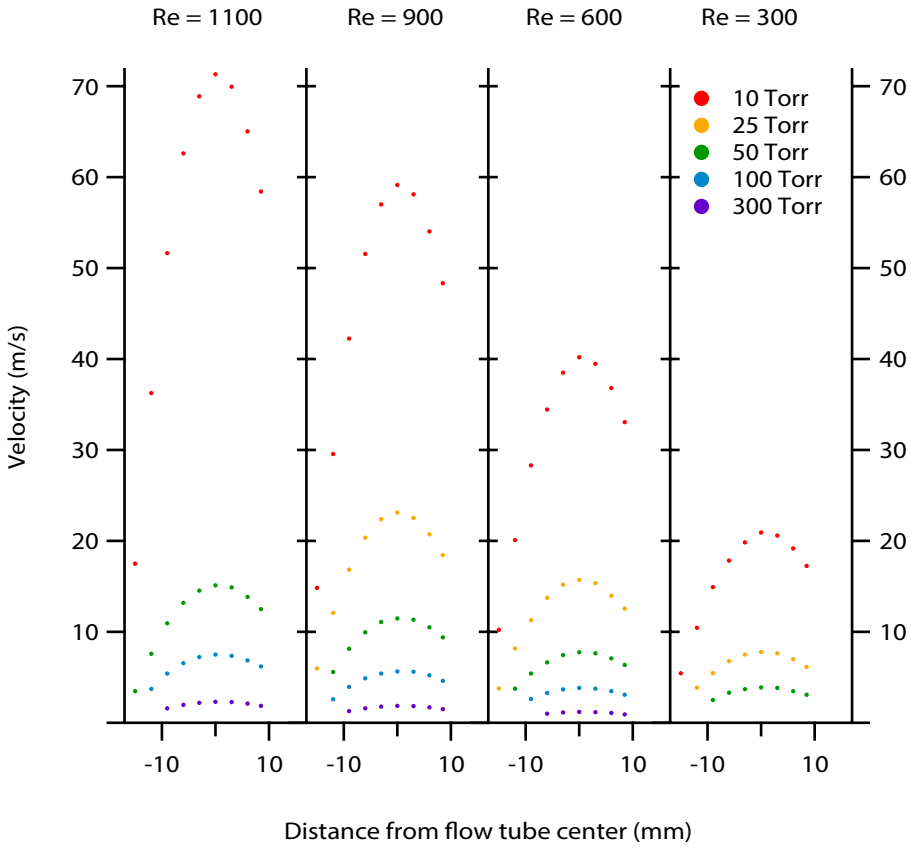
Re = 1100
Re = 900
Re = 600
Re = 300
10 Torr
25 Torr
50 Torr
100 Torr
300 Torr
Velocity (m/s)
Distance from flow tube center (mm)

Figure 4.18: Measured flow times for the apparatus in the long flow configuration versus Reynolds number at various pressures. Calculations using the peak velocity in the flow (at the center of the flow tube) generate the flow times on the left. Calculations using the bulk flow velocity generate the flow times on the right. The span each pressure covers at a given Reynolds number is the difference in flow time between the front and back windows in the photolysis region. We measure the velocities used to determine flow times with the pitot-static tube.

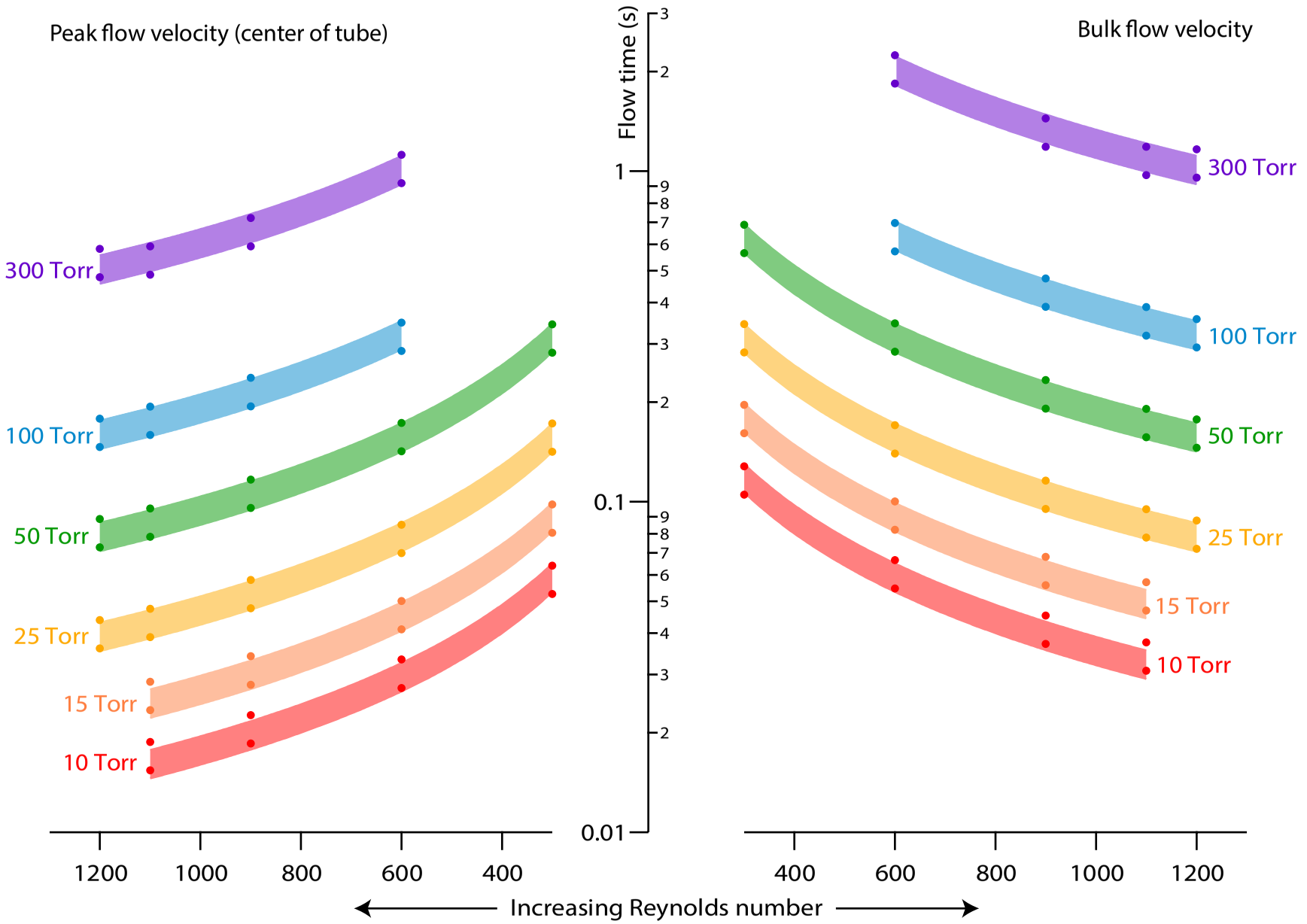
Peak flow velocity (center of tube)
Bulk flow velocity
Flow time (s)
3
2
1
9
8
7
6
5
4
3
2
0.1
9
8
7
6
5
4
3
2
0.01
300 Torr
100 Torr
50 Torr
25 Torr
15 Torr
10 Torr
1200
1000
800
600
400
400
600
800
1000
1200
Increasing Reynolds number

the front and back windows of the photolysis region. The figure shows that the long-flow configuration of the flow tube has the potential to facilitate unimolecular processes with timescales of roughly 0.01–1 s in the laminar regime. Of course, shorter timescales could be studied in the short-flow configuration or the turbulent regime.

We briefly employed the 200 SLM MFM to ensure we could generate turbulent profiles. Because the MFM measures the flow rate rather than controlling it, we cannot produce data as systematically as we did to construct Figure 4.17. Nonetheless, we measure a distinctly turbulent velocity profile at $Re = 4400$. Figure 4.19 plots the turbulent profile with a laminar profile at $Re = 970$. The turbulent profile is at 28.7 Torr and 100 SLM while the laminar profile is at 22 SLM and 19.8 Torr. To assess the shape of the profiles on the same scale, the local flow velocities in each profile were divided by the bulk flow velocity given by equation 4.5. These measurements are the extent of the turbulent flow characterization we performed, but in the future the 250 SLM MFC will provide a more comprehensive characterization of the turbulent flows we can generate with our apparatus. Determining which flow regime is ideal for the unimolecular kinetics studies we propose is not trivial and may depend on the system of interest, but we have demonstrated that our apparatus is capable of flow characterization in either regime over a wide range of pressures.

4.4 OH detection

We use nitric acid photolysis in the flow tube as an OH source to test the functionality of the LIF detection region and assess in-flow detection capabilities. Nitric acid absorbs strongly below 340 nm, leading to NO_2 and OH products.[10] We have successfully employed two LIF

Figure 4.19: Radial velocity profiles in the laminar (blue) and turbulent (red) regime. We divide the local velocities v by the bulk velocity $\bar{v}$ (calculated with Equation 4.5) for each regime to emphasize the shape of the two profiles on a common scale.

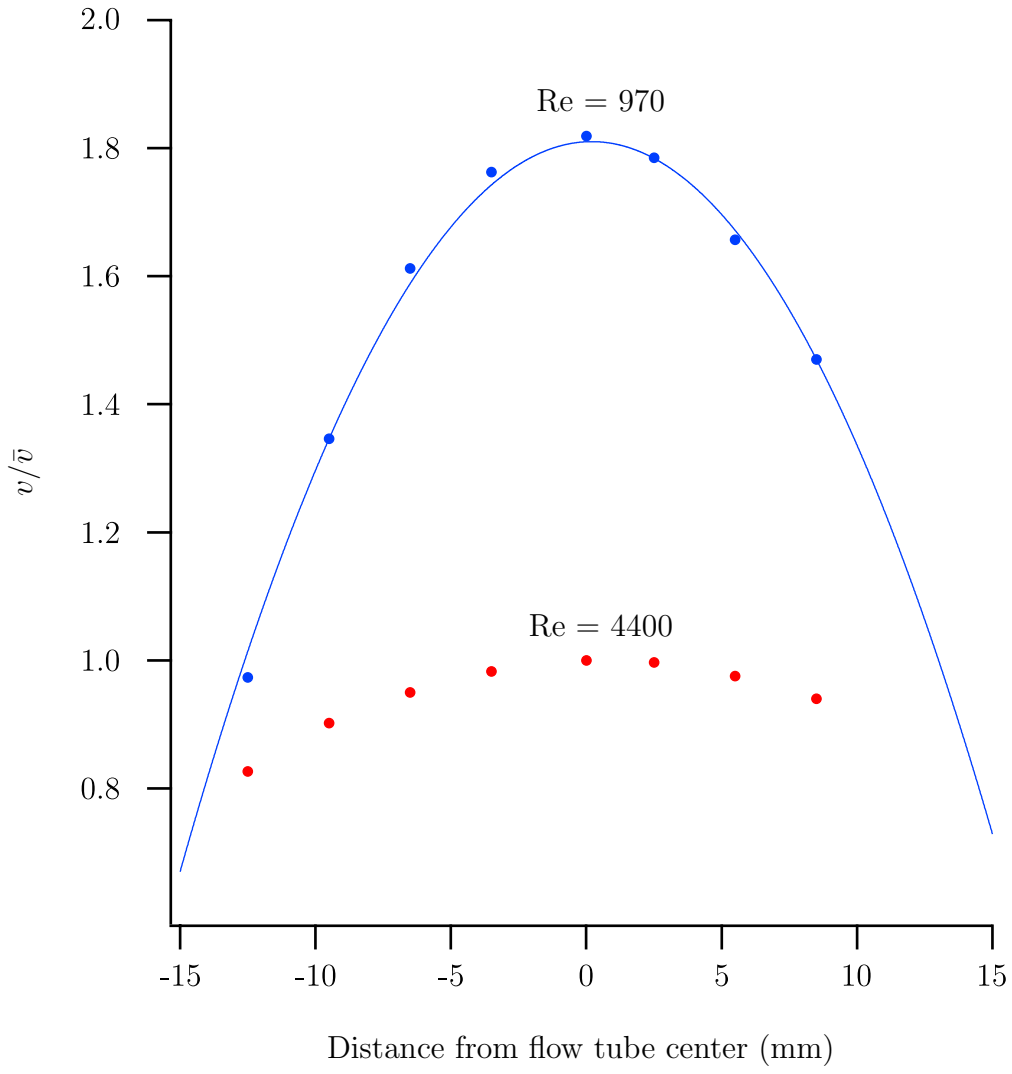
2.0
1.8
1.6
1.4
1.2
1.0
0.8
$v/\bar{v}$
Re = 970
Re = 4400
-15
-10
-5
0
5
10
15
Distance from flow tube center (mm)

schemes for OH detection, both of which utilize the $A^2\Sigma^+ \leftarrow X^2\Pi$ electronic excitation. Excitation at 308 nm excites OH radicals electronically but not vibrationally, so the ensuing fluorescence is at the same wavelength as the laser pulse. This can be problematic for detection, since the fluorescence signal cannot be optically filtered from the scattered laser light. Alternatively, $v = 0 \rightarrow v = 1$ vibrational excitation accompanies electronic excitation at 282 nm, and vibrational relaxation in the excited electronic state leads to fluorescent emission at 308 nm. Thus, by filtering the 282-nm laser light in the PMT assembly, we selectively detect the fluorescence signal. This filtering is achieved by the bandpass filters indicated in Figure 4.7. The filter is rated to pass 14.2% of incident 308-nm light and $< 0.2\%$ of 282-nm light. Although we found LIF signal with both 308- and 282-nm excitation, most of the characterization used the 282-nm scheme, which we found had a better signal to noise ratio and was less susceptible to quenching of the fluorescence at elevated pressure.

4.4.1 Finding LIF signal

Before we look for LIF signal in the flow tube, we ensure the laser is tuned to an OH transition using the flamebox (Section 4.2.6) and compare transitions we identify with the HITRAN database.[11] Our scans typically use a step size of 0.003 nm with 100 laser shots per step, although we average more or less depending on the signal to noise ratio. Figure 4.20 shows a spectrum taken in the flamebox using 282-nm LIF excitation with HITRAN data superimposed. We use the intensity of the LIF transitions we find in the flamebox to choose a transition to look for in the flow tube. The arrow in Figure 4.20 indicates the transition we initially sought in the flow tube at 282 nm. Figure 4.21 shows the same transition in

Figure 4.20: LIF spectrum of OH in the flamebox at 282 nm. The arrow indicates the transition we look for in the flow tube having seen good LIF signal in the flame box in agreement with the HITRAN simulation. The black stick spectrum is the HITRAN data.

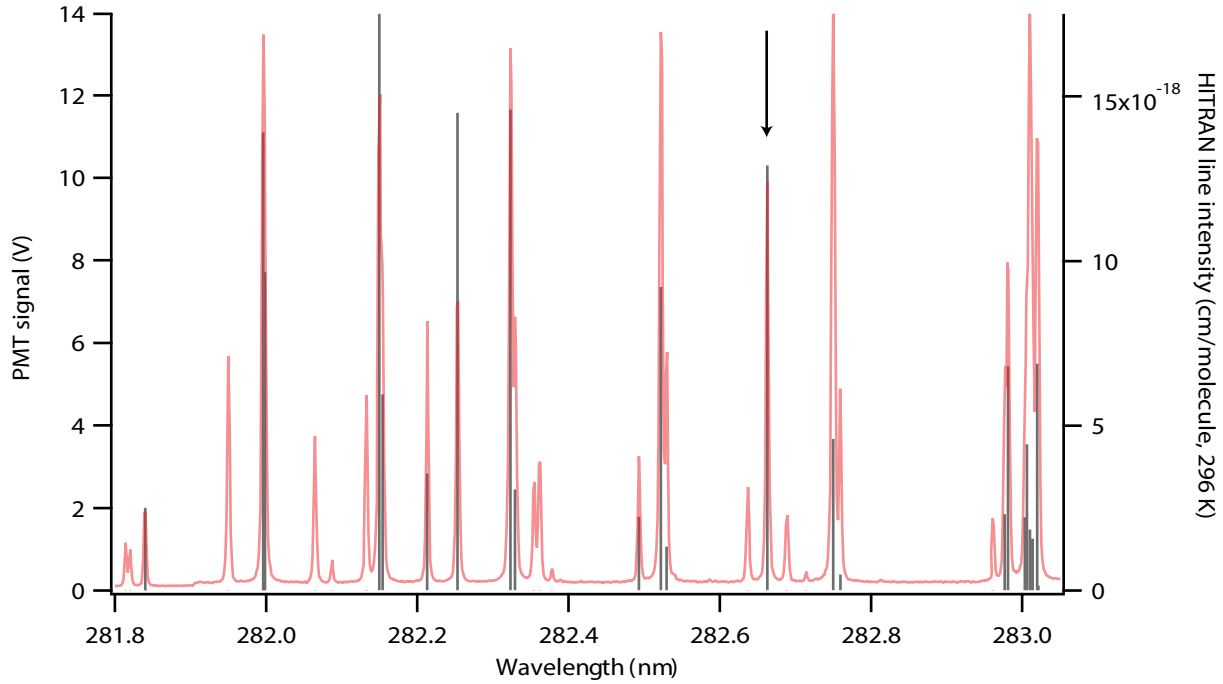
PMT signal (V)
HITRAN line intensity (cm/molecule, 296 K)
15x10^-18
Wavelength (nm)
0
2
4
6
8
10
12
14
5
281.8
282.0
282.2
282.4
282.6
282.8
283.0

Figure 4.21: The top spectrum shows the initial LIF signal of OH we found in the static flowtube at 282 nm. The bottom portion of the figure demonstrates the pressure dependence of the LIF signal in the static flow tube.

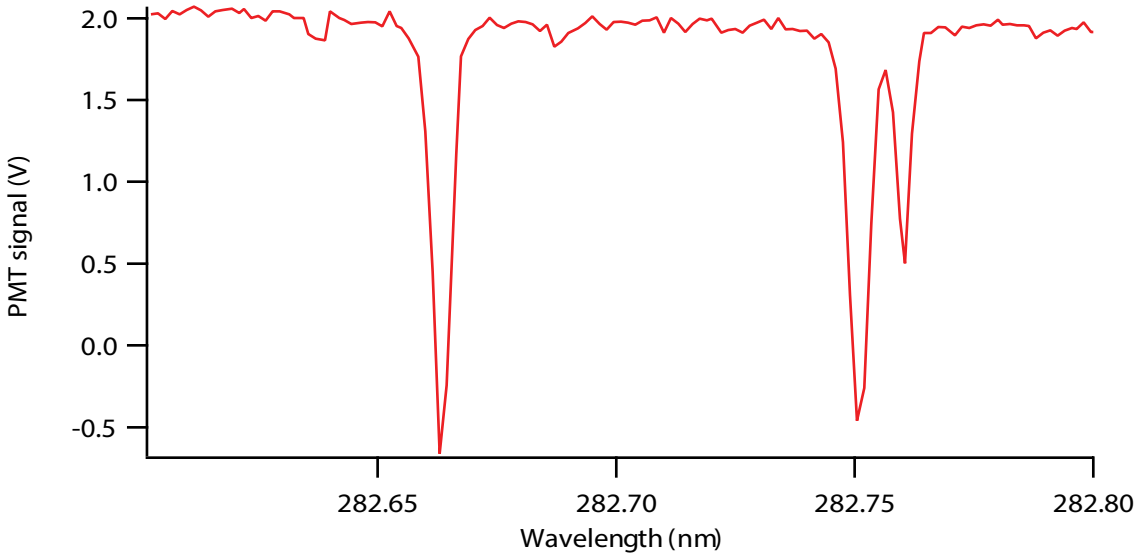
2.0
1.5
1.0
0.5
0.0
-0.5
PMT signal (V)
282.65
282.70
282.75
282.80
Wavelength (nm)

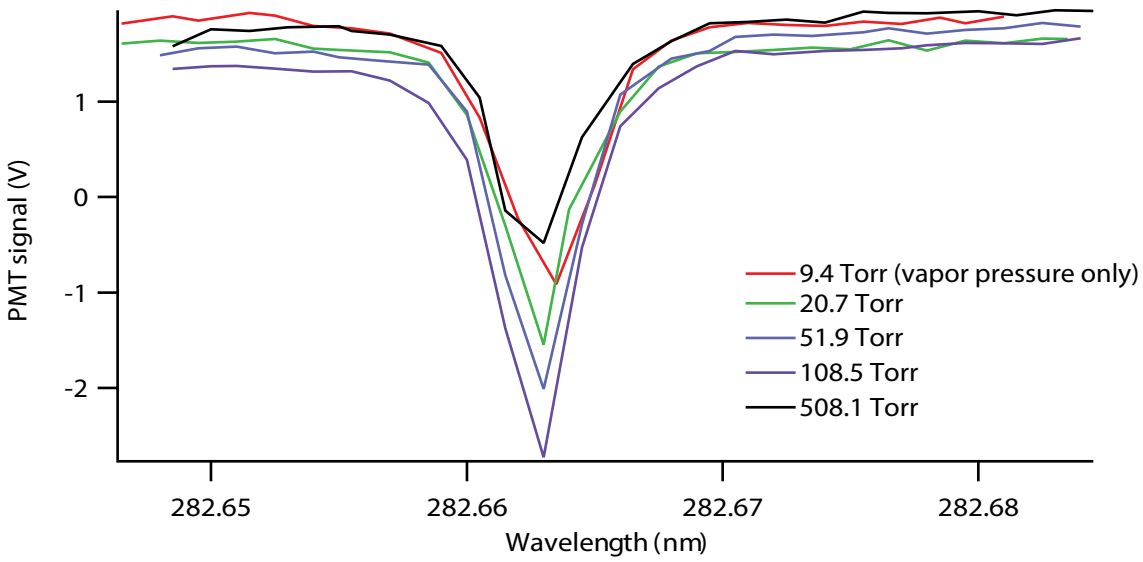
1
0
-1
-2
PMT signal (V)
9.4 Torr (vapor pressure only)
20.7 Torr
51.9 Torr
108.5 Torr
508.1 Torr
282.65
282.66
282.67
282.68
Wavelength (nm)

the flow tube and the pressure dependence of the signal strength. The 70% HNO_3 sample develops 9.4 Torr of vapor pressure, and nitrogen pressurizes the flow tube to achieve the higher pressures shown in the Figure. Demonstrating LIF detection capabilities over a range of pressures is necessary if we wish to utilize the wide range of transport times we measure.

In the flow tube, we find LIF signal initially in a static environment (i.e. without flow) with both lasers aligned through the LIF region. Lens tubes thread into the window ports on each side of the LIF region and support alignment targets to optimize overlap between the two beams. We overlap the beams in time by adjusting the DDGs while monitoring the scattered light signal with the PMT. With the right overlap spatially and temporally, LIF signal manifests as a peak which decays 10s of ns longer than the scattered light pulses. We can then move the photolysis signal a few ns before the LIF pulse, which makes it easier to gate the fluorescence with the boxcar averager without capture scattered photolysis light. The signal is verified by detuning the LIF wavelength and ensuring that it disappears. Figure 4.22 shows traces from the oscilloscope of typical LIF signals. Because the LIF wavelengths we use are readily absorbed by nitric acid, one-color signal is also present. To maximize signal solely due to two-color LIF of OH, we shutter the one-color photolysis-only signal on a shot-to-shot basis and minimize the one-color LIF-only signal by reducing laser power. In this way, we generate difference signal in which one-color contributions are subtracted out.

Even without shuttering the photolysis beam, we found ample LIF signal at 308 nm by scanning the LIF laser. We obtain the top spectrum in Figure 4.23 in this manner. However, switching the LIF wavelength to 282 nm and shuttering the photolysis laser leads to marked improvement in signal to noise ratio, as demonstrated by the bottom spectrum in the figure. With optimized LIF signal in the static flow tube environment using overlapped lasers, we

Figure 4.22: Examples of typical signal the PMT sees from each laser individually and the two-color signal that results when LIF is optimized. Ideally, we subtract the LIF-only signal with shot-to-shot shuttering and minimize the one-color contribution from the photolysis-only signal.

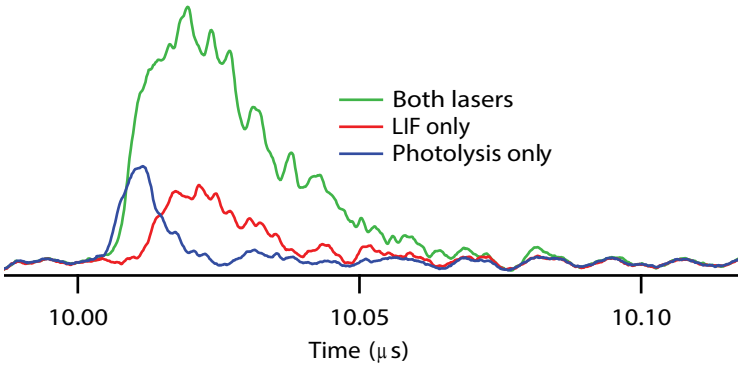
Both lasers
LIF only
Photolysis only
10.00
10.05
10.10
Time (μs)

Figure 4.23: LIF spectra of OH in the static flowtube at 308 and 282 nm. The 308 nm spectrum is a 2-color signal (LIF + photolysis) while the 282 nm spectrum is a difference signal generated with shot-to-shot shuttering on the photolysis leg. Stick spectra (black) are generated by the HITRAN database.[11]

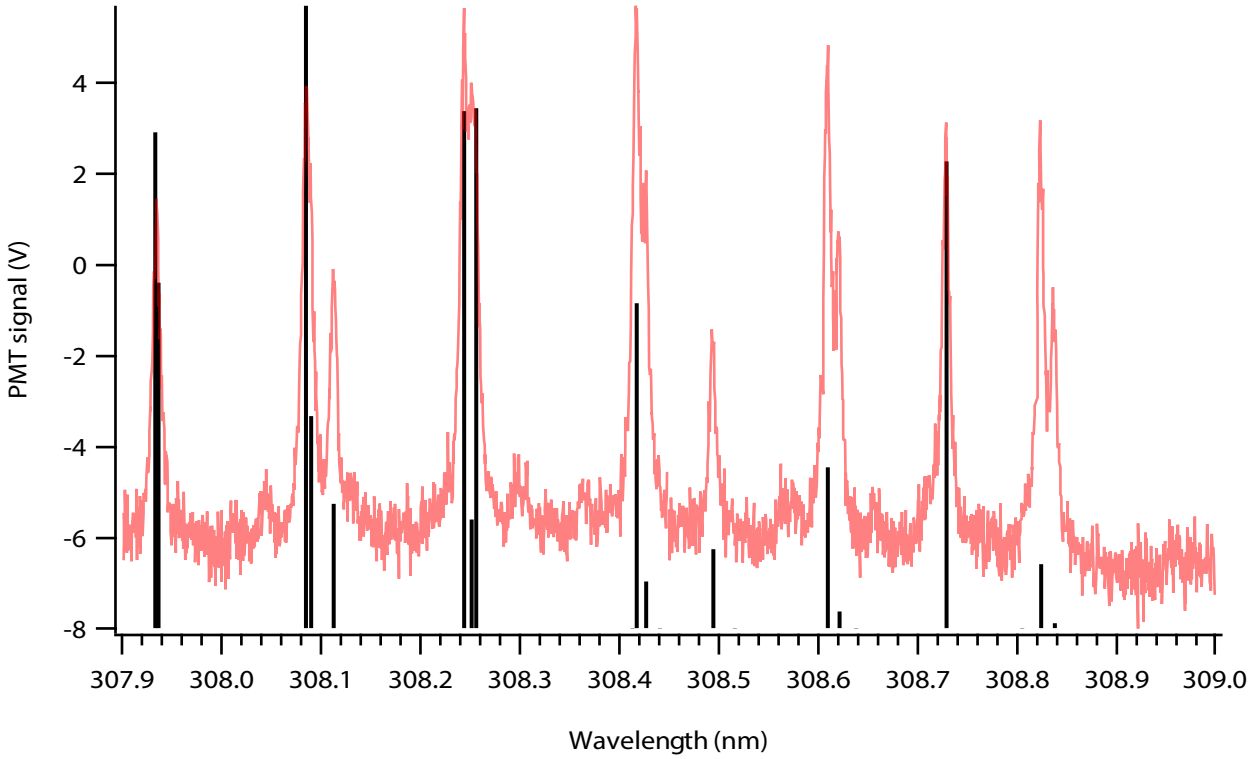
PMT signal (V)
4
2
0
-2
-4
-6
-8
307.9
308.0
308.1
308.2
308.3
308.4
308.5
308.6
308.7
308.8
308.9
309.0
Wavelength (nm)

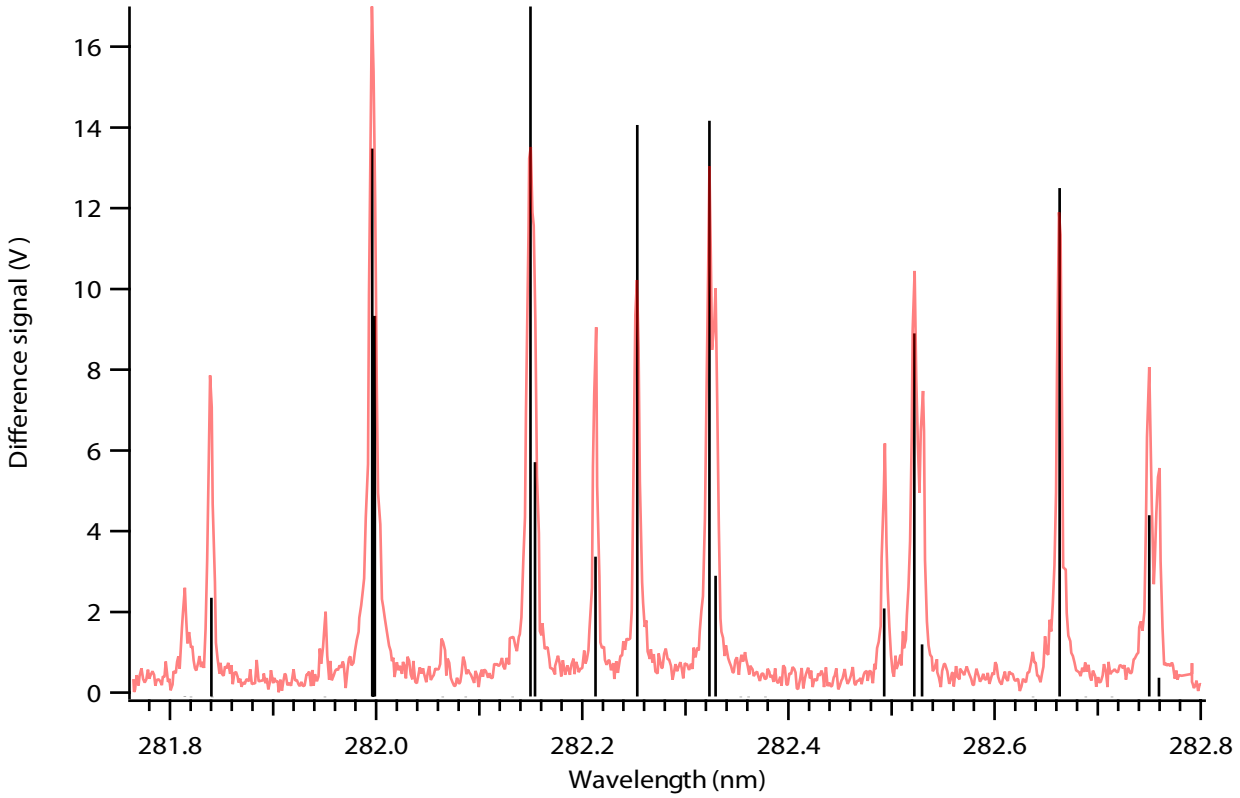
Difference signal (V)
16
14
12
10
8
6
4
2
0
281.8
282.0
282.2
282.4
282.6
282.8
Wavelength (nm)

turn our attention to detecting OH while flowing with the lasers spatially offset.

4.4.2 In-flow detection

Before we separate the lasers spatially and look for LIF of OH transported in the flow, we assess the impact of flow rate on the signal with the lasers overlapped in the LIF region. We find the 70% HNO_3 sample that we keep in the containment has a vapor pressure of ~ 10 Torr. Flowing introduces competition between the rate of evaporation from the sample and the rate of evacuation from the flow tube, which impacts the number density of the nitric acid vapor. Figure 4.24 shows that while higher flow rates indeed hamper LIF signal, we can still detect signal up to at least 5.0 SLM. The figure is generated with PID control at a 10-Torr set point, so that nitrogen is mixed with the nitric acid vapor pressure at whatever flow rate is necessary to maintain the set point. The flow rate is then adjusted by throttling the flow with the diaphragm valve on the vacuum foreline.

Finally, we wish to combine our efforts in characterizing flow properties and LIF detection by photolyzing nitric acid in one region of the flow tube and detecting the OH product in another. The time delay between the photolysis and LIF pulses must be considered carefully. There are 50 ms between the 20-Hz pulses, and each pulse is only ~ 10 ns in duration. The transport time between the photolysis region and the LIF region is not in general a multiple of 50 ms, and therefore we must offset the lasers temporally. Figure 4.25 demonstrates the need for this offset schematically. Moving one laser in time by 10-ns increments would span the range of possible delays. Watching carefully for signal at each step, this process requires five million steps, an arduous task even for a graduate student. Fortunately, this is not

Figure 4.24: Difference signals for OH LIF at 10 Torr and various flow rates. The solid red trace was taken first and the dashed red trace was taken last to check for reproducibility.

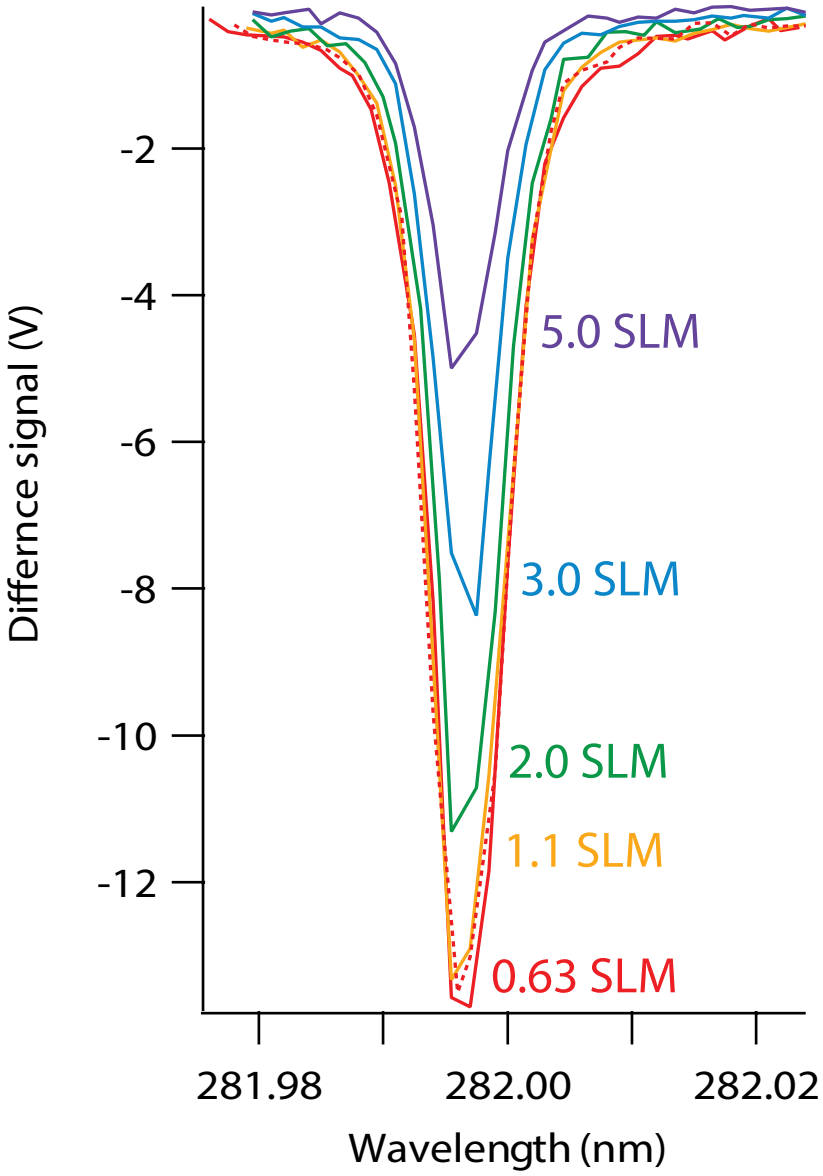
Differnce signal (V)
-2
-4
-6
-8
-10
-12
5.0 SLM
3.0 SLM
2.0 SLM
1.1 SLM
0.63 SLM
281.98
282.00
282.02
Wavelength (nm)

Figure 4.25: Pulse trains for the LIF and photolysis lasers at 20 Hz. An temporal offset of dT between the two lasers accounts for the fact that the transport time from the LIF region to the photolysis region is not necessarily a multiple of the 50 ms delay between pulses. The width of the pulses (~ 10) ns is not to scale.

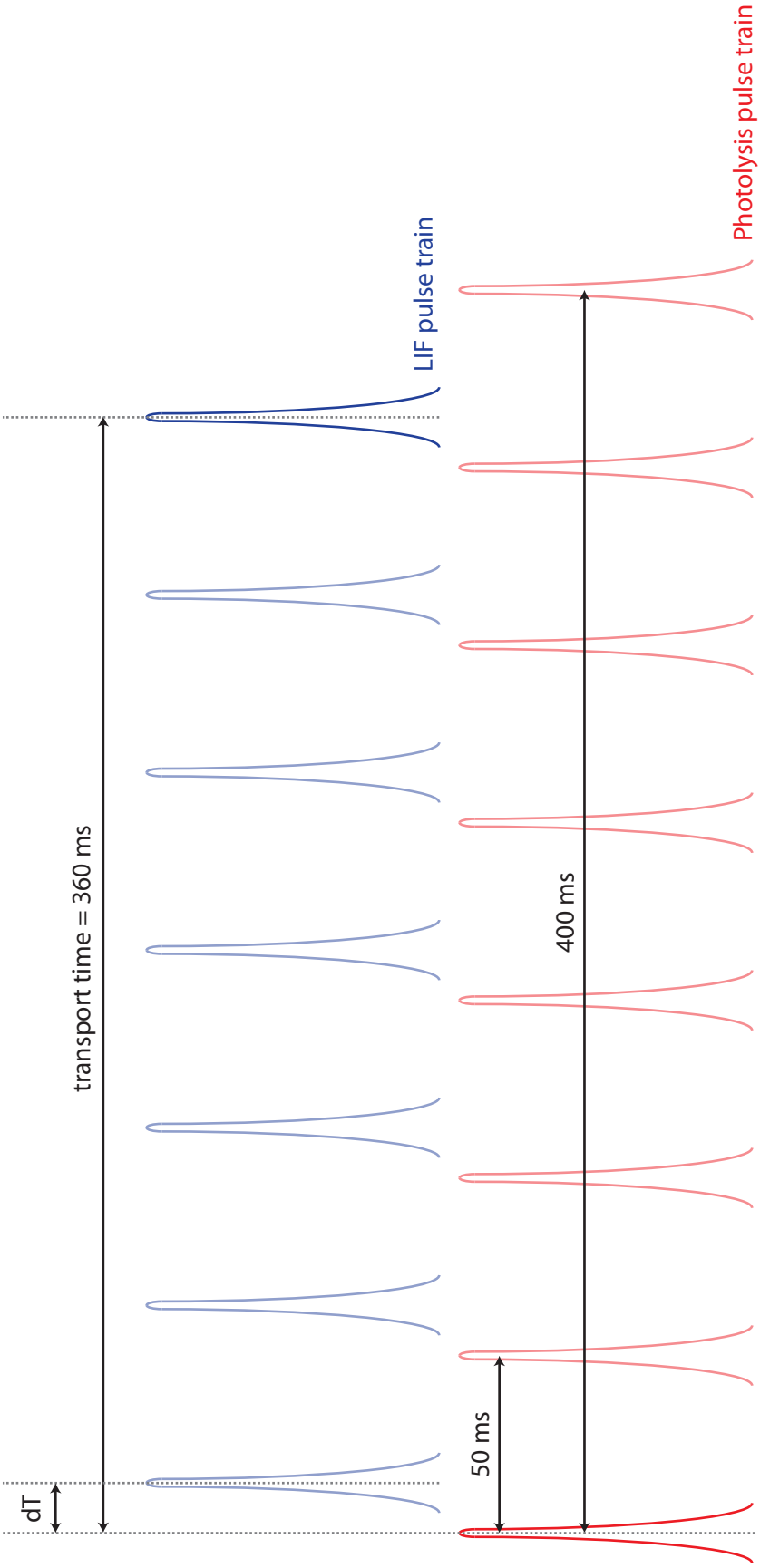
Photolysis pulse train
LIF pulse train
400 ms
50 ms
transport time = 360 ms
dT

necessary. First, we rely on an estimated delay based on the transport times we calculate (as in Figure 4.18) and search for signal near there. Second, the search for signal need not proceed in 10-ns steps, because the width of the OH plume as it travels down the tube is much longer than 10 ns in time. The spot size of the photolysis laser determines the width of the plume at a given pressure and flow rate. We can modify Equation 4.12 to account for the difference in flow time between the front and the back of the photolysis beam waist. That is,

$$\Delta\bar{t} = w\left(\frac{\pi T_0 (D_H)^2}{4TP_0}\right)\left(\frac{P_s}{Q_0}\right) \tag{4.13}$$

where $\Delta\bar{t}$ is the width of the OH plume in time and w is the width of the laser beam. Clearly, a focused beam will create a much narrower plume width than a collimated beam. Figure 4.26 shows OH plume widths calculated with Equation 4.13 using focused and unfocused photolysis light as a function of flow rate. The Figure demonstrates that we can safely take ms-size steps when searching for the proper time delay between the lasers with collimated photolysis light and μs-size steps with focused photlysis light. We have found that in the laminar regime, it is best to use the transport time calculated with the peak flow velocity to estimate the timing for the center of the plume, which suggests we obtain LIF signal primarily from the center of the flow. In cases where we have not used the pitot-static tube to verify the peak flow velocity, a good rule of thumb is to assume the peak flow velocity is twice the bulk flow velocity in the laminar regime.

We found the first signs of in-flow LIF with the lasers separated spatially through the windows of the LIF region. We kept the LIF laser aligned through the center of the windows and moved the photolysis laser backwards along the length of the flow tube. Figure 4.27

Figure 4.26: OH plume widths in the long-flow configuration as a function of flow rate at 10, 20, and 30 Torr. We generate the top plots with Equation 4.13 10-μm beam waist and the bottom plots using 2-mm beam waist.

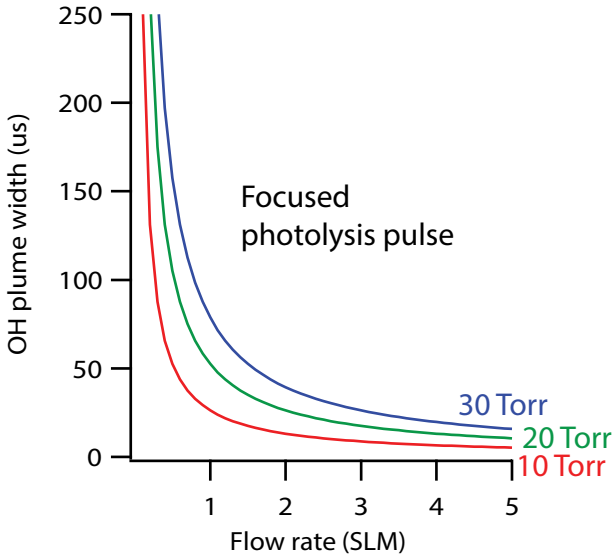
250
200
150
100
50
0
OH plume width (us)
Focused
photolysis pulse
30 Torr
20 Torr
10 Torr
1
2
3
4
5
Flow rate (SLM)

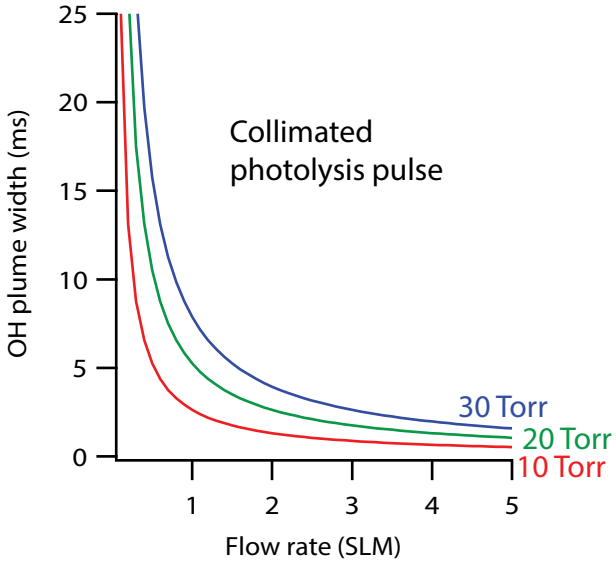
25
20
15
10
5
0
OH plume width (ms)
Collimated
photolysis pulse
30 Torr
20 Torr
10 Torr
1
2
3
4
5
Flow rate (SLM)

Figure 4.27: LIF signals with the photolysis laser separated from the LIF laser by 7 mm. Both laser are aligned through the photolysis region. We took the three difference signals in the figure at different flow rates and adjusted the time delay (dT) between the lasers accordingly to maximize signal.

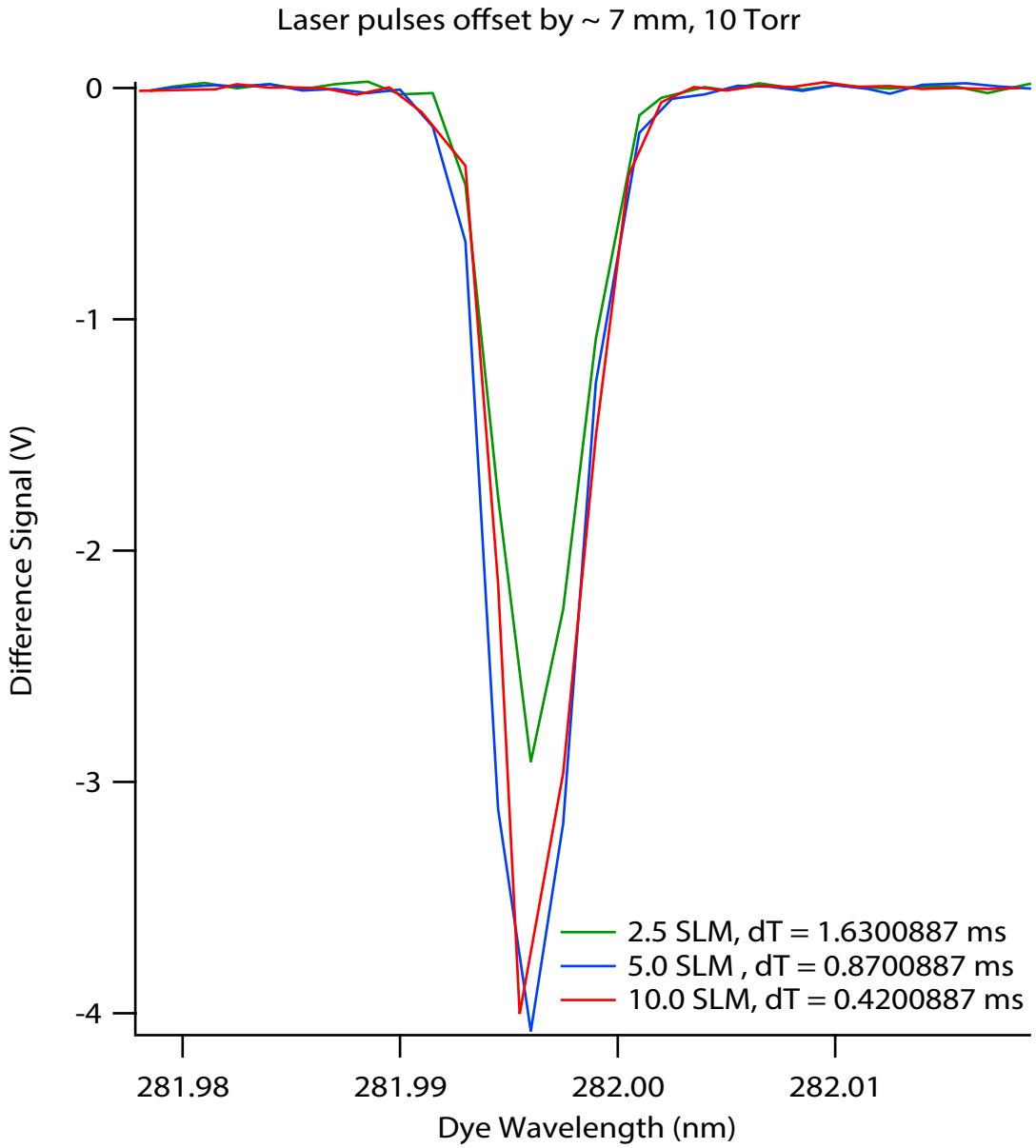
Laser pulses offset by ~ 7 mm, 10 Torr
0
-1
-2
-3
-4
Difference Signal (V)
281.98
281.99
282.00
282.01
Dye Wavelength (nm)
2.5 SLM, dT = 1.6300887 ms
5.0 SLM , dT = 0.8700887 ms
10.0 SLM, dT = 0.4200887 ms

shows LIF signal in 10 Torr flows at various flow rates with ~ 7 mm of separation between the laser beams. The different flow rates lead to different transport times, and we tune the delay between the lasers (dT) accordingly to maximize signal. The smaller signal at 2.5 SLM may be due to diffusion or wall loss, since the transport time is longer than the 5.0 and 10.0 SLM signals.

Next, we extend the transport length from photolysis to LIF by employing the short-flow configuration of the flow tube (Figure 4.1). Starting with the window closest to the LIF region, we optimized signal one window at a time, getting progressively further from the LIF region. When the photolysis beam is aligned through the closest window in the short-flow configuration, we measure a separation of 104 mm from the LIF laser. At the furthest window, the separation is 342 mm. Figure 4.28 demonstrates successful detection of OH following nitric acid photolysis in the windows closest and furthest from the LIF region. To date, this is the furthest distance we have found conclusive in-flow detection. This may be due to the lifetime of OH in the flow tube, and unimolecular processes that do not lead immediately to OH (for instance due to stabilized intermediates or slow isomerization kinetics) may be amenable to longer transport times. Moreover, our characterization of in-flow nitric acid photolysis is not exhaustive. It is possible that modifications to the protocols described here, such as in-flow detection of turbulent flows or a multipass photolysis pulse, could extend the transport times we are able to reliably detect.

Figure 4.28: OH LIF signals in the short-flow configuration of the flow tube. The red signal initiates nitric acid photolysis the window closest to the LIF region, the blue signal initiates photolysis in the window furthest from the LIF region. We take both signals at 10 Torr with a 20 SLM flow rate.

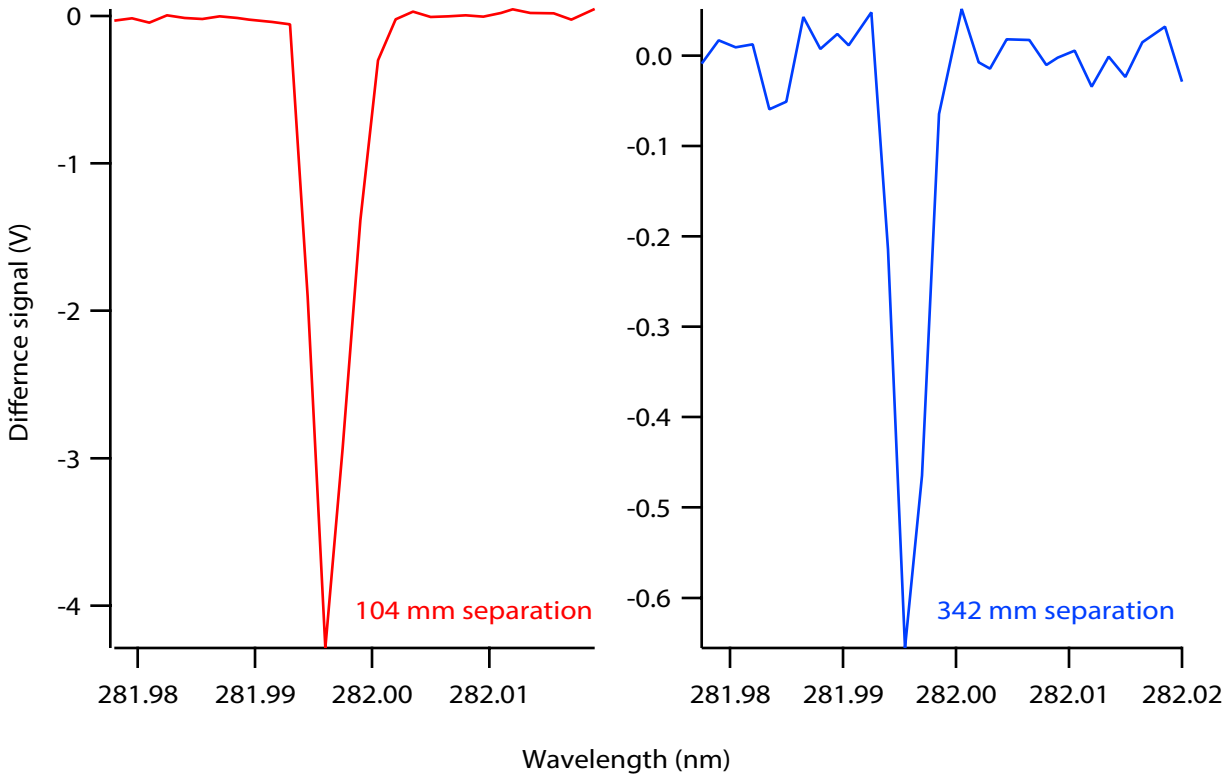
Difference signal (V)
0
-1
-2
-3
-4
104 mm separation
281.98
281.99
282.00
282.01
0.0
-0.1
-0.2
-0.3
-0.4
-0.5
-0.6
342 mm separation
281.98
281.99
282.00
282.01
282.02
Wavelength (nm)

4.5 Summary

This chapter details the components and capabilities of the new flow tube apparatus and the experimental protocols for characterizing flow and detection. We demonstrate robust flow characterization in the laminar and turbulent regimes with radially resolved velocity measurements. We ensure uniform flow is developed prior to photolysis by calculating hydrodynamic entrance lengths from the Reynolds numbers we measure. Our flow characterization reveals the timescales for in-flow transport, and thus, for unimolecular reactions amenable to kinetics studies. We employ LIF on OH following nitric acid photolysis with the lasers overlapped in a static flow tube environment to characterize our detection capabilities. This characterization culminates with in-flow LIF detection where we are able to observe OH signal generated from nitric acid photodissociation at both ends of the photolysis region in the short-flow configuration at various flow rates.

References

[1] C. J. Howard. Kinetic measurements using flow tubes. *J. Phys. Chem.*, 83(1):3–9, 1979.

[2] A. E. Berke. *Reactions near their energetic limit: methane and monodeuterated methane with chlorine and bromine atoms*. PhD thesis, University of Wisconsin, 2012.

[3] C. G. Heid. *Vibrational predissociation dynamics of the ammonia trimer and the 3-aminophenol-ammonia complex*. PhD thesis, University of Wisconsin, 2014.

[4] K. Avila, D. Moxey, A. de Lozar, M. Avila, D. Barkley, and B. Hof. The onset of turbulence in pipe flow. *Science*, 333(6039):192–196, 2011.

[5] Y. A. Cengel and J. M. Cimbala. *Fluid mechanics: Fundamentals and applications*. McGraw-Hill Higher Education, Boston, 2006.

[6] L. F. Keyser. High-pressure flow kinetics. a study of the hydroxyl + hydrogen chloride reaction from 2 to 100 torr. *J. Phys. Chem.*, 88(20):4750–4758, 1984.

[7] J. P. D. Abbatt, K. L. Demerjian, and J. G. Anderson. A new approach to free-radical kinetics: radially and axially resolved high-pressure discharge flow with results for hydroxyl + (ethane, propane, n-butane, n-pentane) .fwdarw. products at 297 K. *J. Phys. Chem.*, 94(11):4566–4575, 1990.

[8] J. V. Seeley, J. T. Jayne, and M. J. Molina. Kinetic studies of chlorine atom reactions using the turbulent flow tube technique. *J. Phys. Chem.*, 100(10):4019–4025, 1996.

[9] Henry P. Bakewell Jr. and John L. Lumley. Viscous sublayer and adjacent wall region in turbulent pipe flow. *The Physics of Fluids*, 10(9):1880–1889, 1967.

[10] O. Rattigan, E. Lutman, R.L. Jones, R.A. Cox, K. Clemitshaw, and J. Williams. Temperature-dependent absorption cross-sections of gaseous nitric acid and methyl nitrate. *Journal of Photochemistry and Photobiology A: Chemistry*, 66(3):313 – 326, 1992.

[11] L.S. Rothman, I.E. Gordon, Y. Babikov, A. Barbe, D. Chris Benner, P.F. Bernath, M. Birk, L. Bizzocchi, V. Boudon, L.R. Brown, A. Campargue, K. Chance, E.A. Cohen, L.H. Coudert, V.M. Devi, B.J. Drouin, A. Fayt, J.-M. Flaud, R.R. Gamache, J.J. Harrison, J.-M. Hartmann, C. Hill, J.T. Hodges, D. Jacquemart, A. Jolly, J. Lamouroux, R.J. Le Roy, G. Li, D.A. Long, O.M. Lyulin, C.J. Mackie, S.T. Massie, S. Mikhailenko, H.S.P. Müller, O.V. Naumenko, A.V. Nikitin, J. Orphal, V. Perevalov, A. Perrin, E.R. Polovtseva, C. Richard, M.A.H. Smith, E. Starikova, K. Sung, S. Tashkun, J. Tennyson, G.C. Toon, Vl.G. Tyuterev, and G. Wagner. The hitran2012 molecular spectroscopic database. *J. Quant. Spectrosc. Radiat. Transfer*, 130:4 – 50, 2013. HITRAN2012 special issue.

Chapter 5

Towards atmospheric chemistry studies in the flow tube

The impetus for building the flow tube apparatus came about in an effort to study atmospherically-relevant chemistry for which our molecular beam apparatus is poorly suited. A group at Sandia's Combustion Research Facility had recently demonstrated an insightful new method for generating carbonyl oxide biradicals known as Criegee intermediates using laser photolysis of a halogenated precursor in the presence of O_2.[1] We endeavored to use an analogous approach to generate peroxy radicals that occur routinely during atmospheric oxidation and are thought to contribute significantly to OH regeneration in the troposphere through unimolecular processes.[2]

Convinced of our qualifications for the job of photodissociating halogenated precursors, we considered the advantages and challenges using the molecular beam apparatus would present. Time-of-flight mass detection is a convenient way to probe OH products, and REMPI schemes for OH are known.[3] However, the timescale for generating OH from the precursor *via* a peroxy radical made in the molecular beam was problematic for the setup we used to study $CHBrCl_2$. Photodissociation of the halogenated precursor causes the fragments to recoil, and they will leave the laser-interaction region if the probe pulse is delayed for too long with the lasers overlapped spatially. This was not a problem in the $CHBrCl_2$ studies because dissociation was rapid and we probed the products immediately. To generate peroxy radicals, O_2 addition occurs subsequent to the carbon-halogen bond cleavage, and the OH products we wish to detect are then generated by isomerization and decomposition

of the peroxy radical. The time required for this chemistry is prohibitively long relative to the residence time in the laser interaction region with the beams overlapped. For instance, if we use the translational energies we measure for $CHBrCl_2$ photodissociation and conservatively assume a focused beam waist of 10 μm in the laser interaction region, the recoiling photofragments leave the interaction region in $\sim$10 ns. The unimolecular chemistry we wish to study occurs on timescales closer to 1 s. Furthermore, the pressures in the main chamber of the molecular beam apparatus ensure a collision-free environment in the laser-interaction region, which would prevent O_2 addition. To account for these issues, we would need to photodissociate the halogenated precursor at the nozzle of the pulsed valve, which the apparatus is not presently equipped to do. If we did modify the window ports on the apparatus, it is possible we could generate peroxy radicals prior to the detection region. However, supersonic expansion conditions would be much colder and lower pressure than ambient atmospheric processes, and the lifetime of the peroxy radicals may be longer than the present predictions made for atmospheric conditions.

While detection in the molecular beam apparatus is ideal for resolving mass and relative quantum state populations, it is less ideal for extracting kinetics information. Although solely detecting OH would be worthwhile to verify unimolecular chemistry as a source for OH recycling in the atmosphere, quantifying rate constants would be more useful to reconciling atmospheric model predictions with measurements. A flow tube addresses difficulties inherent with generating peroxy radicals in the beam in a straightforward way and is well suited for kinetics measurements. We can generate peroxy radicals in the flow tube by photodissociating the precursor in one region, and allowing ample time for O_2 addition, isomerization, and eventual decomposition during transport to another region where the

products are detected. The high pressures in the flow tube (relative to the molecular beam) facilitate collisions leading to O_2 addition, and the transport time can be broadly tuned by the pressure and flow rate. The pressures are also much closer to atmospheric conditions. This situation is ideal for studying atmospherically-relevant unimolecular chemistry without competition from naturally occurring bimolecular processes. Although our group has historically cared about the dynamics of nitric acid photolysis,[4–6] we use it in the flow tube as a proxy for this atmospheric chemistry during characterization. This chapter will touch on the precedent for studying the unimolecular decomposition of peroxy radicals, the methodology we will employ to generate the radicals in the flow tube, and the initial precursors we target to this end.

5.1 Peroxy radicals in the troposphere

Peroxy radicals in the atmosphere react with NO in urban (high NO_x) environments, which generates tropospheric ozone by interrupting the otherwise ozone-neutral NO_x cycle. The NO_x cycle

$$NO_2 \xrightarrow{h\nu} NO + O(^3P) \tag{5.1}$$

$$O_2 + O(^3P) \rightarrow O_3 \tag{5.2}$$

$$NO + O_3 \rightarrow NO_2 + O_2 \tag{5.3}$$

is initiated by NO_2 photolysis with sunlight, which produces excited oxygen atoms that can react with O_2 to make ozone. In the troposphere, ozone is one of only six criteria air pollutants designated by the US National Ambient Air Quality Standards. The Environmental Protection Agency (EPA) regulates criteria pollutants due to their harmful effects on human

health and the environment, which are well documented.[7,8] The reaction between NO and a generic RO_2 peroxy radical

$$NO + RO_2 \rightarrow RO + NO_2 \tag{5.4}$$

prevents the NO_x cycle from destroying the ozone it generates (Reactions 5.2 and 5.3).

The oxidation of volatile organic compounds (VOCs) produces peroxy radicals in the atmosphere. VOCs are emitted largely from biogenic sources such as vegetation, and oxidized primarily by the OH radical. The most prominent tropospheric VOC is isoprene, and its oxidation leads primarily to methyl vinyl ketone (MVK) and methacrolein (MACR).[9] The formation of either compound proceeds *via* a peroxy radical intermediate generated by rapid O_2 addition following OH oxidation of isoprene. The MVK and MACR products undergo similar chemistry, generating additional peroxy radical species and progressively more saturated VOCs. Highly saturated VOCs will eventually form secondary aerosol, another EPA criteria pollutant.

The fate of peroxy radicals under ambient atmospheric conditions is NO_x-dependent. When reactive partners are readily available, Reaction 5.4 is the dominant loss process for RO_2. Under low-NO_x conditions, peroxy radicals can react with RO_2 or HO_2 partners, but an isomerization route leading to unimolecular decomposition proposed by Peeters *et al.* is calculated to occur more rapidly (< 1 s).[10] This decomposition route recycles the OH used up in the initial oxidation step. Thus, peroxy radical chemistry in the atmosphere is important not only for its interaction with the NO_x cycle to generate ozone, but also for the tropospheric OH budget.

5.2 Peroxy radical production and first targets

We use MACR oxidation as an instructive, prototypical example of the unimolecular chemistry we wish to isolate and study in the flow tube. Figure 5.1 shows pathways leading to the MACR-derived peroxy radical target (red). The first pathway (in green) is the typical formation of the peroxy radical in the atmosphere. The second pathway (in blue) is our proposed formation mechanism utilizing the photodissociation of a halogenated precursor in the presence of O_2. This method of generating the MACR-derived peroxy radical follows the method of Welz *et al.*,[1] and a similar method has been demonstrated in the absence of O_2 to study intermediates of isoprene oxidation.[11]

Figure 5.1 also shows the fate of the MACR-derived peroxy radical in the atmosphere. In the presence of NO_x, the peroxy radical follows one of two reaction pathways with NO, which produces either methacrolein hydroxynitrate ($MACRONO_2$) or hydroxyacetone (HAC). Thus, in the absence of unimolecular chemistry, the ratio of $MACRONO_2$ to HAC should be constant as a function of NO concentration (although at very low concentrations, self-reaction plays a role as well). Crounse *et al.* show that the $MACRONO_2$/HAC ratio in fact declines sharply under low NO_x conditions.[12] They also find evidence for the recycling of isotopically labeled OH used to oxidize MACR which cannot be due to the bimolecular chemistry. They propose a 1,4-H shift and subsequent decomposition as an additional source of HAC and a recycling mechanism for the OH used in the initial MACR oxidation. Based on the decline in the measured $MACRONO_2$/HAC ratio, the unimolecular chemistry appears to be important in regimes where the MACR-peroxy radical lifetime is > 0.5 s.

Figure 5.1: Mechanisms for MACR-derived peroxy radical formation and subsequent chemistry in the atmosphere. The oxidation of MACR in the atmosphere (green) generates the peroxy radical in red, which we propose to generate alternatively through photodissociation of an appropriate halogenated precursor (blue). Bimolecular reactions produce either methacrolein hydroxynitrate ($MACRONO_2$) or hydroxyacetone (HAC), while a 1,4-H shift and subsequent decomposition produces HAC exclusively.

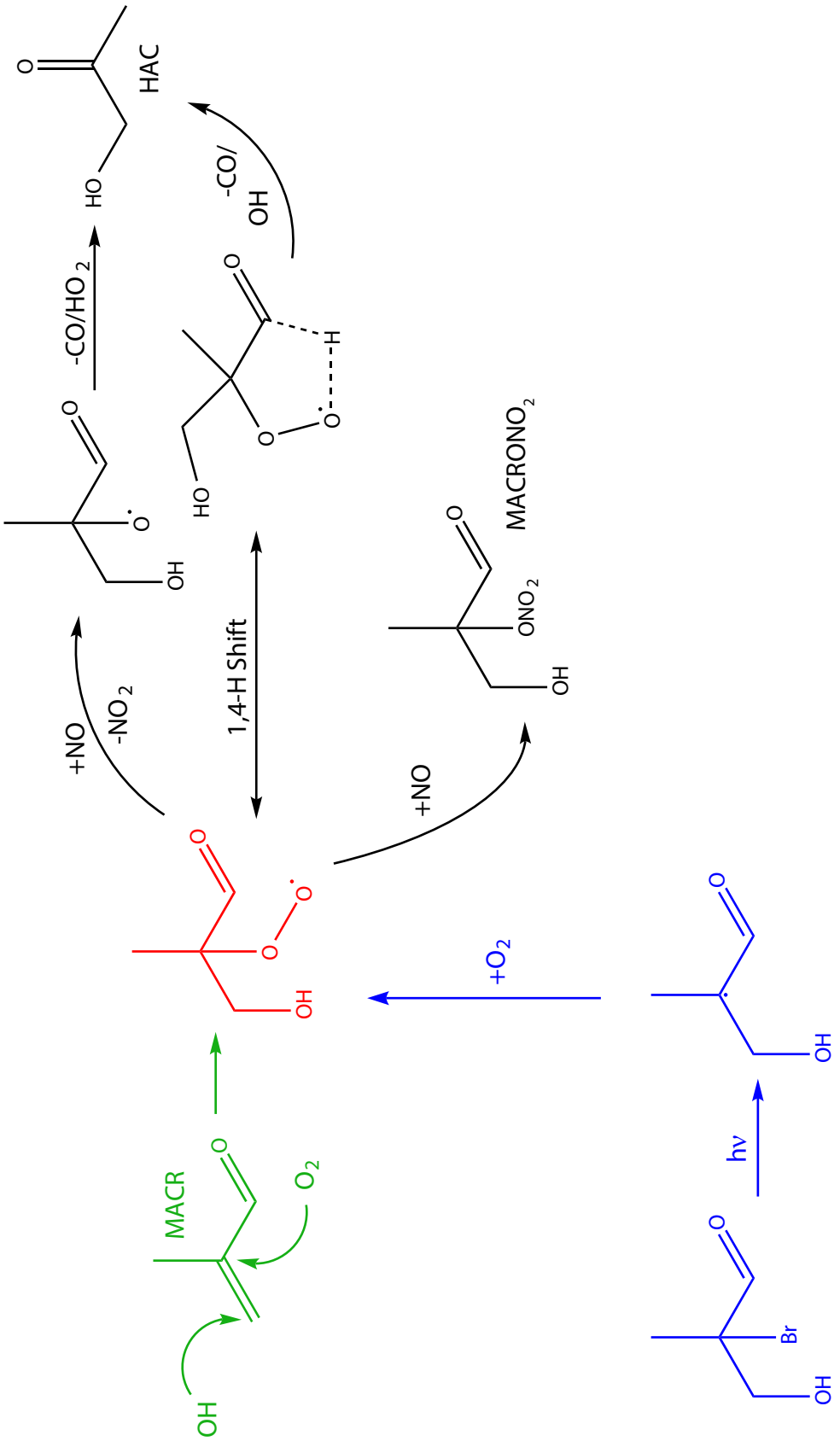
MACR
OH
O2
hν
Br
OH
+O2
+NO
MACRONO2
ONO2
OH
1,4-H Shift
+NO
-NO2
-CO/HO2
HAC
HO
-CO/
OH
HO
OH

We considered a few halogenated precursor targets for initial flow tube studies, including the one pictured in Figure 5.1. The synthesis and purification of these precursors is not trivial, particularly due to the propensity of the terminal hydroxy group to undergo ring-closing in solution. Eventually we settled on a target with a methyl group in place of the hydroxy group, which turns off a potential 1,5-H shift mechanism but still allows for the 1,4-H shift depicted in Figure 5.1. We enlisted the help of Adrian Amador (Yoon Group) for synthesis, purification, and degradation analysis. Figure 5.2 shows the structure of the precursor and a ^{1}H NMR spectrum of the purified sample. The synthetic procedure was originally described by Lee *et al.*,[13] but Adrian provided a more detailed account of the synthesis that we include in Appendix D. The appendix also shows that the precursor target is stable in the freezer after many months. This precursor will likely be the first target for atmospherically-relevant kinetics measurements in the flow tube, but as we do not know the vapor pressure of the compound, it remains to be seen how amenable it is to flow tube studies.

Figure 5.2: Structure and ^{1}H NMR spectrum of the precursor target synthesized by Adrian Amador.

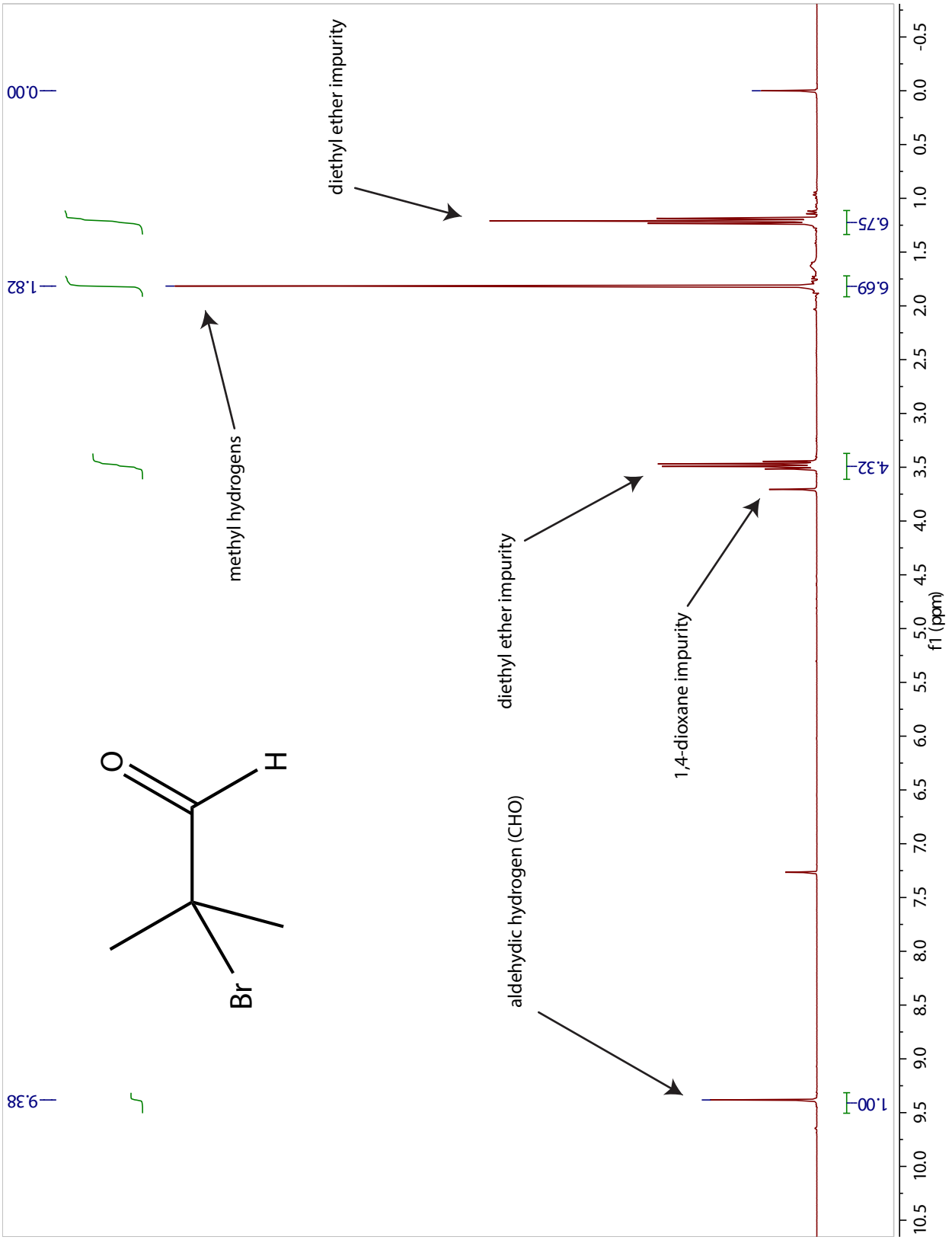
diethyl ether impurity
methyl hydrogens
diethyl ether impurity
1,4-dioxane impurity
aldehydic hydrogen (CHO)
O
H
Br
9.38
1.82
0.00
1.00
6.69
6.75
4.32
f1 (ppm)

References

[1] O. Welz, J. D. Savee, D. L. Osborn, S. S. Vasu, C. J. Percival, D. E. Shallcross, and C. A. Taatjes. Direct kinetic measurements of criegee intermediate (CH_2OO) formed by reaction of CH_2I with O_2. *Science*, 335(6065):204–207, 2012.

[2] D. R. Glowacki and M. J. Pilling. Unimolecular reactions of peroxy radicals in atmospheric chemistry and combustion. *Chem. Phys. Chem.*, 11(18):3836–3843, 2010.

[3] M. E. Greenslade, M. I. Lester, D. Č. Radenović, A. J. A. van Roij, and D. H. Parker. (2+1) resonance-enhanced ionization spectroscopy of a state-selected beam of oh radicals. *J. Chem. Phys.*, 123(7):074309, 2005.

[4] A. Sinha, R. L. Vander Wal, L. J. Butler, and F. F. Crim. Two-color vibrationally mediated photodissociation of nitric acid. *J. Phys. Chem.*, 91(18):4645–4647, 1987.

[5] A. Sinha, R. L. Vander Wal, and F. F. Crim. The vibrationally mediated photodissociation dynamics of nitric acid. *J. Chem. Phys.*, 91(5):2929–2938, 1989.

[6] A. Sinha, R. L. Vander Wal, and F. F. Crim. State-resolved unimolecular reactions: The vibrational overtone initiated decomposition of nitric acid. *J. Chem. Phys.*, 92(1):401–410, 1990.

[7] United States Environmental Protection Agency. Health effects of ozone polution. https://www.epa.gov/ozone-pollution/health-effects-ozone-pollution. Accessed: 08-22-2017.

[8] United States Environmental Protection Agency. Ecosystem effects of ozone polution. https://www.epa.gov/ozone-pollution/ecosystem-effects-ozone-pollution. Accessed: 08-22-2017.

[9] S. A. Montzka, M. Trainer, P. D. Goldan, W. C. Kuster, and F. C. Fehsenfeld. Isoprene and its oxidation products, methyl vinyl ketone and methacrolein, in the rural troposphere. *J. Geophys. Res. Atmos.*, 98(D1):1101–1111, 1993.

[10] J. Peeters, T. L. Nguyen, and L. Vereecken. Hox radical regeneration in the oxidation of isoprene. *Phys. Chem. Chem. Phys.*, 11:5935–5939, 2009.

[11] Erin E. Greenwald, Buddhadeb Ghosh, Katie C. Anderson, Kristin S. Dooley, Peng Zou, Talitha Selby, David L. Osborn, Giovanni Meloni, Craig A. Taatjes, Fabien Goulay, and Simon W. North. Isomer-selective study of the OH initiated oxidation of isoprene in the presence of O_2 and NO. i. the minor inner OH-addition channel. *The Journal of Physical Chemistry A*, 114(2):904–912, 2010. PMID: 19928790.

[12] J. D. Crounse, H. C. Knap, K. B. Ørnsø, S. Jørgensen, F. Paulot, H. G. Kjaergaard, and P. O. Wennberg. Atmospheric fate of methacrolein. 1. peroxy radical isomerization following addition of OH and O_2. *J. Phys. Chem. A*, 116(24):5756–5762, 2012. PMID: 22452246.

[13] J. J. Lee, F. Z. Yang, Y. F. Lin, Y. C. Chang, K. H. Yu, M. C. Chang, G. H. Lee, Y. H. Liu, Y. Wang, S. T. Liu, and J. T. Chen. Unsymmetrical bidentate ligands of α-aminoaldimines leading to sterically controlled selectivity of geometrical isomerism in square planar coordination. *Dalton Trans.*, pages 5945–5956, 2008.

Appendices

Appendix A

Subroutines for the Butler impulsive model

This appendix contains the subroutines associated with the MATLAB code shown in Figure 3.14. We wrote the code from scratch, but the general idea for the model appears in *J. Phys. Chem. A*, **118**, 3211 (2014). We made the code general enough to work for any C–X photodissociation in which the equilibrium parent geometry and the total kinetic energy release (TKER) are known. Here, X refers to the halogen atom being cleaved. We present the subroutines in the order they appear in `butler_model.m` (Figure 3.14).

Figure A.1: MATLAB code for the `zero_cart.m` subroutine. The variables `input` and `i` are passed from `butler_model.m`, where `input` is a matrix of atomic coordinates and `i` is the column of that matrix containing the coordinates for the carbon atom in the C–X bond being cleaved.

```
function cart = zero_cart(input,i)

% Script written by W. G. Merrill
% CREATED: 09.16.2016
% LAST UPDATED: 09.16.2016

% Translates cartesian coordinates for atoms in molecule to put the ith
% atom at the origin. 'input' is a 3xN matrix, each column is the x,y,z
% coordinates for atom i.

sz = size(input);
cart = zeros(sz);

move = input(:,i);

for n = 1:sz(2)
   atom_coord = input(:,n);
   new_atom_coord = atom_coord - move;
   cart(:,n) = new_atom_coord;
end
```

Figure A.2: MATLAB code for the `makesph.m` subroutine. The variable `cart` is passed from `zero_cart.m` *via* `butler_model.m`. The subroutine changes the the coordinate system of the atoms from Cartesian to spherical, which makes rotational transformations more straightforward.

```
function sph = makesph(cart)

% Script written by W. G. Merrill
% CREATED: 09.16.2016
% LAST UPDATED: 09.16.2016

% cart is an 3xN matrix of cartesian coordinates for the N atoms of a
% molecule. The makesph function transforms the cartesian coordinate matrix
% to a spherical coordinate matrix of the same dimensions. The columns of
% cart are x,y,z coordinates, the columns of sph are r,theta,phi
% coordinates. For a given atom, r is the distance from that atom to the
% origin. Theta is the angle from z-axis to r. Phi is the counter-clockwise
% angle from the positive x-axis to the projection of r in the xy-plane.
% Angles are returned in degrees.

sz = size(cart);
sph = zeros(sz);

for n = 1:sz(2) % sz(2) is the number of columns in cart
    atom_cart = cart(:,n);
    % cart(:,n) is the nth column of cart, which is the x,y,z vector for
    % the nth atom in the molecule
    x = atom_cart(1);
    y = atom_cart(2);
    z = atom_cart(3);
    hypotxy = hypot(x,y);
    atom_sph(1) = hypot(hypotxy,z);
    % atom_sph(1) is r
    atom_sph(2) = 90 - rad2deg(atan2(z,hypotxy));
    % atom_sph(2) is theta
    atom_sph(3) = rad2deg(atan2(y,x));
    % atom_sph(3) is phi
    sph(:,n) = atom_sph;
end
```

Figure A.3: MATLAB code for the `rot_bond.m` subroutine. The variable `sph` is passed from `makesph.m` *via* `butler_model.m`. The variable `i` is the column of the `input_matrix` variable for `butler_model.m` containing the coordinates for the halogen atom in the C−X bond being cleaved. The subroutine applies a rotational transformation to the molecule to put the C−X bond on the y-axis.

```
function rot = rot_bond(sph,i)

% Script written by W. G. Merrill
% CREATED: 09.16.2016
% LAST UPDATED: 09.16.2016

% Rotates molecule to put atom i on the y-axis without changing the origin,
% so if (for instance) C-Br is the bond being broken, you choose C in the
% zero_cart function and Br in the rot_bond function to get the C-Br bond
% to lie long the y-axis.

sz = size(sph);
rot = zeros(sz);

rot_theta = sph(2,i)-90;
rot_phi = sph(3,i)-90;

for n = 1:sz(2)
   old_sph = sph(:,n);
   new_sph(1) = old_sph(1);
   new_sph(2) = old_sph(2)-rot_theta;
   new_sph(3) = old_sph(3)-rot_phi;
   rot(:,n) = new_sph;
end
```

Figure A.4: MATLAB code for the `makecart.m` subroutine. The variable `rot` is passed from `rot_bond.m` *via* `butler_model.m`. The subroutine puts the molecule back into Cartesian coordinates from the input in spherical coordinates.

```
function newcart = makecart(rot)

sz = size(rot);
newcart = zeros(sz);

for n = 1:sz(2)
    r = rot(1,n);
    theta = rot(2,n);
    phi = rot(3,n);
    x = r*sin(deg2rad(theta))*cos(deg2rad(phi));
    y = r*sin(deg2rad(theta))*sin(deg2rad(phi));
    z = r*cos(deg2rad(theta));
    cart = [x; y; z];
    newcart(:,n) = cart;
end
```

Figure A.5: MATLAB code for the `comfind.m` subroutine. The variable `coord` is passed from `makecart.m` *via* `butler_model.m`. The variable `mass` is a vector containing the mass of each atom in the parent. The variable `X` is the column of `coord` (and also mass) containing the coordinates for the halogen atom X. The subroutine finds the center of mass coordinates of the molecular photofragment (i.e. the parent minus X) by removing the mass and coordinate information for X from the inputs and converting the remaining coordinates to mass-weighted coordinates. It then sums the mass-weighted coordinates in each dimension and divides by the total mass.

```
function com = comfind(coord,mass,X)

rad_mass = mass;
rad_mass(:,X) = [];
rad_coord = coord;
rad_coord(:,X) = [];
sz = size(rad_coord);
mass_weighted_coord = zeros(sz);

for n = 1:sz(2)
   mass_weighted_coord(:,n) = rad_mass(n)*rad_coord(:,n);
end

mass_total = sum(rad_mass);

com_x = sum(mass_weighted_coord(1,:))/mass_total;
com_y = sum(mass_weighted_coord(2,:))/mass_total;
com_z = sum(mass_weighted_coord(3,:))/mass_total;

com = [com_x; com_y; com_z];
```

Figure A.6: MATLAB code for the `comtrans.m` subroutine. The variable `coord` is passed from `makecart.m` *via* `butler_model.m`. The variable `com` is passed from `comfind.m` *via* `butler_model.m`. The subroutine translates the entire parent molecule to put the center of mass for the molecular photofragment at the origin.

```
function comframe = comtrans(coord, com)

sz = size(coord);
comframe = zeros(sz);

for n = 1:sz(2)
comframe(:,n) = coord(:,n) - com;
end
```

Figure A.7: MATLAB code for the `itensor.m` subroutine. The variable `coord` is passed from `comtrans.m` *via* `butler_model.m`. The variable `mass` is a vector containing the mass of each atom in the parent. The variable `X` is the column of `coord` (and also `mass`) containing the coordinates for the halogen atom X. The subroutine calculates the 3-D inertia tensor for the molecular photofragment in the center of mass frame, which the model uses to calculate rotational energy imparted to the molecular fragment.

```
function tensor = itensor(coord,mass,X)

rad_mass = mass;
rad_mass(:,X) = [];
rad_coord = coord;
rad_coord(:,X) = [];

sz = size(rad_coord);
I_xx_values = zeros(1,sz(2));
I_yy_values = zeros(1,sz(2));
I_zz_values = zeros(1,sz(2));
I_xy_values = zeros(1,sz(2));
I_yz_values = zeros(1,sz(2));
I_xz_values = zeros(1,sz(2));

for n = 1:sz(2)
    I_xx_values(n) = ((rad_coord(2,n)^2)+(rad_coord(3,n)^2))*rad_mass(n);
    I_yy_values(n) = ((rad_coord(1,n)^2)+(rad_coord(3,n)^2))*rad_mass(n);
    I_zz_values(n) = ((rad_coord(1,n)^2)+(rad_coord(2,n)^2))*rad_mass(n);
    I_xy_values(n) = (rad_coord(1,n))*(rad_coord(2,n))*rad_mass(n);
    I_yz_values(n) = (rad_coord(2,n))*(rad_coord(3,n))*rad_mass(n);
    I_xz_values(n) = (rad_coord(1,n))*(rad_coord(3,n))*rad_mass(n);
end

I_xx = sum(I_xx_values);
I_yy = sum(I_yy_values);
I_zz = sum(I_zz_values);

I_xy = sum(I_xy_values);
I_yz = sum(I_yz_values);
I_xz = sum(I_xz_values);

tensor = zeros(3);

tensor(1,1) = I_xx;
tensor(2,2) = I_yy;
tensor(3,3) = I_zz;

tensor(1,2) = I_xy;
tensor(2,1) = I_xy;

tensor(2,3) = I_yz;
tensor(3,2) = I_yz;

tensor(1,3) = I_xz;
tensor(3,1) = I_xz;
```

Figure A.8: MATLAB code for the `findj.m` subroutine. All variables are passed from `butler_model.m`. The variable `TKER` is the total kinetic energy release we measure with the VMI technique. The variable `mass` is a vector containing the mass of each atom in the parent. The variable `X` is the index of `mass` containing the mass for the halogen atom X. The subroutine calculates the relative velocity of the two fragments as they separate using conservation of momentum.

```
function relv = findrelv(TKER,mass,X)

mass_X = mass(X);
mass_mol = sum(mass) - mass(X);

v_mol = ((mass_X/(mass_mol*(mass_X + mass_mol)))*(2*TKER))^(1/2);
v_X = ((mass_mol/(mass_X*(mass_X + mass_mol)))*(2*TKER))^(1/2);

% this calculates magnitudes of the velocity vectors for the two
% photofragments. Since they are flying apart from each other along the
% y-axis, the directions must be opposite:

 v_X = -1*v_X;

 relv = [0; 0; 0];
 relv(2) = v_mol - v_X;
```

Figure A.9: MATLAB code for the `findj.m` subroutine. The variable `relv` is passed from `findrelv.m` *via* `butler_model.m`. The variable `coord` is passed from `comtrans.m` *via* `butler_model.m`. The variable `mass` is a vector containing the mass of each atom in the parent. The variable `X` is the column of `coord` (and also `mass`) containing the coordinates for the halogen atom X. The subroutine calculates the angular momentum vector of the recoiling molecular photofragment, which the model uses to calculate rotational energy imparted to the molecular fragment.

```
function J = findj(relv,coord,mass,X)

mass_X = mass(X);
mass_mol = sum(mass) - mass(X);
rmass = mass_X*mass_mol/(mass_X + mass_mol);

r = coord(:,X);

J = cross(r,rmass*relv);
```

Appendix B

LabView code for the flow tube apparatus

This appendix contains the components of the LabView code responsible for running flow tube experiments. The main virtual instrument (VI) is `flowtube_megastation.vi`. There are many version of this program located on the PC in the folder `C:LabView\MoFlow_code`. The routines in this appendix will cover the most up-to-date version of the code at the time of writing. Figure 4.13 shows the front end of the code and Section 4.2.7 describes it. Therefore, the scope of this appendix will be limited to the aspects LabView block diagram. Segments of the block diagram will be displayed as figures and figure captions will describe the function of each code segment.

Figure B.1: Setup for an analog input (AI) channel. `flowtube_megastation.vi` contains one of these setups for each AI channel (PMT, manometers, MFCs, etc.). The figure shows an example for the static manometer. The primary component of the AI channel setup is the DAQmx Create Channel subVI, which comes with the LabView program. The same VI will create a number of distinct channel types, but in this case we use the AI-voltage-basic option. The DAQmx Create Channel subVI requires a physical channel associated with the input, and the terminal configuration for that channel (10106 designates a differential configuration, see Figure 4.12). The "task" wire is passed between all of the DAQmx subVIs sequentially, and is initially created by the first DAQmx Create Channel subVI. The DAQmx Create Scale subVI converts the voltage the DAQ card reads in volts to a value corresponding with a different unit, such as Torr for the static manometer. The inputs for the DAQmx Create Scale subVI will depend on the voltage-to-signal conversion for a given device.

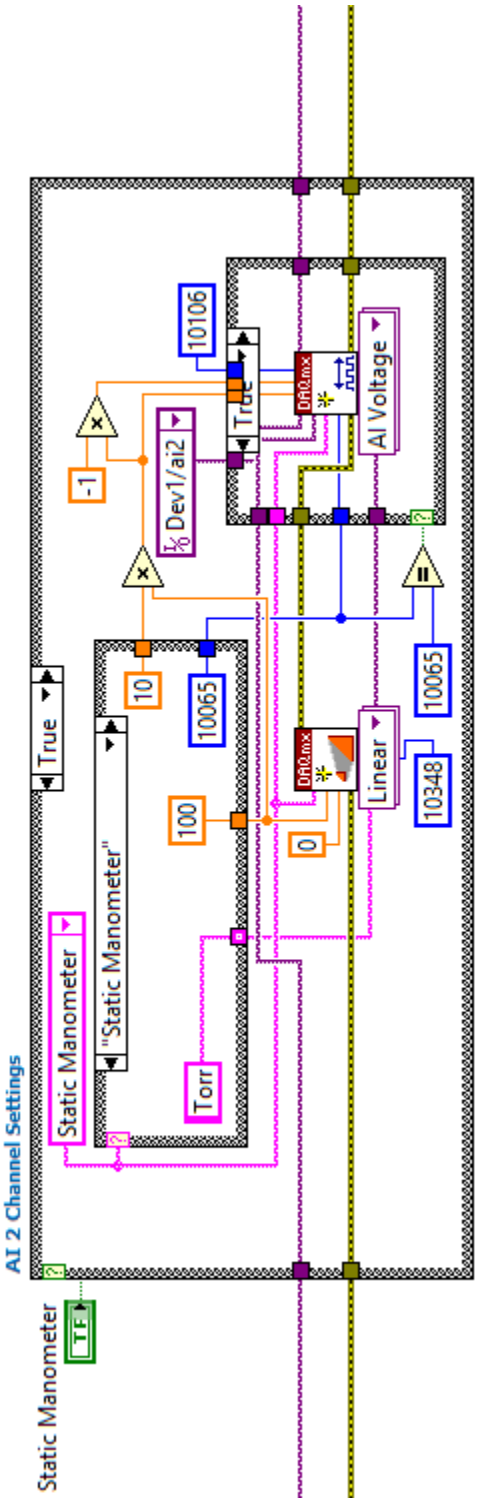
AI 2 Channel Settings
Static Manometer
TF
True
Static Manometer
"Static Manometer"
Torr
10
100
10065
-1
Dev1/ai2
10106
True
AI Voltage
Linear
0
10065
10348

Figure B.2: Sampling settings for `flowtube_megastation.vi`. These settings establish the use of hardware-timed sampling and the corresponding terminal for the hardware-supplied trigger from the DDG. The start trigger uses the PFI_{14} terminal. The main component of the sampling settings segment of code is the DAQmx Timing subVI that comes with the LabView program. The subVI is set to the sample-clock option. Various property nodes in this segment display information about the sampling settings on the front end of the program.

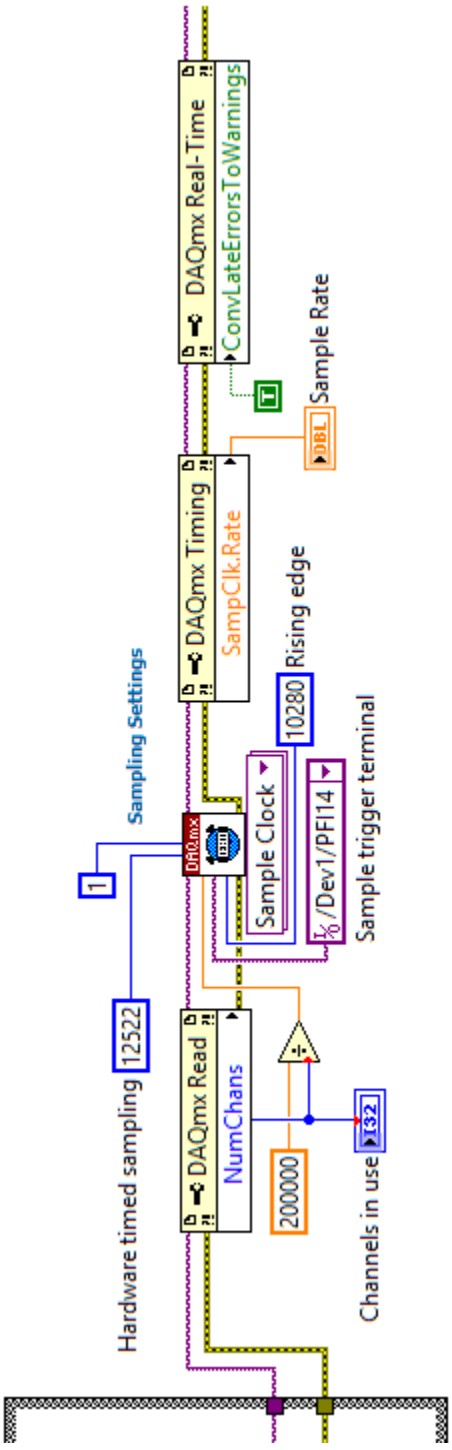
DAQmx Real-Time
ConvLateErrorsToWarnings
DAQmx Timing
SampClk.Rate
Sample Rate
DBL
Sampling Settings
1
Sample Clock
10280
Rising edge
/Dev1/PFI14
Sample trigger terminal
DAQmx Read
NumChans
12522
Hardware timed sampling
200000
I32
Channels in use

Figure B.3: Segment of `flowtube_megastation.vi` that reads in AI signal. First, the task wire is passed through the DAQmx Wait For Next Sample Clock subVI. Then, the task is passed to the DAQmx Read subVI with the Analog 1D wfm NChan NSamp setting selected. With this setting, the DAQmx Read subVI produces a 1D waveform output containing the AI data. The subVIs are part of a large while loop, and each loop iteration takes a new sample. The loop iterates each time a trigger pulse is received from PFI_{14} until a stop condition is met. Figure B.4 shows the stop conditions for the while loop. The waveform is then decomposed into AI values (Y), timing, and attributes with the index array and get waveform components functions. The AI values are added to an array with the build array function at each loop iteration. The waveform is then rebuilt and displayed on the front end.

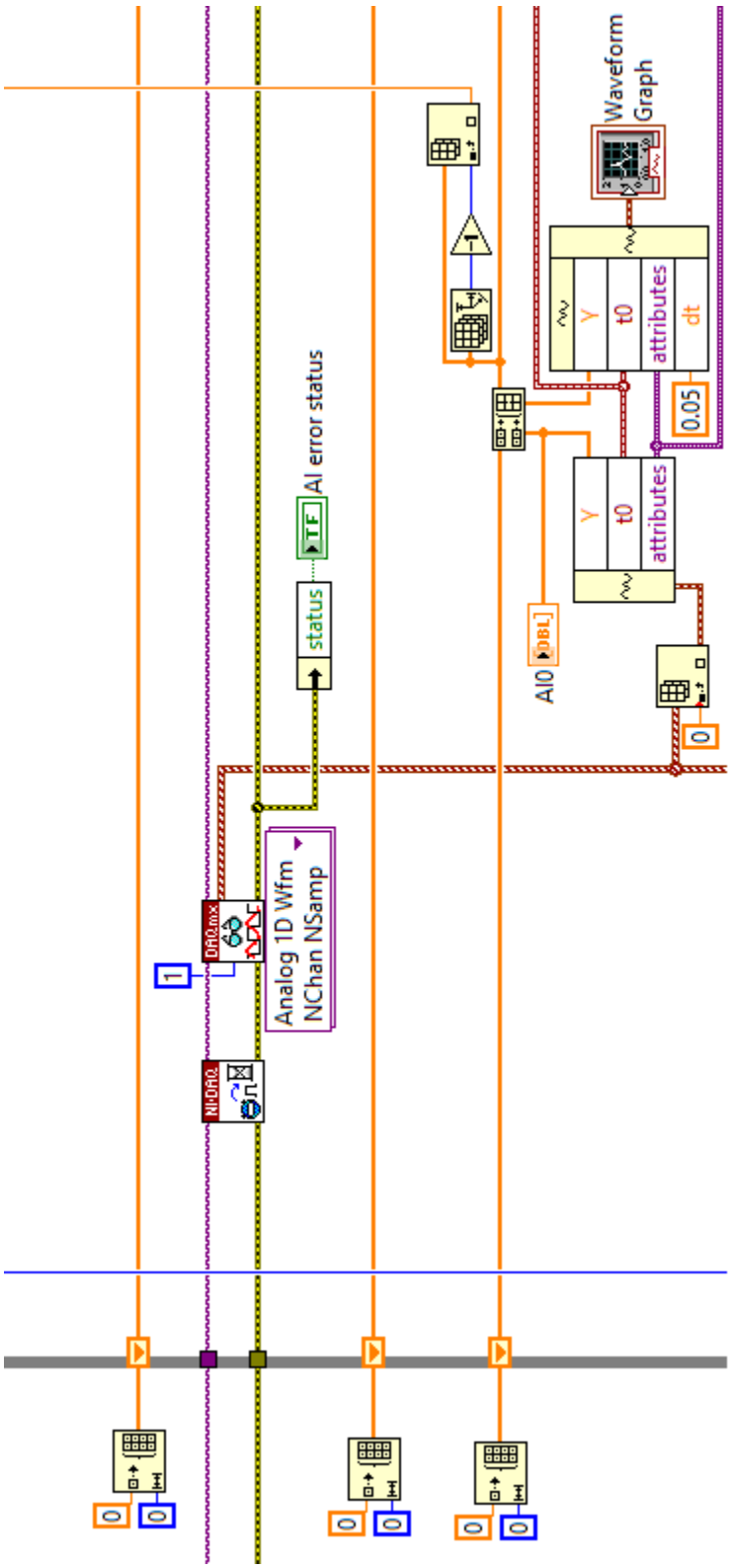
Waveform Graph
Y
t0
attributes
dt
0.05
AI error status
TF
status
AI0
DBL
Analog 1D Wfm NChan NSamp
1
0

Figure B.4: Stop conditions for the main while loop in `flowtube_megastation.vi`. The loops stops iterating if (1) the stop button on the front end is pressed, (2) the number of samples requested under finite sampling conditions is reached, (3) the target wavelength is reached when scanning the laser, or (4) an error occurs.

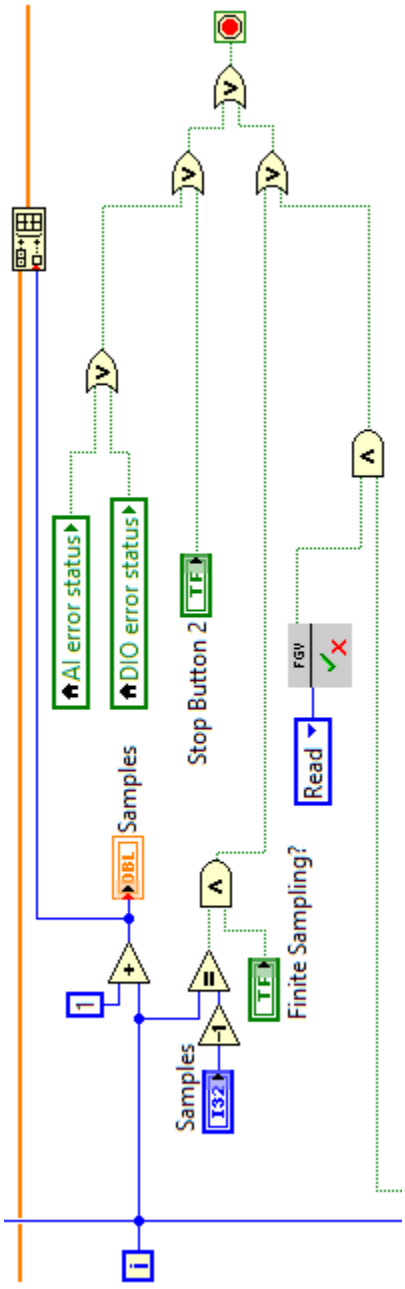
AI error status
DIO error status
Stop Button 2
Samples
Finite Sampling?
Read
Samples
DBL
TF
I32
FGV
1
-1
i

Figure B.5: Segment of the main while loop that records raw wavelength data and updates the readings on the front end. Outside of the main while loop, a separate while loop executes as fast as possible to read in the most recent wavemeter measurement with `read_lambda.vi`. The loop containing `read_lambda.vi` runs outside of the main while loop because communication with the wavemeter can take longer than the 50-ms iterations of the main while loop, which causes the program to miss samples. The value read in is passed between the loops with a functional global variable called FGV_read_WL. An additional global variable called FGV_nominal_WL, which reads the nominal wavelength, is compared to the wavemeter reading. If the nominal wavelength and the value read in by the wavemeter differ by more than 5 nm, a value of 0 is stored in the wavelength array. Values of 0 also occur when the wavemeter does not read, is saturated, or a MULTILINE error occurs. All 0 values are corrected after the array is built outside of the main while loop by searching for the closest non-zero wavelength value in the array and using that value instead of 0.

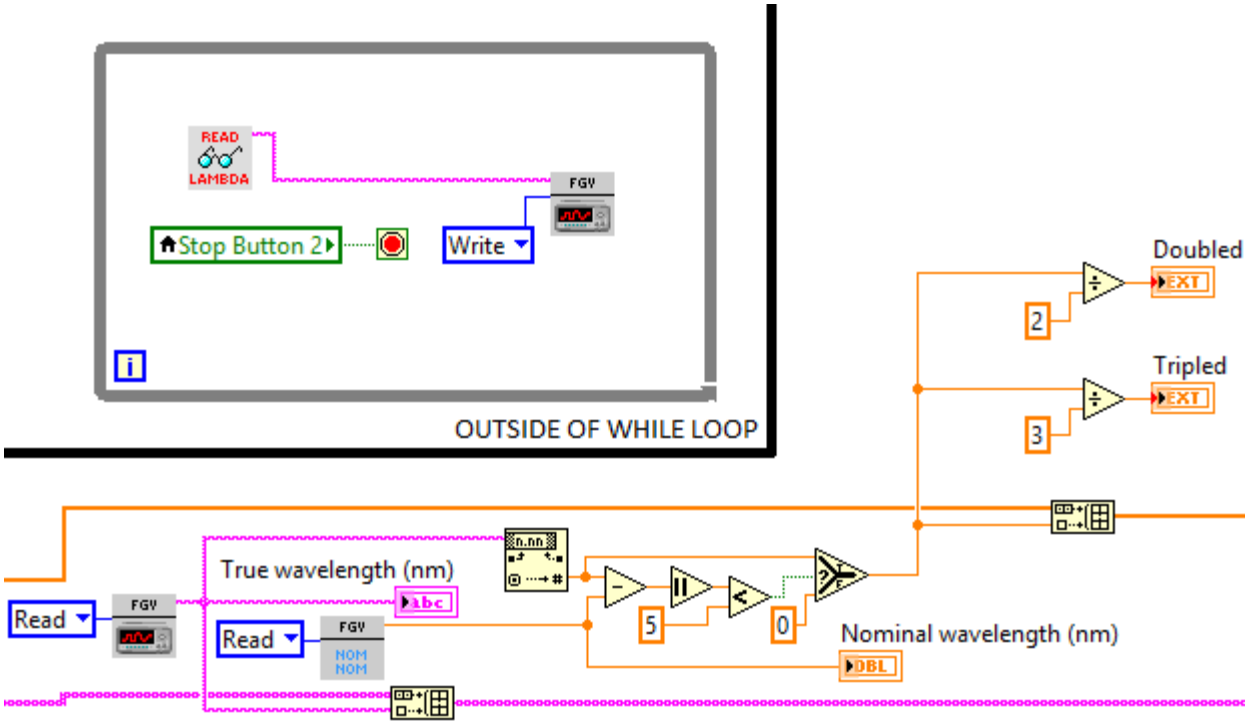
READ
LAMBDA
FGV
Stop Button 2
Write
i
OUTSIDE OF WHILE LOOP
Doubled
EXT
2
Tripled
EXT
3
Read
FGV
True wavelength (nm)
abc
Read
FGV
NOM
NOM
n.nn
5
0
Nominal wavelength (nm)
DBL

Figure B.6: Block diagram of `read_lambda.vi`, which uses RS-232 serial communication to read in text strings passed by the wavemeter. The strings are parsed with a series of VISA functions provided by the LabView program. The subVI output is a text string containing the wavelength or one of three errors: (1) NO SIGNAL, (2) SATURATED, and (3) MULTI-LINE. Those errors are converted to values of 0 in the wavelength array and handled as described in the caption for B.5.

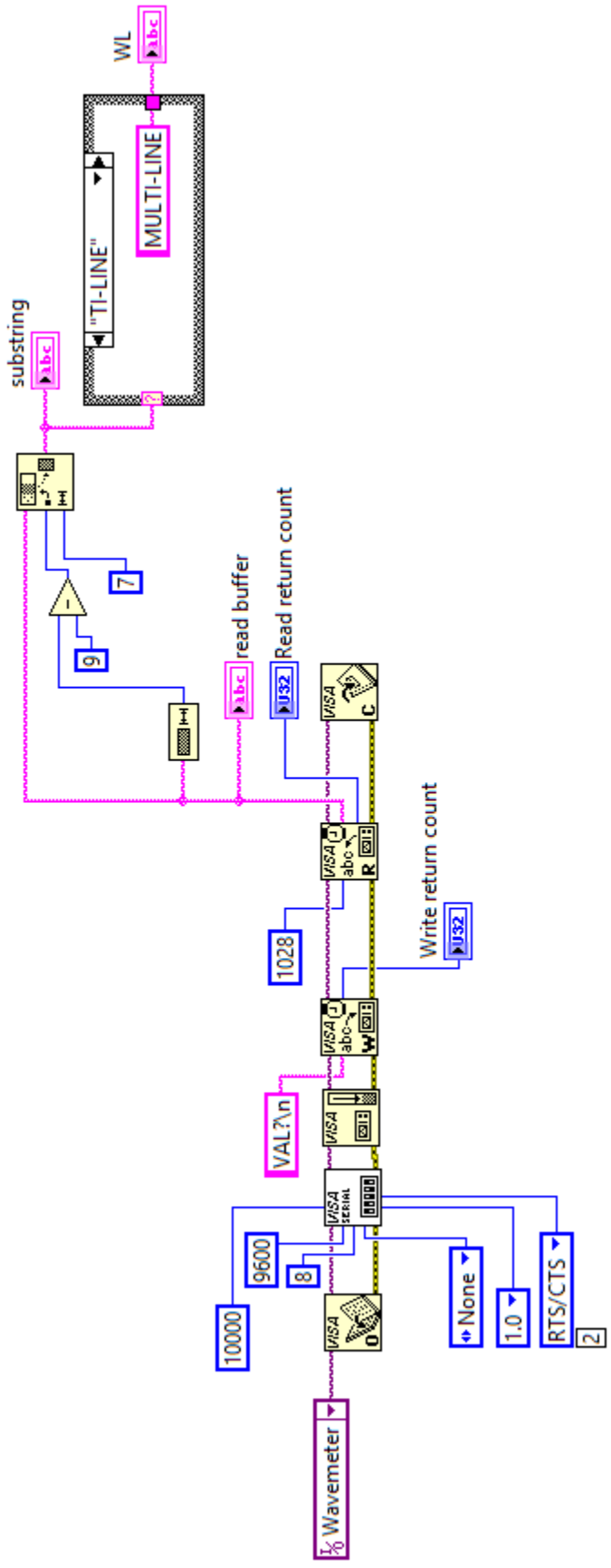
WL
MULTI-LINE
"TI-LINE"
substring
7
9
read buffer
Read return count
1028
Write return count
VALIN
10000
9600
8
None
1.0
RTS/CTS
2
Wavemeter

Figure B.7: Segment of the code that changes the wavelength in `flowtube_megastation.vi`. This routine is called by a case structure that becomes true when the number of shots the user requests at a given step have occurred. The program checks to see if the case structure condition is met inside of the main while loop, but the code shown in the figure exists outside of the main while loop because it can take longer to run than 50 ms, which causes the main loop to miss samples. The case structure condition is passed between outside of the main while loop by the FGV_change_WL functional global variable. The first section of the flat sequence structure assembles a file path according to which laser is being scanned and which grating is being used in that laser. It then reads in the `.txt` file associated with the path it built to obtain the most recent wavelength value written to that file. The `.txt` files are located in the same folder as the code. The second section of the flat sequence structure adds the user-defined step size to the value read in from the `.txt` file and calls `MoFlow_dye_scanner.vi` to communicate with the stepper motor in the dye laser and move to the new target value. `MoFlow_dye_scanner.vi` is modeled after the code written by Andrew Berke to move the dye laser.

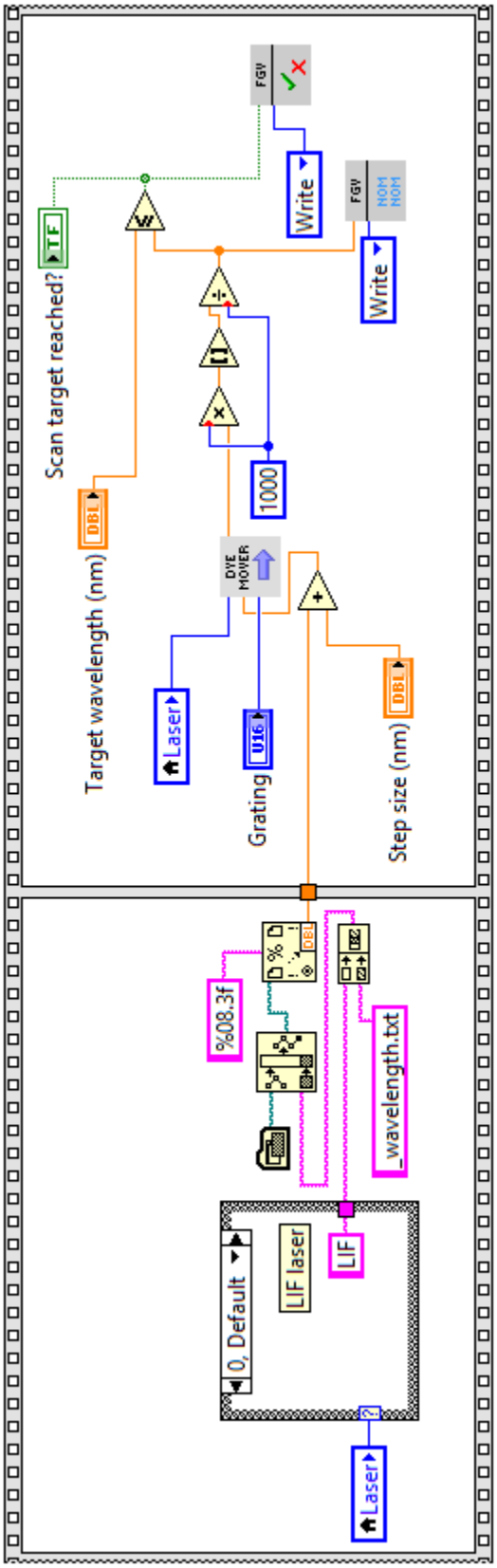
FGW
Write
FGW
NOM
NOM
Write
TF
Scan target reached?
DBL
Target wavelength (nm)
1000
DYE
MOWER
Laser
U16
Grating
DBL
Step size (nm)
%08.3f
DBL
_wavelength.txt
0, Default
LIF laser
LIF
Laser

Figure B.8: Main components of shutter control in `flowtube_megastation.vi`. The entirety of the shutter control routine includes logic to determine if the shutter was in the process of opening or closing for a particular loop iteration, and if so, it replaces the PMT signal for that iteration with an NaN value. The NaN value is then replaced during data processing outside of the main while loop by iterating between the two values on either side of the NaN value in the array. The DAQmx Write subVI with the Digital 1D Bool 1Chan 1Samp option sends a digital TTL output to the shutter *via* the P_0.0 terminal.

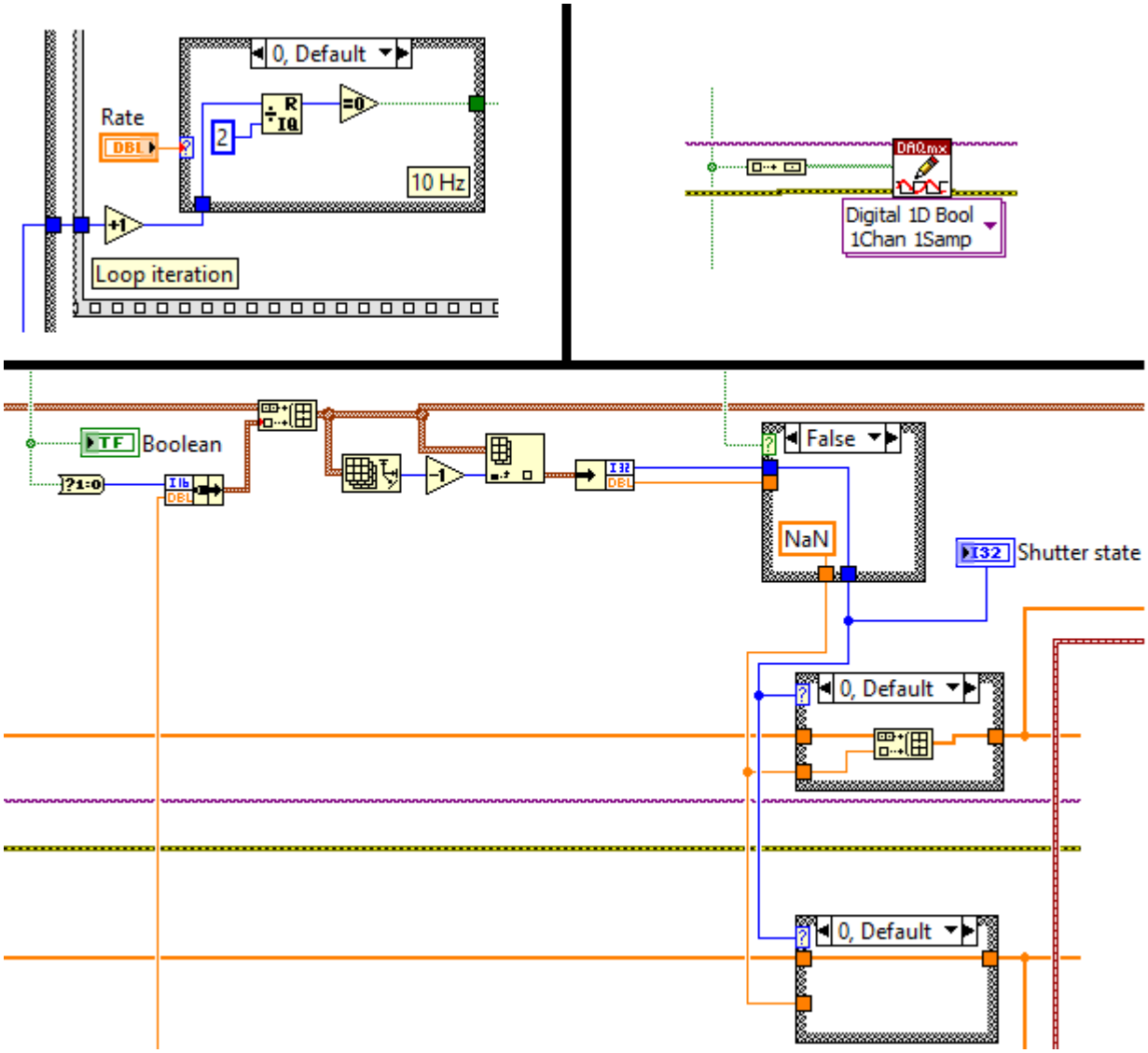
0, Default
Rate
DBL
2
10 Hz
+1
Loop iteration
DAQmx
Digital 1D Bool
1Chan 1Samp
TF
Boolean
?1:0
-1
False
NaN
I32
Shutter state
0, Default
0, Default

Figure B.9: An example of how data is logged in `flowtube_megastation.vi`. Delimited text files are named with outputs from the subVI `timestamp_maker.vi` (Figure B.10) appended with a back-end tag ("Raw_Data" in this case) and a front-end user-defined tag. The location where the file is saved is generated automatically by the subVI `folder_maker.vi` (Figure).

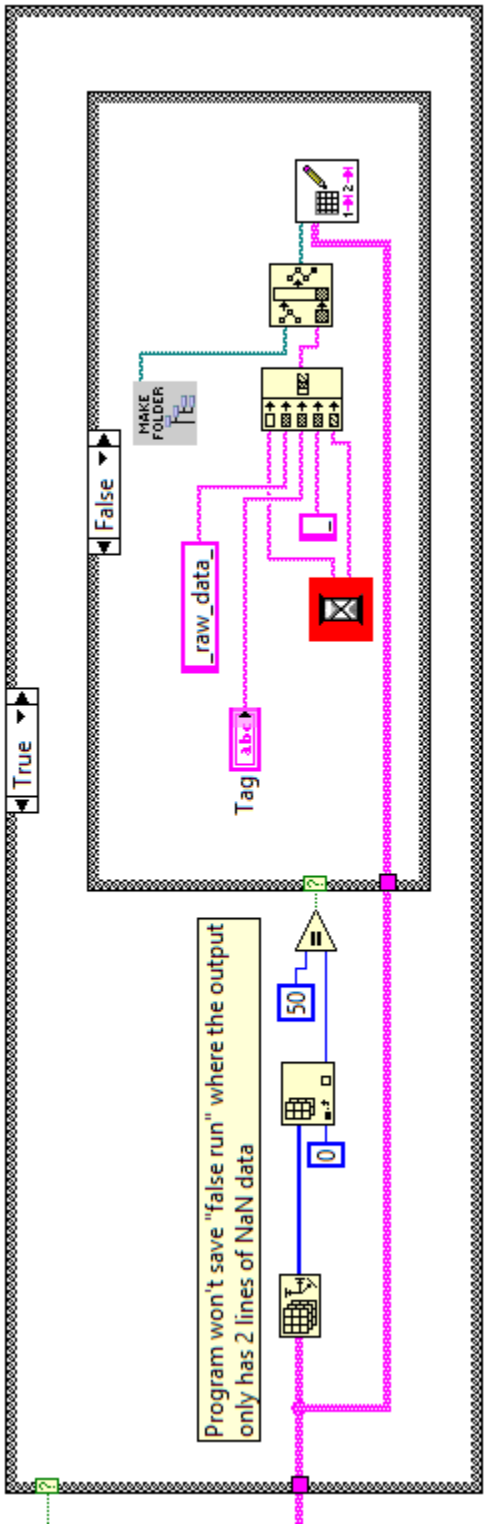
True
False
MAKE FOLDER
_raw_data_
Tag
Program won't save "false run" where the output only has 2 lines of NaN data
50
0

Figure B.10: Block diagram for `timestamp_maker.vi`, the subVI called to tag file names with the date and time the data was taken automatically. The Get Time/Date in Seconds function comes with the LabView program, and the code converts the timestamp output from this function to time and date strings amenable for file names.

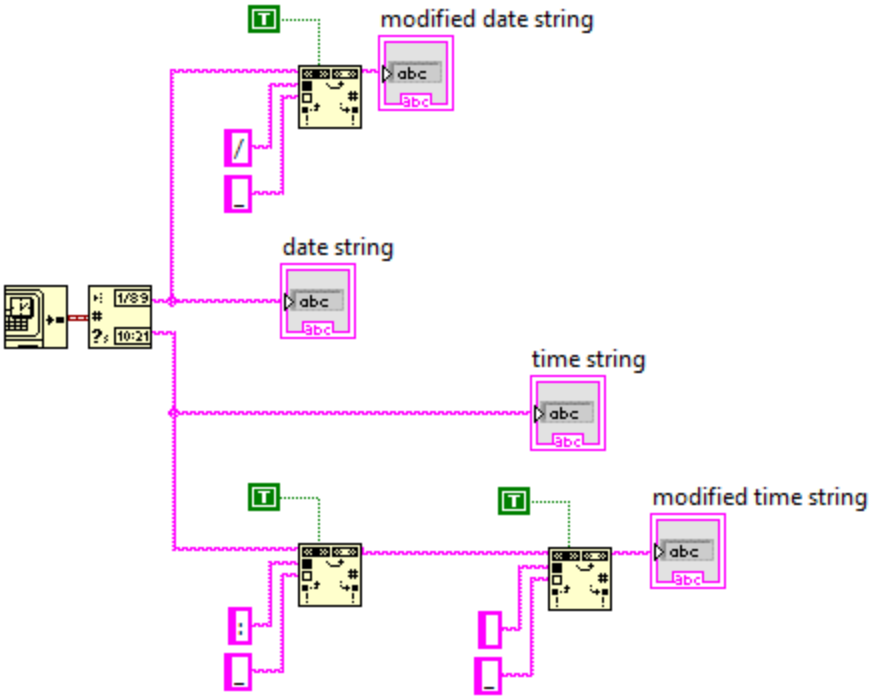
modified date string
abc
/
date string
abc
1/89
10:21
time string
abc
modified time string
abc
:

Figure B.11: Block diagram for `timestamp_maker.vi`, the subVI called to automatically save data in the correct folder, and create that folder if necessary. All data is saved in folders contained in `C:Data`. Each folder is named by month and year, which is parsed from `timestamp_maker.vi` outputs (Figure B.10)

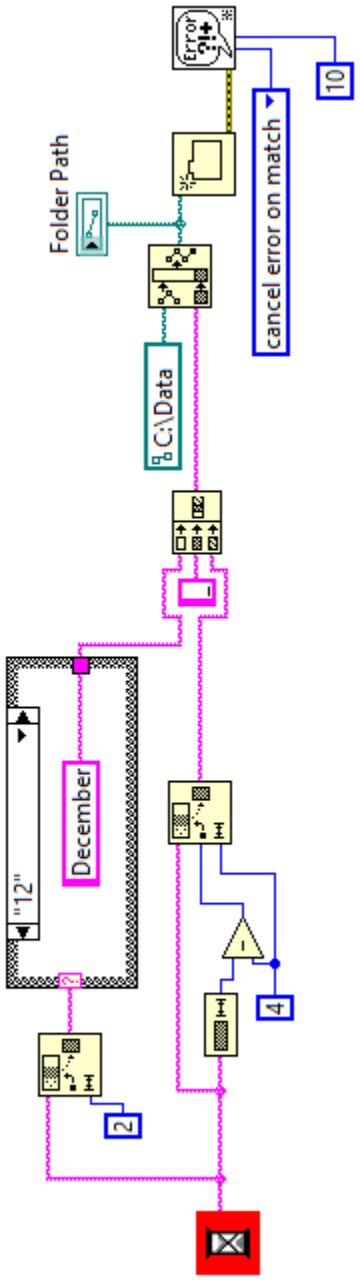
Error
10
cancel error on match
Folder Path
C:\Data
December
"12"
4
2

Appendix C

PID flow control

The MKS 946 vacuum controller utilizes proportional-integral-derivative (PID) control to maintain a pressure set point p_{sp}. PID control varies the flow rate of one or both mass flow controllers (MFCs) based on a user-defined "recipe." PID control works by assessing the difference between p_{sp} and actual flow tube pressure p and modulating the flow rate Q proportionally based the size of the error $e = p_{sp} - p$ over some time integral. The larger the e is, the greater the change to Q will be. The flow rate as a function of time is then given by

$$Q(t) = K_p \left[e(t) + \frac{1}{T_i} \int_0^t e(\tau) d\tau + T_d \frac{de(t)}{dt} \right] \tag{C.1}$$

where K_p is the proportional control parameter that impacts how responsive the system is to error. If K_p is set too high, PID control will be unstable and will not settle to a steady flow rate. If K_p is too low, PID control will not be responsive enough to maintain the set point pressure. This is the variable we tune most often to achieve ideal PID control settings. The default value is 10, but we used a value of 1 for lower pressure (< 100 Torr) characterization and higher values characterization requiring flow rates near the maximum of the 30 SLM MFC capacity. The remaining variables in Equation C.1 are covered below, along with the other components of the PID recipe that can be edited on the vacuum controller.

PID Ch: tells which channel the MFC is on for single MFC control (B1 or B2 in our case) or whether a ratio of two MFCs will be used (in this case Rat is the PID Ch name).

P Ctrl Ch: tells which channel has the pressure gauge to use for arriving at the pressure set point (A1 or A2 in our case). This should always be set to A1 with the setup described in Chapter 4 so that the static manometer is utilized.

P Sp: desired pressure set point in Torr.

Integral-Ti: T_i in Equation C.1, the integral control parameter. Sets a time for integration of the accumulated error. The default is 1 s.

Derivative-Td: T_d in the Equation C.1, the derivative control parameter. Scales the rate of change of the pressure reading with respect to time to contribute to the flow rate signal. For mass flow control, T_d should be set to zero due to its slow response of the flow rate to the corresponding pressure change.

Ceiling: Sets the upper limit of the control signal as a % of the full MFC scale. With some trial and error, this should be set just above where the flow rate ought to be for a given pressure so that it cannot overshoot too badly, but this is not crucial. We have found issues setting the ceiling to 100%, so often it is set to 99%.

Base: Opposite of ceiling, sets lower limit as a % of the full MFC scale. A non-zero value for Base will over-ride the Softstart process, whereby the flow rate is gradually ramped up upon startup to avoid turbulence before PID control begins. The softstart process is controlled by the **Start**, **End**, and **CtrlStart** parameters. More details about the softstart process can

be found in the vacuum controller manual.

Preset: Flow rate for MFC to return to when PID control is terminated. Default value is CLOSE.

Direction: sets valve control either "Upstream" or "Downstream" (relative to the pressure gauge). For our setup we use "Upstream."

Appendix D

Synthesis and degradation analysis of the peroxy radical precursor target

The following procedure was written by Adrian Amador (Yoon Group), who performed the synthesis, purification, and degradation analysis for the precursor target described in Chapter 5.

A 25-mL vial was charged with 2-methylpropanal (1 g, 0.0139 mol) and diethyl ether (5 mL). The vial was cooled to 0 °C and bromine-1,4-dioxane adduct (3.27 g, 0.0132 mol) was added in 4 portions over the course of 10 minutes with vigorous stirring (Caution: bromine-1,4-dioxane adduct is extremely flammable and must be kept away from any ignition sources and sparks). The heterogeneous mixture was stirred until the orange coloration disappeared and then allowed to stir for an additional 10 minutes. The mixture was then extracted 3 times with icecold water. The organic layer was dried over $MgSO_4$, filtered and concentrated carefully under reduced pressure to provide the product as a colorless oil still containing dioxane impurities (1.3 g, 0.0086 mol, 65% yield). Additional extractions with water would likely get rid of these impurities. The resulting product was analyzed by ^{1}H NMR spectroscopy and then divided into three portions and stored in amber vials under inert atmosphere for ∼2 weeks in a freezer, refrigerator, or at room temperature. After this time aliquots were taken for ^{1}H NMR analysis. The vials were re-sealed under air and stored for several months. After this time additional aliquots were taken for ^{1}H NMR analysis.

Figure D.1 shows that the precursor does not degrade entirely over the course of months kept in a freezer. Three ^{1}H NMR spectra were taken at 30 minutes, two weeks, and many

months after the synthesis and purification, and the Figure shows the signal associated with the methyl hydrogens at $\sim$ 1.81 ppm (cf. Figure 5.2). Unfortunately, we cannot quantitatively compare the integration of the three signals, because the spectra after 30 minutes and two weeks were taken on a 300 MHz spectrometer and the spectrum after many months was taken on a 400 MHz spectrometer. We could compare the integration signals against impurities in the NMR spectra, but it is not clear whether those impurities are due to degradation of the precursor or decomposition of the dioxane and diethyl ether impurities. Nonetheless, the degradation analysis shows that some of the precursor sample remains after many months in the freezer.

Figure D.1: ^{1}H NMR signal for the methyl hydrogens in the peroxy radical precursor over time (30 minutes, two weeks, and many months). The samples were stored in a freezer in the dark. The spectra after 30 minutes and two weeks were taken on a 300 MHz spectrometer and the spectrum after many months was taken on a 400 MHz spectrometer, so integration cannot be quantitatively compared.

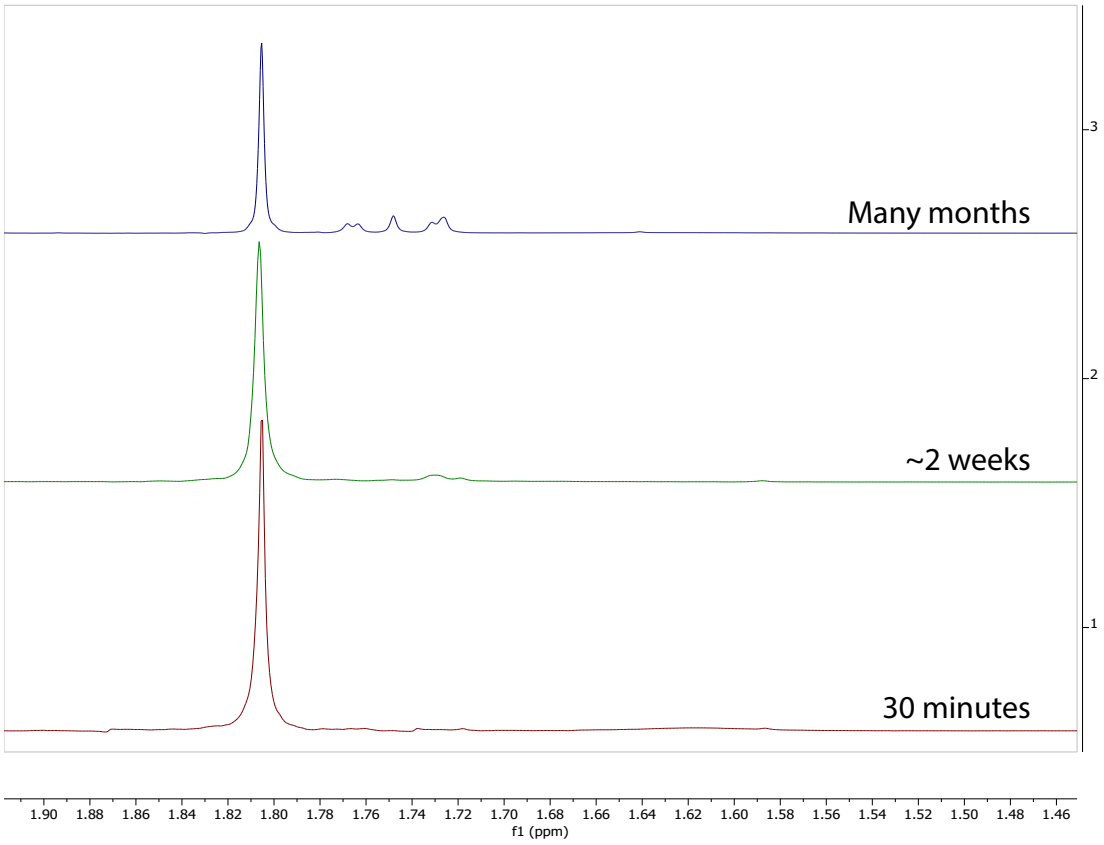
Many months
~2 weeks
30 minutes
3
2
1
1.90 1.88 1.86 1.84 1.82 1.80 1.78 1.76 1.74 1.72 1.70 1.68 1.66 1.64 1.62 1.60 1.58 1.56 1.54 1.52 1.50 1.48 1.46
f1 (ppm)